A multi-scale imaging approach to understand Osteoarthritis development

Johannes Stroebel

SIGILL · UNIVERSITAT · LUDOVIC · MAXIM ·

Munich 2020

A multi-scale imaging approach to understand Osteoarthritis development

Johannes Stroebel

Dissertation
an der Fakultät der Physik
der Ludwig-Maximilians-Universität

vorgelegt von
Johannes Stroebel
aus Stuttgart

München, den 14. Dezember 2020

Erstgutachtein: Prof. Dr. Paola Coan
Zweitgutachter: PD Dr. Guido Bönning
Tag der mündlichen Prüfung: 26.02.2021

Es ist Gottes Ehre, eine Sache zu verbergen,
aber die Ehre der Könige, eine Sache zu erforschen.

Sprüche 25,2

Table of Contents

Acknowledgments

First of all, I would like to express my gratitude to Prof. Dr. Paola Coan for making this dissertation possible. I want to thank her for working with me on an exciting topic, for supervising me during the different scientific stages of this work, encouraging and empowering me to go ahead with my scientific ideas, for making it possible to stay at the ESRF in Grenoble for experiments, for opening manifold opportunities for me such as attending conferences around the world or traveling for putting through experiments. I want to thank Dr. Alberto Bravin for supporting me during my stays and Experiments at the Synchrotron at ID17 to help me with numerous formal issues at the ESRF and introduce me to the finest restaurants in Grenoble. I want to express my enormous debt of gratitude to Dr. Alberto Mittone. He helped me with computational and image processing problems and spending thrilling nights playing "kicker" with me. I have been fortunate to have a medical collaborator in Munich on my side, Dr. Annie Horng; I would like to thank her for teaching me cartilage anatomy, the pathology of osteoarthritis, providing medical images interpretation of reconstructed images. I am very grateful for the help of Prof. Dr. Milz; he offered the histology preparation and images and made the TEM imaging possible. I also like to thank him for the fruitful scientific and medical discussions.

I like to thank Marina Eckermann and Christian Fella for providing cartilage images from laboratory X-ray sources. Special thanks go to Alexandra Pacureanu, Yang Yang and Peter Cloetens for the support during the experiments at ID16A, to Goran Lovric for his support during the experiment at the SLS and to Herwig Requardt for his support during the ID17 Experiments. I like to thank also Alexander Rack, who made the Experiments at ID19 possible. My honest gratitude goes to Giacomo Barbone, my Ph.D. college, for discussing scientific problems with me, for running in the mountains around Grenoble and for Mariele Romano to let me run my calculation on her computer. I am thankful for Thomas Vannieuwenhuyse, my Master's student, who helps me in some parts of my Thesis. A special thank you to Jonathan for supporting me in the final days of Thesis. This Thesis would not have been possible without the loving support of my wife, Lara and my parents. I owe them a debt of gratitude too great to be repaid. I have always been sure of their love, support and trust in my work, and they have ever given me a welcoming, warm home and the freedom to choose the way I want to go. Thanks to my parents, I learned to think critically, do things passionately and trust in God constantly. Thank you.

Abstract

X-ray phase-contrast imaging is an innovative and advanced imaging method. Contrary to conventional radiology, where the image contrast is primarily determined by X-ray attenuation, phase-contrast images contain additional information generated by the phase shifts or refraction of the X-rays passing through matter. The refractive effect on tissue samples is orders of magnitude higher than the absorption effect in the X-ray energy range used in biomedical imaging. This technique makes it possible to produce excellent and enhanced image contrast, particularly when examining soft biological tissues or features with similar X-ray attenuation properties. In combination with high spatial resolution detector technology and computer tomography, X-ray phase-contrast imaging has been proved to be a powerful method to examine tissue morphology and the evolution of pathologies three-dimensionally, with great detail and without the need of contrast agents.

This Thesis work has focused on developing an accurate, multi-scale X-ray-based methodology for imaging and characterizing the early stages of osteoarthritis. X-ray phase-contrast images acquired at different spatial resolutions provide unprecedented insights into cartilage and the development of its degeneration, i.e., osteoarthritis. Other types of X-ray phase-contrast imaging techniques and setups using spatial resolutions ranging from micrometer down to nanometer were applied. Lower spatial resolutions allow large sample coverage and comprehensive representations, while the nanoscale analysis provides a precise depiction of anatomical details and pathological signs. X-ray phase-contrast results are correlated to data obtained, on the same specimens, by standard laboratory methods, such as histology and transmission electron microscopy. Furthermore, X-ray phase-contrast images of cartilage were acquired using different X-ray sources and results were compared in terms of image quality. It was shown that with the use of synchrotron radiation, more detailed images and much faster data acquisitions could be achieved.

A second focus in this Thesis work has been the investigation of the reaction of healthy and degenerated cartilage under different physical pressures, simulating the different levels of stress to which the tissue is subject during daily movements. A specifically designed setup was used to dynamically study cartilage response to varying pressures with X-ray phase-contrast micro-computed tomography, and a fully volumetric and quantitative methodology to accurately describe the tissue morphological variations. This study revealed changes in the behavior of the cartilage cell structure, which differ between normal and osteoarthritic cartilage tissues.

The third focus of this Thesis is the realization of an automated evaluation procedure for the discrimination of healthy and cartilage images with osteoarthritis. In recent years, developments in neural networks have shown that they are excellently suited for image classification tasks. The transfer learning method was applied, in which a pre-trained neural network with cartilage images is further trained and then used for classification. This enables a fast, robust and automated grouping of images with pathological findings. A neural network constructed in this way could be used as a supporting instrument in pathology. X-ray phase-contrast imaging computed tomography can provide a powerful tool for a fully 3D, highly accurate and quantitative depiction and characterization of healthy and early stage-osteoarthritic cartilage, supporting the understanding of the development of osteoarthritis.

Zusammenfassung

Röntgen-Phasenkontrast-Bildgebung ist eine innovative und weiterführende Bildgebungsmethode. Im Gegensatz zu herkömlichen Absorptions-Röntgenaufnahmen, wie sie in der Radiologie verwendet werden, wird der Kontrast bei dieser Methode aus dem Effekt der Phasenverschiebung oder auch Brechung der Röngtenstrahlen gebildet. Der Brechungseffekt bei Gewebeproben ist um ein Vielfaches höher als der Absorptionseffekt des elektromagnetischen Spektrums der Röntgenstrahlen. Diese Methode ermöglicht die Darstellung von großen Kontraste im Gewebe. Unter Verwendung eines hochauflösenden Detektors und in Kombination mit der Computer-Tomographie, ist Phasenkontrast-Bildgebung eine sehr gute Methode um Knorpelgewebe und Arthrose im Knorpel zu untersuchen.

Diese Arbeit beschreibt primär ein Verfahren zur Darstellung arthrotischen Knorpels im Anfangsstadium. Die mit verschiedenen Auflösungen und 3D-Phasen-Kontrast-Methoden produzierten Aufnahmen ermöglichen einen noch nie dagewesenen Einblick in den Knorpel und die Entwicklung von Arthrose im Anfangsstadium. Hierbei kam die propagationsbasierte Phasenkontrastmethode mit einer Auflösung im mikrometer Bereich und die (Nano)-Holotomographie-Methode mit einer Auflösung im Submicrometer Bereich zum Einsatz. Durch Auflösung im mikrometer Bereich kann ein großes Volumen im Knorpel gescannt werden, während die Nano-Holotomographie Methode eine sehr große Detailauflösung aufweißt. Die Phasenkontrast-Aufnahmen werden mit zwei anderen wissenschaftlichen Methoden verglichen: mikroskopische Abbildungen histologisch aufgearbeiteter Knorpelproben und Aufnahmen eines Transmissionselektroskop zeigen sehr große Übereinstimmungen zur Röntgen-Phasenkontrast-Bildgebung. Desweiteren wurden Phasenkontrast-Aufnahmen von Knorpel aus unterschiedlichen Röntgenquellen verglichen. Hierbei zeigte sich, dass mit Hilfe des Teilchenbeschleunigers (Synchrotron) detailreichere und schnellere Aufnahmen erzielt werden können. Bilder aus Flüssig-Metall-Quellen zeigen sich durchaus von guter Qualität, erfordern jedoch sehr lange Aufnahmezeiten.

In dieser Arbeit wird zudem das Verhalten von Knorpelgewebe, welches ein Anfangsstadium von Arthrose aufweist, unter physikalischem Druck untersucht. Hierfür wurden 3D-Computertomographie-Aufnahmen von komprimiertem Knorpelgewebe angefertig und mit Aufnahmen ohne Komprimierung verglichen. Ein quantitativer Vergleich machte Veränderungen des Verhaltens der Knorpelzellstruktur (Chondronen) sichtbar. Es konnte gezeigt werden, dass Chondrone bei arthrotischem Knorpel ein verändertes Kompressionsverhalten haben.

Der dritte Fokus dieser Arbeit liegt auf der automatisierten Auswertung von Aufnahmen gesunden und arthrotischen Knorpelgewebes. Die Entwicklungen im Bereich der Neuronale Netze zeigten in den letzten Jahren, dass diese sich hervoragend für Bildklassifizierungsaufgaben eignen. Es wurde die Methode des transferierenden Lernens angewandt, bei der ein vortrainiertes Neuronales Netz mit Knorpelbildern weitertrainiert und anschließend zur Klassifizierung eingesetzt wird. Dadurch ist eine schnelle, robuste und automatisierte Gruppierung von Bildern mit pathologischen Befunden möglich. Ein derart konstruiertes Neuronales Netz könnte als unterstützendes Instrument in der Pathologie angewandt werden. Röntgen-Phasenkontrast-CT kann ein leistungsstarkes Werkzeug für eine umfassende, hochpräzise und quantitative 3D-Darstellung und Charakterisierung von gesundem Knorpel und athrotischem Knorpel im Frühstadium bieten, um das Verständnis der Entwicklung von Osteoarthritis zu erweitern.

Abbreviations

ABBREVIATIONS	**EXPLANATION**
ABI	Analyzer based imaging
BM	Bending magnet
CCD	Charged coupled device
CMOS	Metal-oxide-semiconductor
CPMU	Cryogenic permanent magnet undulator
CT	Computed tomography
DCM	Double crystal monochromator
EDTA	Ethylenediaminetetraacetic acid
EI	Edge Illumination imaging
ESRF	European Synchrotron Research Facility
FEL	Free electron laser
FRELON CAMERA	fast readout low noise camera
FWHM	Full-width half-maximum
GEV	*Giga electron volts*
GI	*Grating interferometry*
KB	Kirkpatrick-Baez
LUAG	Lutetium Aluminum Garnet
ML	Multilayer monochromator
MRI	Magnet resonant imaging
MRT	Micro Radiation Therapy
MSDDS	Mean standard deviation distance to the surface
OA	Osteoarthrosis
OARSI	Osteoarthritis Cartilage Histopathology Assessment System
OASYS	*OrAnge SYnchrotron Suite*
PBI	Propagation based imaging
PCI	Phase-contrast imaging
PCO	**"P**ioneer in **C**ameras and **O**ptoelectronics" (company)
PSI	Paul Scherrer Institute
RC	Rocking curve
SAXS	Small-angle scattering
SLS	Swiss Light Source
SR	Synchrotron Radiation
TEM	Transmission electron microscope
TOMCAT	TOmographic Microscopy Coherent rAdiology experimenTs
USAXS	Ultra-small angle scattering
U	Undulator
XOP	X-ray Oriented Program

Z	Atomic / proton number
2D	Two dimensional
3D	Three dimensional

Introduction

We live in an aging society. Germany is one of the "oldest" nations: the median age in 2020 was 47,8 years compared to the world median, which is of 31 years (Factbook 2020). With this age advancement, the prevalence of Osteoarthrosis (OA) has increased: 70% of the population over 65 suffers from this painful and debilitating disease (Zhang and Jordan 2010). This Thesis's overall target is to **visualize and analyze in 3D the changes of cartilage at the early stages of OA by using** state-of-the-art, high-sensitivity, and high-resolution X-ray imaging techniques to get a **better understanding** of the development of OA and the induced effects on the tissue.

Osteoarthritis

OA is a debilitating condition characterized by pain, joint inflammation and joint stiffness, which results in a substantial degree of physical disability. OA is a non-reversible disease (Breedveld 2004). Multiple important factors, like age or injuries, are risk factors for the development of OA. However, the development of this pathology is not well understood yet. A new image modality, which provides 3D representation combined with high spatial resolution, is highly advisable and could help elucidate the cartilage structure and its degeneration.

Imaging techniques for investigation of OA and their limitation

In clinical practice and laboratories, several techniques exist and are used to examine cartilage tissue; each of them has advantages and limitations.

Histology is the gold standard for evaluating cartilage health, OA severity and treatment efficacy (Pedersen, Goetz et al. 2013). For histological imaging, specimens are cut into thin slices, stained and analyzed with a light microscope equipped with a camera and records 2D images. Different biological parts can be differentiated and highlighted by staining, but the drawback is that the specimen must be chemically processed. This procedure and the required tissue slicing may lead to the loss of some details and/or tearing of structures. A (sub)-micrometer spatial resolution is available with histology but is destructive, and only 2D images are provided.

Magnet Resonant Imaging (MRI) is a non-invasive and no-dose imaging tool sensitive to soft tissues. It is a good method to evaluate cartilage (Rodrigues and Camanho 2010). Clinical MRI scanners for humans provide a resolution of about 300 µm (Geith, Brun et al. 2018), whereas scanners for small animals can reach resolutions down to 50 µm in-plane (Haffner-Luntzer, Müller-Graf et al. 2017).

Conventional Computed Tomography (CT), based on X-ray absorption, is particularly sensitive to materials with a high atomic number (Z). For cartilage imaging, CT is not the method of choice to detect its structural parts (Geith, Brun et al. 2018). The conventional X-ray CT has (sub)-micrometer spatial resolution but lacks soft tissue sensitivity.

Over the past fifteen years, a novel X-ray-based method, the so-called X-ray phase-contrast imaging, has been introduced in preclinical research of cartilage and musculoskeletal imaging. This technique is based on revealing and X-ray attenuation and the X-ray phase shift induced by the imaged specimen. It provides an enhanced visualization of soft tissue with respect to conventional radiographic methods without the need for contrast media or staining (Horng, Brun et al. 2014).

For PCI, there is no processing of specimens need; the samples can be imaged in the most "natural" form. A 3D representation can be obtained in a spatial resolution range ranging from tens to fractions of micrometers.

With respect to the methods mentioned above, X-ray PCI provides simultaneously high spatial resolution, high sensitivity for soft tissue, 3D visualization, tissue preservation and large sample coverage. For all these reasons, X-ray PCI can overcome many of the limitations affecting standard analysis methodologies and has grown as an established tool for cartilage and OA research.

The objectives of this Thesis

At the time when I started my Ph.D. Thesis, several works could be found in the literature demonstrating the high level of sensitivity of X-ray PCI for the depiction of both healthy and degenerated cartilage. Anatomical and pathological features within extracted human and animal tissue specimens, as well as full joints obtained by using spatial resolutions ranging from tens (46 µm) to a few micrometers (3 µm), were presented (Horng, Brun et al. 2014, Cao, Zhang et al. 2016, Gahunia, Karhula et al. 2016)

This doctoral project's overall objective has been to advance the technique and methodology based on X-PCI computed tomography to allow unprecedented 3D high-spatial and contrast-resolution for the detection and characterization of **early-stage cartilage structural alterations induced by osteoarthrosis**. The minimal sample preparation (only formalin-fixation) required for these analyses allowed the investigation of the cartilage in its almost natural form.

The function of cartilage is to serve as a cushion in the joint areas. In the knee joint, when walking or running, cartilage is under pressure. The forces present while walking can be as high as three times the person's body weight (Glitsch, Lundershausen et al. 2009). There are multiple biomechanical studies and simulation of cartilage, based on MRI images (Mononen, Mikkola et al. 2012), absorption-based X-ray tomography images(Maki, Inou et al. 2003) or angular nuclear magnetic resonance (Gründer, Kanowski et al. 2000) where the behavior of cartilage under pressure conditions was examined. This study inspired a project within my Ph.D. Thesis to use X-ray PCI micro-computed tomography to obtain detail **3D insights into the structural changes and response of human cartilage cylinders** affected by different stages of OA and under different pressure loads. The purpose was to evaluate how the pathological conditions impact the tissue's cellular and matrix structure and thus its biomechanical properties.

As proven by works in the literature as well as by the results obtained in this Ph.D. Thesis, X-ray PCI can be efficiently used as a tool for 3D-virtual-histology of biological tissue (Xuan, Zhao et al. 2015, Brandlhuber, Armbruster et al. 2016), (Coan, Bamberg et al. 2010). The high and ultra-high spatial resolutions used in state-of-the-art synchrotron X-PCI computed tomography setups, which are also equipped with fast detection systems and acquisition procedures (5-10 min per CT scan), has increased hugely the amount of data acquire during an experimental session. It is common to acquire 1 TB of data during one 8-hour shift. Analyzing and interpreting these large data amounts is highly time-consuming. This means for hospitals or research facilities that the cost for detecting pathologies is very high. An automatic and observer-independent method has been investigated for cartilage classification to address this problem, i.e., to discriminate **automatically** between healthy and OA specimens based on X-PCI 3D images. This automated analysis was realized with **artificial neural networks**, which are advanced **machine learning methods**. This part of the Thesis was inspired by the work by Abadin et al. (Abidin, Deng et al. 2018). Different neural networks are used with transfer learning to train and classify sub-micron cartilage and liver images in an **automatic and observer-independent** way.

Structure of the Thesis

In the **first chapter**, the anatomy of articular cartilage and the risk factors for OA development are explained. A description of the present knowledge on the development of OA and a list of the standard methods used for cartilage imaging are provided. Moreover, the previous works and main results of PCI application to study cartilage and OA are presented.

The **second chapter** is dedicated to X-ray phase-contrast imaging. The different techniques developed to detect the X-ray phase and the theoretical description of the so-called propagation-based PCI imaging will be given; the method used in this Thesis will be presented. This chapter includes Computed Tomography (CT) and the reconstruction methods that are currently used.

Chapter three is about X-ray production and X-ray imaging setups. This chapter includes paragraphs on synchrotron radiation and its characteristics. The two synchrotrons (the European Synchrotron Radiation Facility – ESRF, and the Swiss Light Source – SLS) and the three imaging beamlines where the experiments of this Thesis were performed are described.

Chapter four results from the multi-scale imaging study on healthy and OA cartilage specimens are shown and discussed. The full data processing methodology, including CT reconstruction, volume rendering, and segmentation with a machine learning algorithm, is described.

Chapter five is dedicated to the study of cartilage response to an applied load by high-resolution 3D PCI tomography. The experimental setup and procedure are presented as well, and the results. For this experiment, a specific analyzing method to extract 3D information about the cell network was developed. This was then used to describe the cell network and its changes under pressure.

Chapter six is about applying a convolutional neural network (CNN) to analyze and characterize high-resolution cartilage images and liver images. This study shows that it is possible to handle and analyze a large amount of data in a time-efficient, observer-independent way.

Bibliography

Abidin, A. Z., B. Deng, D. S. AM, M. B. Nagarajan, P. Coan and A. Wismuller (2018). "Deep transfer learning for characterizing chondrocyte patterns in phase-contrast X-Ray computed tomography images of the human patellar cartilage." Comput Biol Med **95**: 24-33.

Brandlhuber, M., M. Armbruster, B. Zupanc, P. Coan, E. Brun, W. Sommer and M. Rentsch (2016). "A Novel and Sensitive Approach for the Evaluation of Liver Ischemia-Reperfusion Injury After Liver Transplantation." Investigative Radiology **51**(3): 170-176.

Breedveld, F. C. (2004). "Osteoarthritis--the impact of a serious disease." Rheumatology (Oxford) **43 Suppl 1**: i4-8.

Cao, Y., Y. Zhang, X. Yin, H. Lu, J. Hu and C. Duan (2016). "3D visualization of the lumbar facet joint after degeneration using propagation phase-contrast micro-tomography." Scientific Reports **6**: 21838.

Coan, P., F. Bamberg, P. C. Diemoz, A. Bravin, K. Timpert, E. Mützel, J. G. Raya, S. Adam-Neumair, M. F. Reiser and C. Glaser (2010). "Characterization of Osteoarthritic and Normal Human Patella Cartilage by Computed Tomography X-ray Phase-Contrast Imaging: A Feasibility Study." Investigative Radiology **45**(7): 437-444.

Factbook, C. (2020, 19.11.2020). "The World Factbook." Retrieved 23.11.2020, 2020, from https://www.cia.gov/library/publications/the-world-factbook/geos/gm.html.

Gahunia, H., S. Karhula, T. Ylitalo, E. Hæggström, K. P. Pritzker, S. Saarakkala and H. J. Nieminen (2016). "3D-histopathological grading of articular cartilage using contrast-enhanced high-resolution micro-CT." Osteoarthritis and Cartilage **24**: S277-S278.

Geith, T., E. Brun, A. Mittone, S. Gasilov, L. Weber, S. Adam-Neumair, A. Bravin, M. Reiser, P. Coan and A. Horng (2018). "Quantitative Assessment of Degenerative Cartilage and Subchondral Bony Lesions in a Preserved Cadaveric Knee: Propagation-Based Phase-Contrast CT Versus Conventional MRI and CT." American Journal of Roentgenology **210**(6): 1317-1322.

Glitsch, U., N. Lundershausen, D. Knieps, A. Johannknecht and R. Ellegast (2009). Biomechanische Analyse der Kniegelenkbelastung bei Tätigkeiten im Hocken und Knien 49. Jahrestagung der Deutsche Gesellschaft für Arbeitsmedizin und Umweltmedizin. Aachen. **49**.

Gründer, W., M. Kanowski, M. Wagner and A. Werner (2000). "Visualization of pressure distribution within loaded joint cartilage by application of angle-sensitive NMR microscopy." Magnetic Resonance in Medicine **43**(6): 884-891.

Haffner-Luntzer, M., F. Müller-Graf, R. Matthys, Y. Hägele, V. Fischer, R. Jonas, A. Abaei, F. Gebhard, V. Rasche and A. Ignatius (2017). "Evaluation of high-resolution In Vivo MRI for longitudinal analysis of endochondral fracture healing in mice." PLOS ONE **12**(3): e0174283.

Horng, A., E. Brun, A. Mittone, S. Gasilov, L. Weber, T. Geith, S. Adam-Neumair, S. D. Auweter, A. Bravin, M. F. Reiser and P. Coan (2014). "Cartilage and soft tissue imaging using X-rays: propagation-based phase-contrast computed tomography of the human knee in comparison with clinical imaging techniques and histology." Invest Radiol **49**(9): 627-634.

Maki, K., N. Inou, A. Takanishi and A. Miller (2003). "Computer-assisted simulations in orthodontic diagnosis and the application of a new cone beam X-ray computed tomography." Orthodontics & craniofacial research **6**: 95-101.

Mononen, M., M. Mikkola, P. Julkunen, R. Ojala, M. Nieminen, J. Jurvelin and R. Korhonen (2012). "Effect of superficial collagen patterns and fibrillation of femoral articular cartilage on knee joint mechanics—a 3D finite element analysis." Journal of biomechanics **45**(3): 579-587.

Pedersen, D. R., J. E. Goetz, G. L. Kurriger and J. A. Martin (2013). "Comparative digital cartilage histology for human and common osteoarthritis models." Orthopedic research and reviews **2013**(5): 13-20.

Rodrigues, M. B. and G. L. Camanho (2010). "MRI EVALUATION OF KNEE CARTILAGE." Revista Brasileira de Ortopedia **45**(4): 340-346.

Xuan, R., X. Zhao, D. Hu, J. Jian, T. Wang and C. Hu (2015). "Three-dimensional visualization of the microvasculature of bile duct ligation-induced liver fibrosis in rats by x-ray phase-contrast imaging computed tomography." Scientific Reports **5**: 11500.

Zhang, Y. and J. M. Jordan (2010). "Epidemiology of osteoarthritis." Clinics in geriatric medicine **26**(3): 355-369.

1. Cartilage and Osteoarthrosis

In this chapter, the structure and anatomical features of the articular cartilage tissue and its degeneration due to osteoarthritis (OA) are presented. The main imaging and analysis modalities used for OA detection in clinical and preclinical practice are presented and discussed.

1.1. Cartilage structure

Articular cartilage is a soft tissue coated on the bone surface in a joint space. It is mellow and flexible due to its unique structure. The primary purpose of this structure is to absorb the physical energy of movements and to provide a smooth sliding of bone in the joints.

A joint is a connection between two or more bones, which gives the bones the flexibility to move. The structure and elements of a knee joint are shown in Figure 1.1.

- **Bones** (two or more): strong, stiff, weight-bearing structural element in the human body.
- **Cartilage**: tissue covering the extremities of the bones, dampening impact and allowing for smooth movement
- **Joint capsule**: a strong tissue connection to connect the bones.
- **Synovial membrane:** thin membrane, which holds the synovial fluid inside the capsule.
- **Synovial fluid**: a fluid that provides a healthy environment for the cartilage tissue and reduces friction between cartilages.
- **Ligaments:** cord-like structure of fibrous tissue connecting the bones.
- **Tendons**: strong fibrous tissue connecting the muscle and the bones, an important factor in joint stability.
- **Muscle:** bundles of fibers, which can be contracted by nerve stimulation to produce a movement.

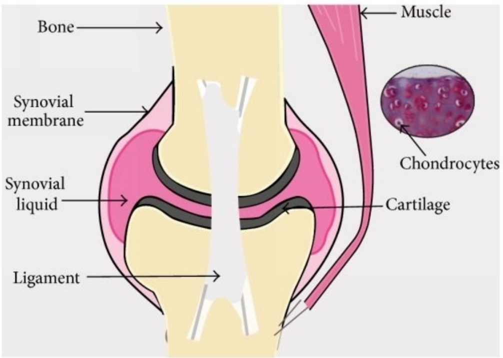

Figure 1.1 Schematic drawing of a knee joint showing the different components that joints are built of. (Catherine Baugé 2015)

Ligaments, tendons, and muscles are needed to keep the joint stable and allow moving or bending. Articular cartilage consists of chondrocytes, also called cartilage cells, within a cartilage matrix. The cartilage matrix is composed of collagen fibers, proteoglycans, and glycoproteins, which are essential features for the elasticity of cartilage that also depends on the water level in it. In the cartilage tissue, no blood vessels or nerves are present.

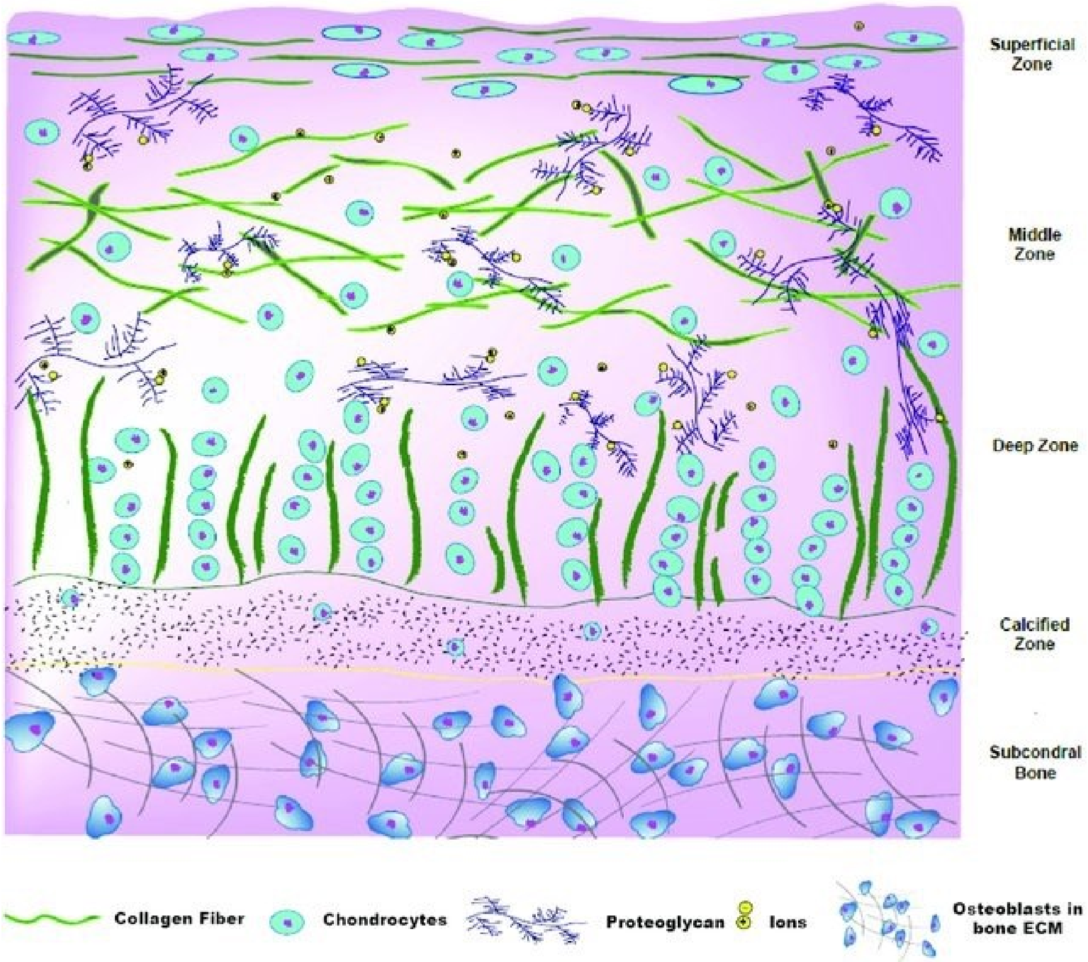

Figure 1.2 Schematic structure of articular cartilage with different layers: superficial zone, middle zone, deep zone, calcified zone and subchondral bone (Zhang, Hu et al. 2009).

Within the articular cartilage tissue, several layers can be distinguished. The density and orientation of chondrocytes, as well as the orientation of the collagen fibers, vary between the different layers, as shown in Figure 1.2 (Sophia Fox, Bedi et al. 2009). The different layers are:

- **Superficial, tangential or sliding layer**: ellipsoid chondrocytes and thin collagen fibers are oriented parallel to the surface and separate the cartilage from synovial fluid.
- **Intermediate /transitional or middle layer:** chondrocytes are irregularly distributed, collagen fibers are thicker than in the previous layer and randomly distributed.
- **Deep layer:** chondrocytes possess a spherical shape and may appear as single chondrocyte or in a group. The matrix is oriented perpendicular to the surface. This layer covers 80% of cartilage.
- **Tidemark:** a ~10 µm thick layer is separating the calcified cartilage layer from the non-calcified layer.
- **Calcified layer**: chondrocytes are embedded in a calcified matrix. The purpose of this calcified matrix is to prevent the diffusion of nutrients from the bone to the cartilage.
- **Subchondral bone:** the layer of the bone structure below cartilage in a joint

Chondrocytes are active in a metabolic sense: their function is to produce and repair the elements of the cartilage matrix (collagen fibers, proteoglycans, and glycoproteins). There is a high matrix to cell ratio in the tissue: only 1% - 5 % of the cartilage tissue are chondrocytes (Bhosale and Richardson 2008). The chondrocytes are surrounded by the pericellular matrix, which acts as a "filter" for biochemical and biomechanical signals to balance the chondrocyte production (Guilak, Nims et al. 2018). The pericellular matrix and the cell (chondrocyte) is called chondron (Poole, Flint et al. 1987). The chondrons are then surrounded by the territorial matrix, which consists mostly out of collagen fibrils forming a basket around the chondrons (Guilak and Mow 2000, Kim, Guilak et al. 2008). Multiple chondrons can be located close to each other in a lacuna. This structure is called a chondron cluster (Lotz, Otsuki et al. 2010).

The chondrocyte is in a low oxygen environment, with low metabolic turnover and contains a low number of mitochondrions (Archer and Francis-West 2003). The turnover for the proteoglycan is estimated to take up to 25 years, and the turnover for collagen between several decades up to a lifetime. (Eyre, Weis et al. 2006).

The inter-territorial region is the space around the territorial matrix; it is the largest area of the cartilage. The region has oriented bundles of collagen fibrils in it, which are arranged parallel to the cartilage surface in the superficial zone and perpendicular in the deep zone. Proteoglycans are abundant in the inter-territorial zone and contribute the most to the biomechanical properties (Sophia Fox, Bedi et al. 2009) of the tissue. Therefore, it can withstand shear as well as ductile and compressional forces, which occur in the joint capsule.

1.2. Causes and development of osteoarthritis

The reasons for the onset of OA diseases vary among different people. There are several known risk factors, primary and secondary causes, which can be identified for this pathology. Risk factors are aging, overweight, joint injury, heavy jobs that stress the joints, or specific sports activities and sports injuries.

The primary cause of OA is related to aging. With age, the water level in the cartilage increases, and the composite of protein degenerates. Also, the use and overuse of the joints inflame and irritate the cartilage over the years. In technical terms, the cartilage gets worn out over time. Genetic factors strongly determine the development of the disease. The evidence of genetic influences is derived from epidemiological studies of family history, family clustering and twin studies (Spector and MacGregor 2004).

Secondary causes of OA are related to other diseases or to an abnormal condition of the cartilage. Common causes are repeated trauma or surgery of joints, obesity, gout, diabetes or other hormone disorders.

The origin of the disease can be a convergence of primary and secondary factors. Which factors cause the disease and which sustain it is still a point of debate (Felson 1988). The structural changes of the cartilage tissue due to OA first occur on the surface, which gets soft, fibrillated and then erodes (Sandell and Aigner 2001). When the loss of extracellular matrix is recognized by the chondrocyte, a production of proteoglycans and collagen type II is activated. This phenomenon causes an imbalance in the ratio of enzyme and protein production, which results in a complete loss of cartilaginous tissue over time. The cause of this signaling is not entirely understood yet (Zhang 2015).

In order to histopathologically characterize the development of OA in the cartilage, the OARSI (Osteoarthritis Cartilage Histopathology Assessment System) was established in 2000 (Pritzker, Ostergaard et al. 2000). This grading system is based on microscopic findings on histology images.

- Grade 0: surface intact, cartilage morphology intact, standard matrix architecture, cells intact, appropriate orientation
- Grade 1: surface intact; superficial zone intact, edema and/or superficial fibrillation (abrasion), focal superficial matrix condensation, cells death, clustering, and hypertrophy
- Grade 2: surface discontinuity; matrix discontinuity at superficial zone (deep fibrillation), Cationic stain matrix depletion (Safranin O or Toluidine Blue) in the upper 1/3 of cartilage, focal perichondral increased staining (mid zone), the disorientation of chondron columns
- Grade 3: vertical fissures; Matrix vertical fissures into the mid zone, branched fissures, Cationic stain depletion (Safranin O or Toluidine Blue) into lower 2/3 of cartilage (deep zone), New collagen formation (polarized light microscopy, Picro Sirius Red stain)
- Grade 4: erosion; Cartilage matrix loss: delamination of superficial layer, mid-layer cyst formation, matrix loss superficial layer, and mid zone
- Grade 5: denudation; on the surface: sclerotic bone or reparative tissue including fibrocartilage within the denuded surface, microfractures with repair limited to the bone surface
- Grade 6: deformation, bone remodeling (more than osteophyte formation only). Includes: microfracture with fibrocartilaginous and osseous repair extending above the previous surface

For a better understanding, in Figure 1.3 - Figure 1.5, there are graphical representations of this grading system and correlations with safranin O staining histological images (Pritzker, Gay et al. 2006).

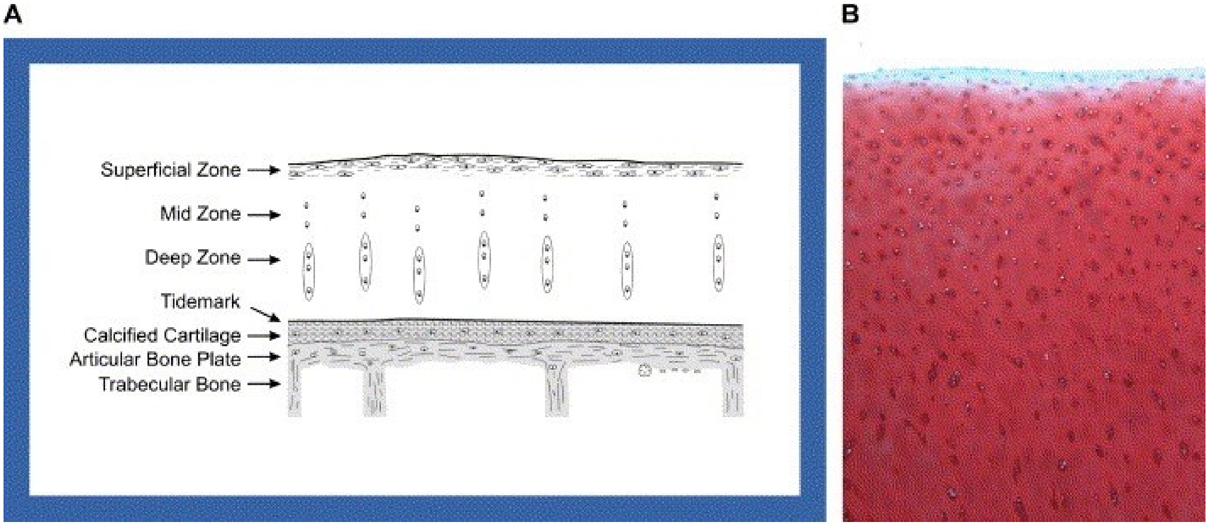

Figure 1.3 Grade 0, normal cartilage with histological features, smooth surface and organized chondrocytes, A) graphical visualization, B) histological image safranin O staining and 5x magnification (Pritzker, Gay et al. 2006)

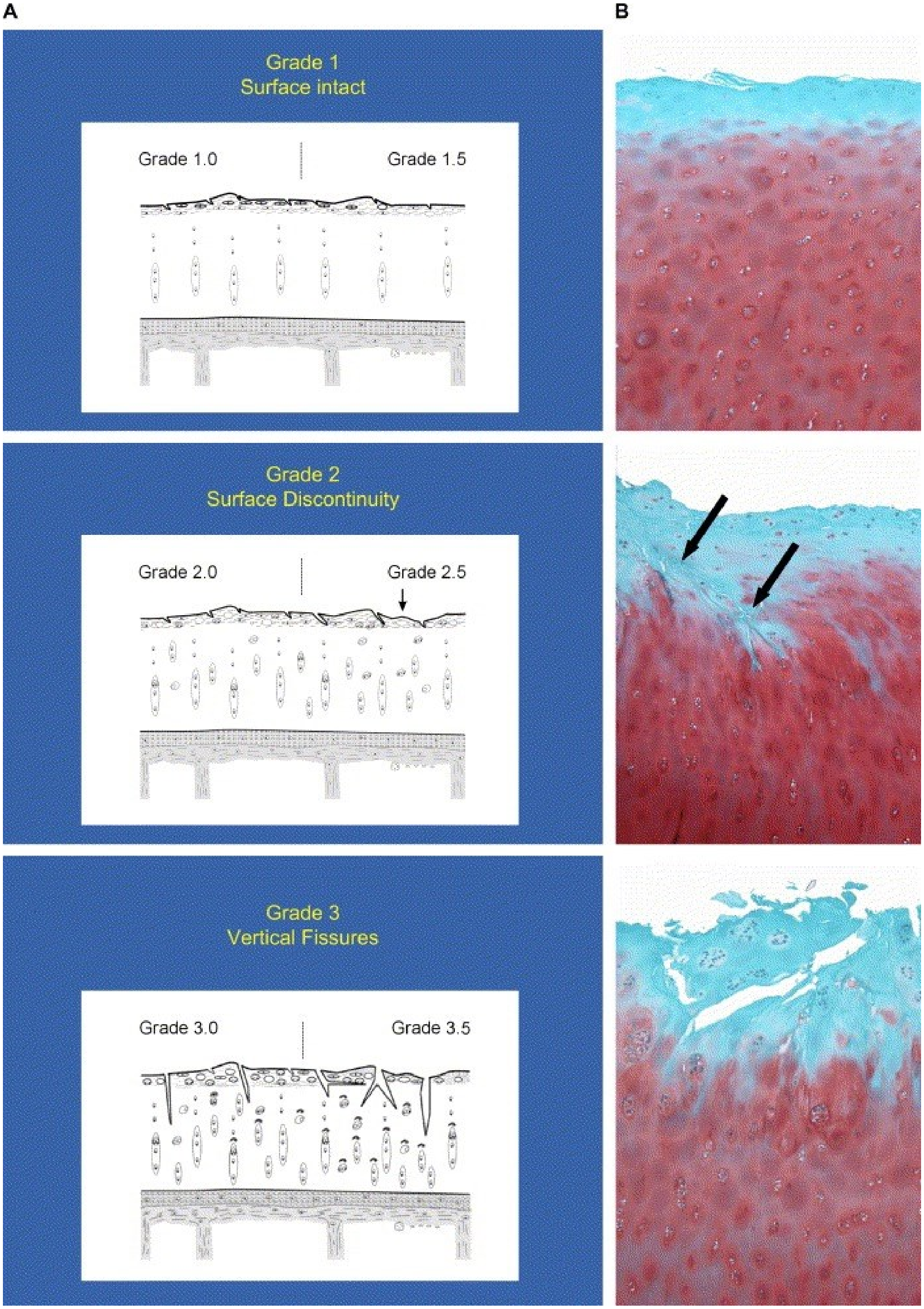

Figure 1.4 Grade 1-3; A) Visualization of cartilage B) histological image safranin O staining; Grade 1: surface intact uneven with superficial fibrillation, this can come from cell death or proliferation, mid and deep zone are unaffected. Grade 2 surface discontinuity, fibrillation extends to through the superficial zone into the midzone. Grade 3: vertical fissures are extending into the midzone. (Pritzker, Gay et al. 2006)

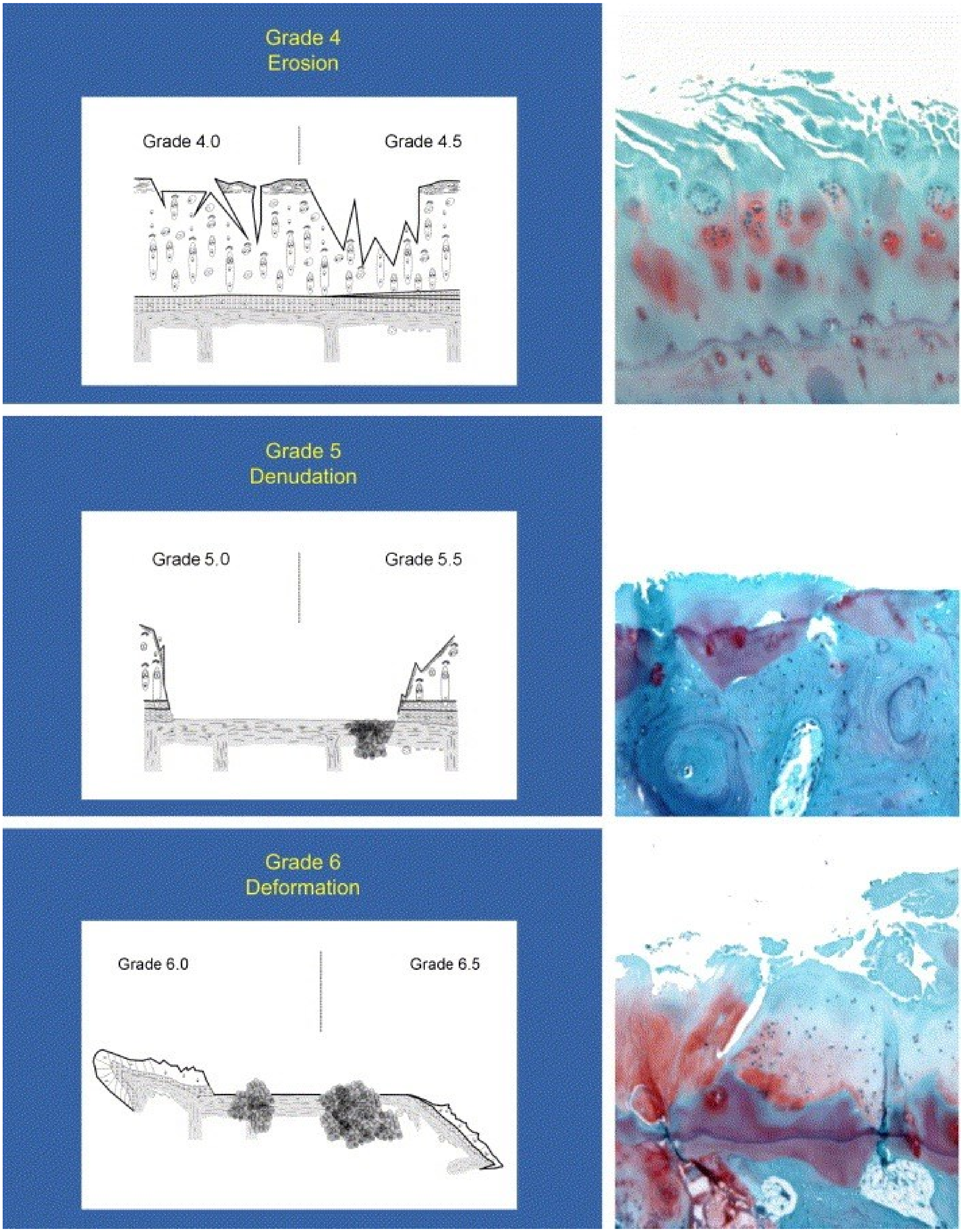

Figure 1.5 Grade 4-6: same left and right side as ***Error! Reference source not found.****. Grade 4 erosion: matrix loss is seen in superficial zone Grade 5: denudation, complete erosion of unmineralized cartilage, the surface is mineralized cartilage, micro fracture in bone plate Grade 6 deformation: micro fractures and bone remodeling changing the contour of cartilage surface (Pritzker, Gay et al. 2006)*

To get a better understanding of the early structural changes within the cartilage tissue, a 3D, high-resolution imaging method capable of visualizing in detail the components of the cartilage matrix and its alterations under pathological conditions is of paramount importance. We need to reveal the tissue modifications at the earliest stages (Grade 1-3) of OA in order to be able to intervene efficiently before reaching the irreversible point of the pathology. The work of this Ph.D. thesis aims at attaining this goal by applying state-of-the-art 3D X-ray imaging techniques and image processing tools to study the articular cartilage tissue.

1.3. Main imaging techniques for cartilage and OA studies

Both in clinical and preclinical settings, there are several tools available to study cartilage and OA. Each method has advantages and drawbacks.

Histology

It is a method that consists of fixating the tissues, cutting them into small slices and staining for highlighting tissue components. These slices are then observed under the microscope. Cartilage is fixated with neutral buffered 4 % formaldehyde to preserve the proteoglycan and glycoproteins. The bone and cartilage are decalcified with acids like Ethylenediaminetetraacetic acid (EDTA) or formal nitric acid (Kiviranta, Tammi et al. 1984). The cartilage is usually embedded in paraffin blocks on a tray to process this block with a microtome. The microtome is used to cut this block into 2-5 µm slices onto a microscope carrier (Lang 2012). The staining of the cartilage specimen is done mostly with safranin O or hematoxylin and eosin (H&E). The safranin O staining colors the cell nuclei red, the H&E colors the collagen fibers blue (Rosenberg 1971).

Transmission electron microscopy

In a Transmission Electron Microscopy (TEM) examination, an electron beam is used to investigate the specimen. The interaction of the electrons with the sample (via absorption processes) gives rise to the contrast of the microscope image. The transmitted electrons are recorded on a charged coupled device for readout. This transmitted beam can either be focused or magnified (Reimer 2013). The resolution achieved is dependent on the wavelength of the electrons (λ) and the numerical aperture (NA) of the system with n is the index of refraction and α the angular aperture:

$$d \approx \frac{\lambda}{2n\,sin\,\alpha} = \frac{\lambda}{2NA} \tag{1.1}$$

The resolution of a TEM is from 1 nm down to sub 50 pm (Erni, Rossell et al. 2009). The sample preparation is complex: biological tissues have to be embedded in a resin and then cut into less than 100 nm slices by a so-called ultramicrotome. This cutting is done with a diamond knife attached to the microtome (Porter and Blum 1953).

X-ray Computed Tomography

X-ray Computed Tomography (CT) is mostly used in the clinical workup. The contrast of the images is based on the absorption properties of the sample/body. The X-ray source and the detector system are mounted on a ring on opposing sides; this allows the system to rotate 360°. The X-ray beam has a cone beam shape, which allows fast scanning times. Each angular projection is then computed based on the Radon Transformation (Radon 1917) to get 3D images of the body/specimen. The spatial resolution of the clinically used system is between 100 µm and 200 µm (Kalender 2006). X-ray microtomography, mostly used in preclinical studies, can have a spatial resolution in the micrometer range (Elliott and Dover 1982). X-ray attenuation/absorption is the main contrast mechanism. Thus only materials with a high atomic number are well depicted on conventional CT images. Contrast agents with a high atomic number can be injected, for example, in the blood to visualize vessels. Since cartilage does not have any vessel network, the contrast agent can be used to improve the visibility of the cartilage surface (Silvast, Jurvelin et al. 2009).

Magnetic Resonance Imaging

Magnetic Resonance Imaging (MRI) is based on nuclear magnetic resonance. A strong homogenous magnetic field (B_0) is applied to create a net magnetization of hydrogen atoms. Hydrogen atoms are mainly present in the form of water in biological materials (the human body, for example, is composed of 70 % water) (Watson, Watson et al. 1980). By applying a radio frequency pulse, the net magnetization changes to 90° or 180°, which is called spin-flip. After the spin-flip, the hydrogen atoms slowly go back to the 0° net magnetization. The measure of this relaxation time is the T_1 time. Dephasing of the spin-flip in the traverse plane of the magnetic field vector can be measured; the time this loss accurse is the T_2 time. The magnetization can be measured by receiver coils. The different materials in the body have different T_1 and T_2; this is how the contrast is formed. The MRI provides, after image reconstruction, a 3D representation of the proton distribution in the specimen with a spatial resolution is about 1 mm, for clinical MRI machines (Dössel 2000, Reiser and Semmler 2013). Clinical MRI has a magnetic field strength between 1,5 T and 3 T. For research and experimental purposes, and there are full-body machines with a magnetic field strength of 7 T (Wuerfel, Sinnecker et al. 2012); for head imaging, the field strength can reach 9.4 T (Shajan, Hoffmann et al. 2011) or there is a system for small animal which reach a field strength of 16.4 T (Shajan, Hoffmann et al. 2012).

Soft tissues are visible on MRI images due to their high water content. The MRI shows a clear depiction of cartilage, but the resolution is not sufficient for any tissue details (i.e. cells). (Horng, Brun et al. 2014)

CT and MRI, as described, are mostly used in clinical practice for the patients' examination and for in vivo studies. TEM and histology are destructive, and therefore they are used for ex vivo and fundamental research of cartilage. Histology is the "gold standard" method in pathology. Histology and TEM only provide 2D information about the specimen. CT and the MRI, in contrast, offer a 3D visualization, but they are not as sensitive to cartilage tissue or do not provide enough resolution for the depiction of details, respectively. X-ray phase-contrast imaging is sensitive to cartilage tissue and can provide a 3D analysis of specimens with high spatial resolution. This is why it is used to investigate the possibilities for cartilage and OA imaging in this Thesis.

1.4. X-ray Phase-contrast Imaging for cartilage research

X-ray phase-contrast imaging (PCI) is an imaging technique for X-ray which makes use of the phase shift induced by a specimen. The images show great enhancement towards soft tissue. The next chapter is dedicated to explaining this method in more detail. X-ray PCI was first done on planar 2D images and later on combined with 3D tomography. The high-resolution (sub-micron) microtomography is often referred to as 3D virtual histology (Albers, Pacilé et al. 2018). It provides an insight of a specimen with the resolution compared to histology, but it is non-destructive to the specimen.

X-ray PCI overcomes the limitations of the standard methods, like histology, CT or MRI imaging: it is sensitive to soft tissue, with tomography it gives a 3D dataset of the specimen, and it is able to provide a high spatial resolution down to sub-micron resolution. In 2D X-ray, PCI provides a high temporal resolution (Escauriza, Olbinado et al. 2018). For all these reasons and given the particular characteristics of the tissue, X-ray phase-contrast radiography and CT have been used soon for cartilage studies

One of the first results of articular cartilage with PCI was produced in planar mode with the analyzer-based PCI imaging (ABI) method, which will be described in chapter two, paragraph Analyzer-based imaging, (Mollenhauer, Aurich et al. 2002, Muehleman, Chapman et al. 2003). In the following year, ABI measurements could demonstrate that it is powerful for orthopedics diagnosis (Muehleman, Majumdar et al. 2004, Wagner, Aurich et al. 2005). Studies for understanding healing processes with implants are done to demonstrate the sensitivity of the ABI method compared to conventional radiography (Wagner, Sachse et al. 2006). A step forward was obtaining 3D information of a sample with PCI. This was first done again with the ABI technique using a voxel size of 56.2 μm^3 (Li, Zhong et al. 2009). In a further experiment, a voxel size of 8 μm^3 was used to characterize osteoarthritic and normal human patella cartilage (Coan, Bamberg et al. 2010). The potential of in vivo ABI was firstly demonstrated on Guinea pig knees with 2D planar images (Coan, Wagner et al. 2010).

The next step forward in 2014 was the examination of a full human knee with PCI in comparison with other clinical imaging techniques and histology (Horng, Brun et al. 2014). The PCI method used in this study was propagation-based imaging (PBI), which is explained in more detail in chapter two, paragraph Propagation based imaging (PBI). It showed that PCI could detect early changes in OA conditions on a full joint. The voxel size used in this experiment was 46 x 46 x 46 μm^3.

More recent works concerned the translation of the X-ray PCI method with laboratory X-ray sources and the development of animal models for OA and PCI. In the paper of Massimo Marenzana (Marenzana, Hagen et al. 2014), a laboratory setup for PCI, based on the so-called edge-illumination contrast mechanism (Diemoz, Hagen et al. 2013), which is explained in chapter two, paragraph Edge Illumination imaging is used to detect cartilage lesion in a mice knee without contrast agent, and results are compared with synchrotron-based images. Some studies showed as well the potential of X-ray PCI for detecting lesions on small animal models by using PBI on rabbit femoral heads (Sun, Zhang et al. 2015) and guinea pigs of different ages (Horng, Geith et al. 2017).

All published works, at the time of the beginning of this Thesis, presented PCI results obtained by using pixel sizes of 3 µm or bigger. Therefore, in this Thesis, we wanted to push further the limits of spatial resolution in order to study the development and effects of OA on the cartilage tissue at the micro- and nano-scale in 3D and in a non-destructive way. We have applied what is nowadays called 'virtual histology by X-rays' and implemented novel analysis procedures to extract quantitative information from acquired and reconstructed high contrasted and detailed 3D datasets.

Bibliography

Albers, J., S. Pacilé, M. A. Markus, M. Wiart, G. V. Velde, G. Tromba and C. Dullin (2018). "X-ray-Based 3D Virtual Histology—Adding the Next Dimension to Histological Analysis." Molecular Imaging and Biology: 1-10.

Archer, C. W. and P. Francis-West (2003). "The chondrocyte." The International Journal of Biochemistry & Cell Biology **35**(4): 401-404.

Bhosale, A. M. and J. B. Richardson (2008). "Articular cartilage: structure, injuries and review of management." British Medical Bulletin **87**(1): 77-95.

Catherine Baugé , K. B. (2015). "Use of Adult Stem Cells for Cartilage Tissue Engineering: Current Status and Future Developments." Stem Cells International **2015**: 14.

Coan, P., F. Bamberg, P. C. Diemoz, A. Bravin, K. Timpert, E. Mützel, J. G. Raya, S. Adam-Neumair, M. F. Reiser and C. Glaser (2010). "Characterization of Osteoarthritic and Normal Human Patella Cartilage by Computed Tomography X-ray Phase-Contrast Imaging: A Feasibility Study." Investigative Radiology **45**(7): 437-444.

Coan, P., A. Wagner, A. Bravin, P. C. Diemoz, J. Keyrilainen and J. Mollenhauer (2010). "In vivo x-ray phase-contrast analyzer-based imaging for longitudinal osteoarthritis studies in guinea pigs." Phys Med Biol **55**(24): 7649-7662.

Diemoz, P. C., C. K. Hagen, M. Endrizzi and A. Olivo (2013). "Sensitivity of laboratory based implementations of edge illumination X-ray phase-contrast imaging." Applied Physics Letters **103**(24).

Dössel, O. (2000). "Bildgebende Verfahren in der Medizin." Von der Technik zur medizinischen Anwendung **1**.

Elliott, J. and S. Dover (1982). "X-ray microtomography." Journal of microscopy **126**(2): 211-213.

Erni, R., M. D. Rossell, C. Kisielowski and U. Dahmen (2009). "Atomic-resolution imaging with a sub-50-pm electron probe." Physical review letters **102**(9): 096101.

Escauriza, E. M., M. P. Olbinado, M. E. Rutherford, D. J. Chapman, J. C. Jonsson, A. Rack and D. E. Eakins (2018). "Ultra-high-speed indirect x-ray imaging system with versatile spatiotemporal sampling capabilities." Applied optics **57**(18): 5004-5010.

Eyre, D. R., M. A. Weis and J.-J. Wu (2006). "Articular cartilage collagen: an irreplaceable framework." Eur Cell Mater **12**(1): 57-63.

Felson, D. T. (1988). "Epidemiology of hip and knee osteoarthritis." Epidemiologic reviews **10**: 1-28.

Guilak, F. and V. C. Mow (2000). "The mechanical environment of the chondrocyte: a biphasic finite element model of cell–matrix interactions in articular cartilage." Journal of biomechanics **33**(12): 1663-1673.

Guilak, F., R. J. Nims, A. Dicks, C.-L. Wu and I. Meulenbelt (2018). "Osteoarthritis as a disease of the cartilage pericellular matrix." Matrix biology : journal of the International Society for Matrix Biology **71-72**: 40-50.

Horng, A., E. Brun, A. Mittone, S. Gasilov, L. Weber, T. Geith, S. Adam-Neumair, S. D. Auweter, A. Bravin, M. F. Reiser and P. Coan (2014). "Cartilage and soft tissue imaging using X-rays: propagation-based phase-contrast computed tomography of the human knee in comparison with clinical imaging techniques and histology." Invest Radiol **49**(9): 627-634.

Horng, A., T. Geith, E. Brun, A. Mittone, S. Gasilov, S. Adam-Neumair, A. Bravin, M. F. Reiser and P. Coan (2017). "Cartilage Imaging using HR Propagation-Based Phase-contrast CT in a Guinea Pig Knee Joint Model of Different Age Groups." Seminars in Musculoskeletal Radiology **21**(S01): 1-5.

Kalender, W. A. (2006). Computertomographie: Grundlagen, Gerätetechnologie, Bildqualität, Anwendungen, Publicis Corporate Publ.

Kim, E., F. Guilak and M. A. Haider (2008). "The dynamic mechanical environment of the chondrocyte: a biphasic finite element model of cell-matrix interactions under cyclic compressive loading." Journal of biomechanical engineering **130**(6): 061009.

Kiviranta, J., M. Tammi, J. Jurvelin, A.-M. Säämänen and H. Helminen (1984). "Fixation, decalcification, and tissue processing effects on articular cartilage proteoglycans." Histochemistry **80**(6): 569-573.

Lang, G. (2012). Histotechnik: Praxislehrbuch für die biomedizinische Analytik, Springer-Verlag.

Li, J., Z. Zhong, D. Connor, J. Mollenhauer and C. Muehleman (2009). "Phase-sensitive X-ray imaging of synovial joints." Osteoarthritis and cartilage **17**(9): 1193-1196.

Lotz, M. K., S. Otsuki, S. P. Grogan, R. Sah, R. Terkeltaub and D. D'Lima (2010). "Cartilage cell clusters." Arthritis and rheumatism **62**(8): 2206-2218.

Marenzana, M., C. K. Hagen, P. D. N. Borges, M. Endrizzi, M. B. Szafraniec, T. L. Vincent, L. Rigon, F. Arfelli, R.-H. Menk and A. Olivo (2014). "Synchrotron- and laboratory-based X-ray phase-contrast imaging for imaging mouse articular cartilage in the absence of radiopaque contrast agents." Philosophical transactions. Series A, Mathematical, physical, and engineering sciences **372**(2010): 20130127.

Mollenhauer, J., M. Aurich, Z. Zhong, C. Muehleman, A. Cole, M. Hasnah, O. Oltulu, K. Kuettner, A. Margulis and L. Chapman (2002). "Diffraction-enhanced X-ray imaging of articular cartilage." Osteoarthritis and cartilage **10**(3): 163-171.

Muehleman, C., L. D. Chapman, K. E. Kuettner, J. Rieff, J. A. Mollenhauer, K. Massuda and Z. Zhong (2003). "Radiography of rabbit articular cartilage with diffraction-enhanced imaging." The Anatomical Record Part A: Discoveries in Molecular, Cellular, and Evolutionary Biology: An Official Publication of the American Association of Anatomists **272**(1): 392-397.

Muehleman, C., S. Majumdar, A. S. Issever, F. Arfelli, R.-H. Menk, L. Rigon, G. Heitner, B. Reime, J. Metge and A. Wagner (2004). "X-ray detection of structural orientation in human articular cartilage." Osteoarthritis and cartilage **12**(2): 97-105.

Poole, C. A., M. H. Flint and B. W. Beaumont (1987). "Chondrons in cartilage: ultrastructural analysis of the pericellular microenvironment in adult human articular cartilages." Journal of orthopaedic research **5**(4): 509-522.

Porter, K. R. and J. Blum (1953). "A study in microtomy for electron microscopy." The anatomical record **117**(4): 685-709.

Pritzker, K., K. Ostergaard and D. Salter (2000). "Towards standardization of osteoarthritis histopathology: terminology, topology and technology." Osteoarthritis Cartilage **8**(Suppl B): IP010.

Pritzker, K. P. H., S. Gay, S. A. Jimenez, K. Ostergaard, J. P. Pelletier, P. A. Revell, D. Salter and W. B. van den Berg (2006). "Osteoarthritis cartilage histopathology: grading and staging." Osteoarthritis and Cartilage **14**(1): 13-29.

Radon, J. (1917). "Über die Bestimmung von Funktionen durch ihre Integralwerte längs gewisser Mannigfaltigkeiten." Berichte über die Verhandlungen der Königlich-Sächsischen Gesellschaft der Wissenschaften zu Leipzig **69**(Mathematisch-Physische Klasse): 262-277.

Reimer, L. (2013). Transmission electron microscopy: physics of image formation and microanalysis, Springer.

Reiser, M. and W. Semmler (2013). Magnetresonanztomographie, Springer-Verlag.

Rosenberg, L. (1971). "Chemical basis for the histological use of safranin O in the study of articular cartilage." JBJS **53**(1): 69-82.

Sandell, L. J. and T. Aigner (2001). "Articular cartilage and changes in Arthritis: Cell biology of osteoarthritis." Arthritis Research & Therapy **3**(2): 107.

Shajan, G., J. Hoffmann, D. Z. Balla, D. K. Deelchand, K. Scheffler and R. Pohmann (2012). "Rat brain MRI at 16.4 T using a capacitively tunable patch antenna in combination with a receive array." NMR in Biomedicine **25**(10): 1170-1176.

Shajan, G., J. Hoffmann, J. Budde, G. Adriany, K. Ugurbil and R. Pohmann (2011). "Design and evaluation of an RF front-end for 9.4 T human MRI." Magnetic resonance in medicine **66**(2): 594-602.

Silvast, T. S., J. S. Jurvelin, A. S. Aula, M. J. Lammi and J. Töyräs (2009). "Contrast Agent-Enhanced Computed Tomography of Articular Cartilage: Association with Tissue Composition and Properties." Acta Radiologica **50**(1): 78-85.

Sophia Fox, A. J., A. Bedi and S. A. Rodeo (2009). "The Basic Science of Articular Cartilage: Structure, Composition, and Function." Sports Health **1**(6): 461-468.

Spector, T. D. and A. J. MacGregor (2004). "Risk factors for osteoarthritis: genetics¹." Osteoarthritis and Cartilage **12**: 39-44.

Sun, W., Y. Zhang, F. Gao, Z. Li, G. Li and L. Pan (2015). "Phase-contrast imaging with synchrotron hard X-ray of micro lesions of the cartilage of the femoral head in rabbits." International Journal of Clinical and Experimental Medicine **8**(11): 20086-20091.

Wagner, A., M. Aurich, N. Sieber, M. Stoessel, W. D. Wetzel, K. Schmuck, M. Lohmann, B. Reime, J. Metge, P. Coan, A. Bravin, F. Arfelli, L. Rigon, R. H. Menk, G. Heitner, T. Irving, Z. Zhong, C. Muehleman and J. A. Mollenhauer (2005). "Options and limitations of joint cartilage imaging: DEI in comparison to MRI and sonography." Nuclear Instruments and Methods in Physics Research Section A: Accelerators, Spectrometers, Detectors and Associated Equipment **548**(1-2): 47-53.

Wagner, A., A. Sachse, M. Keller, M. Aurich, W. Wetzel, P. Hortschansky, K. Schmuck, M. Lohmann, B. Reime and J. Metge (2006). "Qualitative evaluation of titanium implant integration into bone by diffraction enhanced imaging." Physics in Medicine & Biology **51**(5): 1313.

Watson, P. E., I. D. Watson and R. D. Batt (1980). "Total body water volumes for adult males and females estimated from simple anthropometric measurements." The American journal of clinical nutrition **33**(1): 27-39.

Wuerfel, J., T. Sinnecker, E. B. Ringelstein, S. Jarius, W. Schwindt, T. Niendorf, F. Paul, I. Kleffner and J. Dörr (2012). "Lesion morphology at 7 Tesla MRI differentiates Susac syndrome from multiple sclerosis." Multiple Sclerosis Journal **18**(11): 1592-1599.

Zhang, L., J. Hu and K. A. Athanasiou (2009). "The Role of Tissue Engineering in Articular Cartilage Repair and Regeneration." Critical reviews in biomedical engineering **37**(1-2): 1-57.

Zhang, Z. (2015). "Chondrons and the pericellular matrix of chondrocytes." Tissue Engineering Part B: Reviews **21**(3): 267-277.

2. X-ray Phase-contrast Imaging

2.1. Introduction

Conrad Röntgen discovered X-ray radiation in 1895 (Röntgen 1896), which signified the start of non-invasive medical imaging. The potential of X-ray imaging was recognized immediately after this discovery. The next significant step in X-ray imaging was made when two-dimensional radiographs were followed by three-dimensional computed tomography (CT) imaging, developed by the electrician Sir G. N. Hounsfield in 1973 (Hounsfield 1973) based on the theoretical work of Johann Radon in 1917 (Radon 1917). The underlying physical principle did not change over the following years. The absorption of X-rays in different materials due to their chemical composition and thickness is used to generate contrast on the image (i.e., radiograph). This mechanism leads to the result that highly absorbing materials, e.g. bone, are better visible on radiographs than soft tissue (e.g., brain, breast, lungs, cartilage). To overcome this limitation, a new X-ray imaging method has been applied in biomedicine over the last decades, which makes use of refraction information in addition to the absorption signal. This method is called X-ray Phase-contrast Imaging (PCI) and includes various techniques to detect the refraction signal (Momose and Fukuda 1995). Such a method allows for improved image contrast and, thus sensitivity. As a result, weakly absorbing materials may be better depicted even without the use of contrast agents. X-ray PCI combined with the CT technology and methodology can provide 3D high-resolution visualization of soft and hard tissues simultaneously such as for cartilage imaging (Horng, Brun et al. 2014).

2.2. Index of refraction

The fundamental physical principle of PCI is described starting from the complex index of refraction. Let us assume a plane incident X-ray wavefront passing through an object. The incoming wave changes can be due to absorption, elastic or inelastic scattering inside the matter.

The index of refraction can be written in the following form (Jackson 1999):

$$n = 1 - \delta + i\beta \tag{2.1}$$

The phase shift of an electromagnetic wave occurring within matter is determined by the **refractive index decrement $\boldsymbol{\delta}$**. The photoelectric absorption of X-rays in the matter is linked to the **attenuation index $\boldsymbol{\beta}$**.

In the free electron model, which describes the polarization of matter by an electromagnetic field of incident radiation, the electron density ρ_e is proportional to the electric susceptibility χ_e, for hard X-rays and far from the absorption edge. The parts of the index of refraction δ and β can be written as the real and imaginary part of χ_e (Zachariasen 2004):

$$\delta = \frac{1}{2}\chi_{0_r} \text{ and } \beta = \frac{1}{2}\chi_{0_i} \tag{2.2}$$

The expressions can be written in terms of electron density ρ_e, then they look like this (Jackson 1999):

$$\delta = \frac{r_e \lambda^2}{2\pi}\rho_e \tag{2.3}$$

$$\beta = \frac{r_e \lambda^3}{4\pi^2 c}\rho_e \sum_j \frac{f_j \gamma_j}{Z} \tag{2.4}$$

Where r_e is the electron radius, λ the wavelength of X-rays, f_j gives the number of electrons per atom, γ_j is the damping constant of the atom, Z the atomic number. The electron density ρ_e is connected to the macroscopic mass density ρ:

$$\rho_e = \frac{Z}{V} = Z\,\rho\,\frac{N_a}{A} \tag{2.5}$$

Where N_a is the Avogadro constant, and A is the atomic mass number

Refraction occurs due to Thompson elastic scattering; therefore, the refractive index decrement can be written generally as:

$$\delta = \frac{r_e\lambda^2}{2\pi V}\sum_j (Z + f_{jr}) \tag{2.6}$$

Where f_{jr} is the real part of the wavelength-dependent dispersion correction of the atomic scattering factor. The absorption index β can be written as:

$$\beta = \frac{r_e\lambda^2}{4\pi^2 V}\sum_j f_{ji} \tag{2.7}$$

The absorption process is dominated by the imaginary part of the wavelength-dependent dispersion correction f_{ji}, which behaves with the energy as E^{-m}With m between three and four.

The linear absorption coefficient μ can be related to the absorption index β (Raven, Snigirev et al. 1996):

$$\mu = \frac{4\pi\beta}{\lambda} \tag{2.8}$$

Within an object, δ and β are changing; therefore they are functions of the spatial coordinates (x,y,z). The change in intensity follows the law of Lambert-Beer, where μ is the linear absorption coefficient:

$$I(z) = I_0 e^{-\mu z} \tag{2.9}$$

The intensity is proportional to the square amplitude of the electrical field, $\mathrm{I} \sim E^2$: Thus, the phase cannot directly be accessed by simply recording the intensity of X-rays.

The scattering properties of the radiation in a crystalline medium are generally defined using the structure factor. The crystalline structure does not influence the wave propagation if the Bragg reflection is not satisfied. The refractive index, in this case, can be expressed in terms of the (complex) F_0 structure factor as:

$$n = 1 - \frac{r_e\lambda^2}{2\pi}\frac{F_0}{V} \tag{2.10}$$

If the refractive index *n* is calculated numerically, the change from unity is reasonably small (Born and Wolf 1999). Therefore, δ and β are very small, as well. However, δ in soft tissue is two to three orders of magnitudes higher than β. This is demonstrated in Figure 2.1, where the δ/β ratio for bone and soft tissue is reported, as an example.

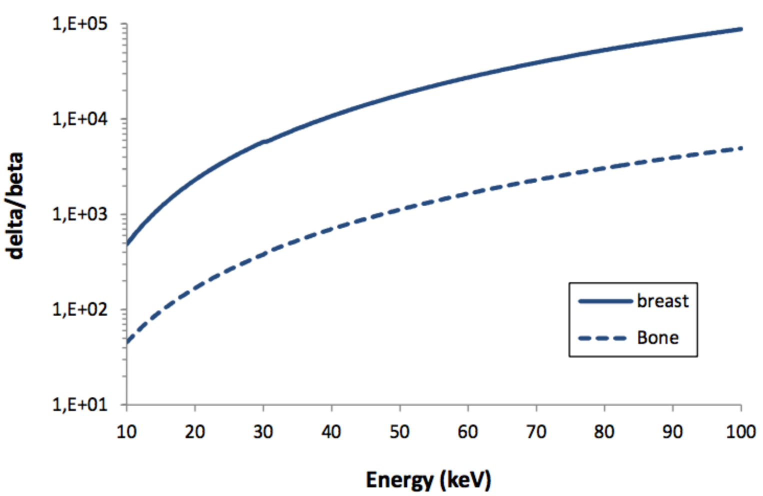

Figure 2.1 Ratio of the delta and beta indices ranges 10-100 keV for bone and soft tissue. The values have been calculated with XOP[1]

So, if one uses high X-ray energies, refraction compared to the absorption effect is up to 3-4orders of magnitude higher. The significant difference between δ and β is the responsible advantages of PCI regarding absorption-based radiology; the phase contribution is an additional and essential source of contrast when the absorption counterpart is very weak or undetectable.

2.3. Coherence

Coherence is an important physical principle for X-ray PCI. There are two different types of coherence: longitudinal and spatial coherence. The longitudinal coherence is defined by the distance of two in-phase waves traveling in order to have a phase shift of π.

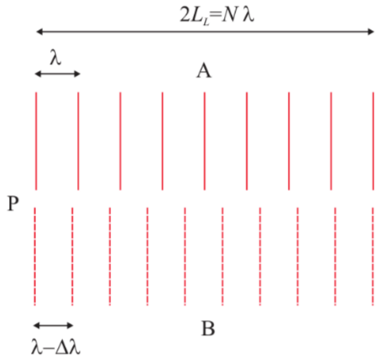

Figure 2.2 visualization of the longitudinal coherence length (Als-Nielsen and McMorrow 2011)

This distance is called longitudinal coherence length L_L.

With equation $2L_L = N\lambda$ and $N \approx \frac{\lambda}{\Delta\lambda}$ the longitudinal coherence can be expressed as:

$$\boldsymbol{L_L = \frac{1}{2}\frac{\lambda^2}{\Delta\lambda}} \qquad (2.11)$$

---

[1] http://www.esrf.fr/computing/scientific/dabax/

A small energy bandwidth Δλ (monochromatic)) leads to a high longitudinal coherence length.

The spatial coherence length, L_S, is the distance that two waves, with the same wavelengths but different directions, can travel to diphase entirely. In Figure 2.3, waves A and B, originating from two points and having the same phase propagate in space along with the respective directions and after $2L_S$, they are in phase again, which leads to equation $2L_T\Delta\theta = \lambda$, with $\Delta\theta$ is the angle between the travel directions of the wavefronts. Let us indicate with D the distance between the two-point sources. The distance from the source to point P, the point of the observer, is called R, then $\Delta\theta = \frac{D}{R}$. The relation for the transversal (spatial) coherence is:

$$\boldsymbol{L_T = \frac{\lambda}{2}\left(\frac{R}{D}\right)} \tag{2.12}$$

The spatial coherence is depending on the distance R the X-rays are traveling and the source size D.

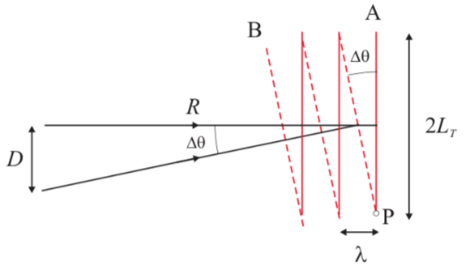

Figure 2.3 visualization of the spatial coherence length (Als-Nielsen and McMorrow 2011)

2.4. Phase-contrast imaging techniques

One of the first papers that discusses the use of coherent X-rays for imaging was published in 1995 by A. Snigirev (Snigirev, Snigireva et al. 1995). It is easy to detect X-ray absorption because the absorption is directly correlated to the intensity recorded on the detector. However, the X-ray phase cannot directly be measured and needs the use of specific setups in order to be detected. In this paragraph, four different techniques are presented; these are the most common PCI methods. Three of them use an optical device for retrieving phase information, and one uses the interferences of X-ray during their propagation.

2.4.1. Propagation based imaging (PBI)

Propagation-based imaging is the PCI technique with the most straightforward setup: an X-ray beam with a 'sufficient' spatial coherence, an object and a detector. The spatially coherent X-ray beam is propagating through the samples. This leads to a variation in both the amplitude and phase of the X-ray wavefront. In a geometrical approach, the phase shift corresponds to a change in the direction of propagation of the X-rays after the object (Peter, Raymond et al. 1996).

An interference pattern between partial X-ray wavefronts, which have been deviated by the object, is then recorded at the detector, placed at a certain distance from the object. Detection is possible because the phase shifts are transformed into intensity variations by the Fresnel diffraction (Born and Wolf 1999).

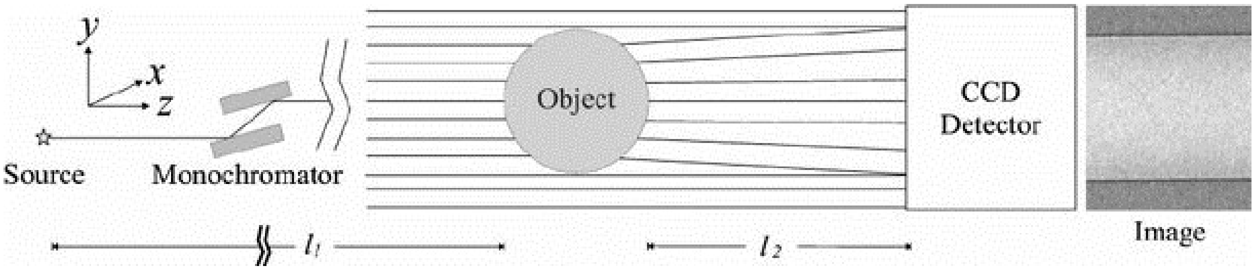

Figure 2.4 Schemata of a Propagation-based imaging setup a partially coherent monochromatic beam is passing through an object; after a distance, an interference pattern can be recorded on the detector. (Kitchen, Lewis et al. 2005)

In this setup, no additional optical elements are needed. Therefore, it is aberration-free, and the achievable spatial resolution is mostly dependent on the source size and the imaging detector characteristics (Arhatari, Mancuso et al. 2004). The angular deviation of X-rays after passing through the sample can be expressed approximately for a monochromatic wavefront traveling in the z-direction as, if $|\Delta\varphi| << 2\pi/\lambda$ is valid :

$$\Delta\alpha(x,y) \simeq -\frac{\lambda}{2\pi}\Delta_{x,y}\varphi(x,y,\lambda) \tag{2.13}$$

With $\Delta\varphi$ and λ as phase shift and wavelength of the X-ray wave. The propagation-based imaging technique is sensitive to the phase shift in x and y directions, as shown in Figure 2.4. The obtained signal strongly depends on the distance between the object and the detector (sample-to-detector distance d). If the distance in the z-direction varies and the size of the object is a, three regimes can be distinguished (Snigirev, Snigireva et al. 1995):

- d ≈ 0 **absorption regime**, no phase-contrast signal, therefore only absorption contrast is visible
- $r_f^2 = \lambda d \leq a^2$ **near field refraction regime or edge detection**; the distance d is small, r_f is the radius of the first Fresnel zone in the object plane. The contrast is formed around the phase modulation's high-frequency components, which occur on the edges of features within the object. This signal provides strong geometrical information because it rises from the interference of portions of the wavefront that experience different phase shifts at the structures' interfaces with slightly different refractive index.
- $r_f^2 = \lambda d > a^2$ **far-field diffraction or Frauenhofer regime**; the interference patterns are well detected, but the patterns cannot be easily associated with a specific boundary within the object. These images contain little direct information about the object itself, and the shape of the object is hardly recognizable. But the images contain Fourier transformed information about the object, which can be retrieved.

The recorded intensity on the detector can be described by using the transport of intensity equation. This equation is only valid under two assumptions. It can be used only in the near field regime, where the propagation distances are sufficiently small, and when the object has a slowly varying phase in the (x,y) plane (transversal to the optical z-direction). Under the mentioned approximations, the intensity modulation is proportional to the Laplacian phase (Gureyev, Raven et al. 1999).

For PBI, the X-ray beam needs to have a sufficient degree of lateral (spatial) coherence (see paragraph 2.3 Coherence). The spatial coherence is linked to source size and distance to the source. Synchrotron sources and micro-focus X-ray tubes have source sizes between 10 and 20 µm. The source size of a standard rotating anode laboratory X-ray tube is characterized by a blurring effect on the interference pattern due to the extended source size and the limited distance from the source. The degree of monochromaticity of the beam is less essential, as proven by Wilkins, who obtained PBI images even with a polychromatic spectrum generated by a conventional micro-focus X-ray tube (Wilkins, Gureyev et al. 1996, Zhou, Lundström et al. 2013, Larsson, Vågberg et al. 2016).

Specific image acquisition procedures and algorithms have been developed over the years in order to allow the quantitative exploitation of PCI. For PBI, two main phase retrieval protocols are used: one is based on a single distance image and a certain number of assumptions (this method is commonly referred to as the "Paganin algorithm" from the name of his inventor (Paganin, Mayo et al. 2002)); and the second is the so-called holographic imaging, which uses a set of images acquired with different sample-to-detector distances (Cloetens, Ludwig et al. 1999)). Both methods were used in this Thesis.

2.4.1.1. Single distance phase retrieval algorithm

The next paragraph describing the phase retrieval for a single distance comes from the paper of Paganin et al. (Paganin, Mayo et al. 2002)

Let us consider the transport-of-intensity equation, which describes the evolution of a wave propagating after interaction with matter.

$$\nabla_{\perp}(I(r_{\perp},z)\nabla_{\perp}(\varphi(r_{\perp},z)) = -\frac{2\pi}{\lambda}\frac{\partial}{\partial z}\, I(r_{\perp},z) \tag{2.14}$$

With $I(r_{\perp},z)$ the X-ray wave intensity and phase $\varphi(r_{\perp},z)$. $r_{\perp}$ is the position vector, which is perpendicular to the wave propagation direction.

We assume that the sample contains a single material and is homogeneous. Lambert-Beer's law provides the intensity of the X-ray wave exiting the sample:

$$I(r_{\perp},z=0) = I_0 e^{-\mu T(r_{\perp})} \tag{2.15}$$

With $T(r_{\perp})$ is the thickness of the sample and I_0 the intensity of the incoming wave. If we assume that the thickness of the object is sufficiently small, then the phase after the sample is proportional to the thickness:

$$\varphi(r_{\perp},z=0) = -\frac{2\pi}{\lambda}\delta\, T(r_{\perp}) \tag{2.16}$$

With δ, the refractive index decrement (2.1).

Substitute equations (2.15) and (2.16) into equation (2.14), an equation non-linear in $T(r_{\perp})$ is obtained, but it can be rewritten as an equation linear in in $e^{-\mu T(r_{\perp})}$.

$$-\frac{\delta}{\mu} I_0 \nabla_\perp^2 e^{-\mu T(r_\perp)} = \frac{\partial}{\partial z} I(r_\perp, z=0) \tag{2.17}$$

Equation (2.17) used the identity of equation (2.18)

$$\delta \nabla_\perp \left(e^{-\mu T(r_\perp)} \nabla_\perp T(r_\perp) \right) = -\frac{\delta}{\mu} \nabla_\perp^2 e^{-\mu T(r_\perp)} \tag{2.18}$$

The right side of equation (2.17) can be estimated by measuring the intensity of two sufficiently close planes with a distance of R_2:

$$\frac{\partial}{\partial z} I(r_\perp, z=0) \approx \frac{I(r_\perp, z=R_2) - I_0 e^{-\mu T(r_\perp)}}{R_2} \tag{2.19}$$

By substituting (2.19) into (2.17) and rearranging, one obtains

$$\left(-\frac{R_2\delta}{\mu} \nabla_\perp^2 + 1\right) e^{-\mu T(r_\perp)} = \frac{I(r_\perp, z=R_2)}{I_0} \tag{2.20}$$

Passing in the Fourier domain and substituting equation (2.21) in equation (2.20):

$$\mathcal{F}\left\{e^{-\mu T(r_\perp)}\right\} = \mu \frac{\mathcal{F}\{I(r_\perp, z=R_2)\}/I_0}{R_2\delta|k_\perp|^2 + \mu} \tag{2.21}$$

Taking the inverse Fourier transform and solving for $T(r_\perp)$ gives:

$$T(r_\perp) = -\frac{1}{\mu} log_e \left(\mathcal{F}^{-1} \left\{ \mu \frac{\mathcal{F}\{I(r_\perp, z=R_2)\}/I_0}{R_2\delta|k_\perp|^2 + \mu} \right\} \right) \tag{2.22}$$

For a weakly refracting object illuminated by a point source with R_1, the intensity I_{R_1} is related to I_∞ :

$$I_{R_1}(r_\perp, z) = \frac{1}{M^2} I_\infty \left(\frac{r_\perp}{M}, \frac{z}{M} \right) \tag{2.23}$$

With M = (R_1 + R_2) / R_1 as the magnification of the point source. Equation (2.22) can be written with (2.23) to be suitable for a point source:

$$T(r_\perp) = -\frac{1}{\mu} log_e \left(\mathcal{F}^{-1} \left\{ \mu \frac{\mathcal{F}\{M^2 I(M r_\perp, z=R_2)\}/I_0}{R_2\delta|k_\perp|^2/M + \mu} \right\} \right) \tag{2.24}$$

This result solves the transfer-intensity equation (2.14) for a homogenous object with a projected thickness of $T(r_\perp)$ by using one single defocused image. (Paganin, Mayo et al. 2002).

2.4.1.2. Holographic imaging

The transmission function $T(x) = a(x)\exp(i\varphi(x))$ with a(x) the absorption and $\varphi(x)$ the phase. In this paragraph, the assumption is made that the absorption of an object is small and can be neglected; therefore the transmission function of a pure phase object is $T(x) = \exp(i\varphi(x))$.

The Fourier transform of the intensity distribution for a Fresnel diffraction pattern at a given distance $D_m(m = 1, \dots, N)$ is given as: (Guigay 1977)

$$\tilde{I}_m(f) = \delta_D(f) + \tilde{R}_m(f) 2 \ sin(\pi\lambda D_m f^2)\, \tilde{\varphi}(f) + \tilde{I}_{NL,m}(f) \tag{2.25}$$

The non-linear part $\tilde{I}_{NL,m}(\mathbf{f})$, with $\mathbf{f}$ as the frequency, will be small if $|\varphi(s+\lambda D_m \boldsymbol{f})-\varphi(s)|$ "1 for all distances s. The Dirac distribution $\delta_{\mathrm{D}}(\mathrm{f})$ is the mean unit intensity. The multiplication factor $\tilde{R}_m(\mathrm{f}) = \tilde{R}(\mathrm{f})\gamma^c(\lambda \mathrm{D}_m \mathrm{f})$ has the detector transfer function $\tilde{R}(\mathrm{f})$ and the degree of spatial coherence $\gamma^c(\lambda \mathrm{D}_m \mathrm{f})$ in it. Because the contrast factor $2\ \sin(\pi\lambda D_{\mathrm{m}}\mathrm{f}^2)$ becomes zero for some spatial frequencies, multiple measurements of the intensity are needed. These multiple images are combined to reduce the non-linear term. Neglecting the non-linear term, a least-squares function approximation comes to the following estimation:

$$H(f)\tilde{\varphi}(f) = \frac{1}{N}\sum_{m=1}^{N} H_m(f)\,\tilde{I}_m^{exp}(f) \tag{2.26}$$

With

$$H_m(f) = \tilde{R}_m(f)2\ \sin(\pi\lambda D_m f^2) \tag{2.27}$$

And

$$H(f) = \frac{1}{N}\sum_{m=1}^{N} \tilde{R}_m^2(f)\ 2\ \sin^2(\pi\lambda D_m f^2) \tag{2.28}$$

By using the full description of the non-linear image formation process, this estimation can be optimized recursively.

2.4.2. Analyzer-based imaging

The analyzer-based imaging (ABI) technique employs an analyzer crystal placed between the sample and the detector. A highly coherent and collimated beam passes through the sample and gets angularly deviated due to the variation of the refractive index, as described in the formula (2.13). The analyzer crystal acts as an angular filter, rejecting all photons that do not meet the Bragg condition:

$$2a\ sin(\theta) = \lambda \tag{2.29}$$

With a as the distance between atoms in the lattice, θ the angle between the photon propagation direction and the lattice planes, and λ the wavelength of the photons. Only the diffracted/accepted X-rays can reach the detector and form the image (A. Bravin, 2003).

The monochromator crystal (Figure 2.5) and the analyzer crystal (Figure 2.5) of the ABI setup is not dispersive, but their reflecting surfaces are parallel. The rocking curve (RC) of the system is the convolution of the monochromator and the analyzer reflectivity curves, determined by the Bragg condition (equation (2.24)). The RC determines the filter function, which has an acceptance window (RC's full width at the half maximum FHWM) of a few microradians. For example, a 111 Silicon crystal for energy between 15 to 60 keV has an acceptance window (FWHM) of 17.6 to 4.3 µrad (XOP).[2] The analyzer crystal can be operated in Bragg or Laue condition, depending on their cut and configuration.

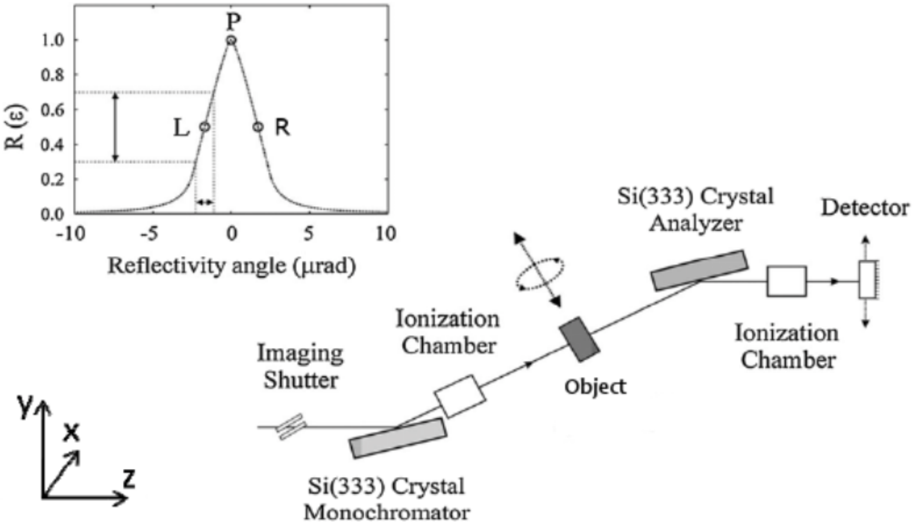

Figure 2.5 Schematic diagram of ABI setup The diffraction optics includes a monochromator and an analyzer crystal. The graph shows the reflectivity curve, R(ε), of silicon 333 (Si 333) reflection at 30 keV and the principle of the analyzer-based on X-ray imaging method (Keyriläinen, Fernández et al. 2008)

The ABI is only sensitive to X-rays' angular deflections in the direction parallel to the crystal diffraction plane.

$$\Delta\alpha(x, y) \simeq -\frac{\lambda}{2\pi}\frac{\partial\phi(x, y, \lambda)}{\partial y} \tag{2.30}$$

Axes are as in Figure 2.5. The intensity on the detector can be expressed as:

$$I_{ABI} = \frac{TI_0}{M^2}R(\theta_{an} + \Delta\alpha) \tag{2.31}$$

With M the magnification due to the divergence of the beam and θ_{an} the angular position of the analyzer crystal with respect to the Bragg angle for the selected photon energy. To get an ABI image, the analyzer crystal is placed at a different angle along with the RC. These images get combined, and by applying a sophisticated algorithm, contrast contributions such as the phase shift, absorption and scattering signals are retrieved. One of the first of these algorithms is the DEI algorithm (Chapman, Thomlinson et al. 1997), which needs two images at 50 % of the RC to extract the refraction and the absorption signals. This algorithm works on the Taylor expansion to the second-order; the small and ultra-small angle scattering (USAXS) is ignored. Another more advanced algorithm needs three images from the RC and a higher-order

---

[2] XOP: X-ray Oriented Program, Version 2.3, ESRF, Grenoble, France

Taylor expansion to extract the USAXS signal. (Chou, Anastasio et al. 2007, Rigon, Arfelli et al. 2007). An alternative algorithm using a gaussian function has been used to model the RC to extract the SAXS and USAXS signal (Oltulu, Zhong et al. 2003, Wernick, Wirjadi et al. 2003). For this algorithm, multiple images along the RC are needed.

2.4.3. Edge Illumination imaging

The group of Alessandro Olivo drove the development of the edge illumination method (EI) within the last 15 years. The basic idea was to enhance the phase sensitivity of an imaging system by illuminating only the edge of the active surface of a detector pixel. In this way, photons, which are not hitting the active surface, can be deviated onto it due to an interaction with the sample (Olivo and Speller 2007). This leads to an increase or decrease of photon counts in the pixel, depending on the direction they get refracted. This method can be performed with synchrotron radiation or with conventional, non-micro focal X-ray tubes.

The setup (Figure 2.6) of this technique uses a pre-sample coded aperture mask ('sample mask' in the following), which slices the incoming beam into small sub-beams. The aperture mask is located upstream of the sample. The aperture blocks the incoming beam in a way that the sub-beams are not interfering with each other. Therefore, the edge illumination is not an interfering method. There is a second aperture right in front of the detector. This is called a post-sample coded aperture mask ('detector mask' in the following). The detector mask covers the detector in a way that there are an active area and an inactive one of the pixels. The detector mask is designed so that the period[3] has the same dimension as the detector pixel. The detector mask is aligned in a way that every detector pixel is blocked half by the detector mask and can be illuminated by X-rays on the other half (see Figure 2.6). The sample mask can be moved orthogonally to the beam direction and parallel concerning the detector mask. In the absence of the sample, the detector mask is fixed, and the sample mask is moved over one period so that an illumination curve is recorded. This illumination curve is related to the intensity measured at each pixel when changing the beamlet physically. This is analog to the rocking curve in ABI.

When placing a sample downstream of the sample mask, this changes the measured intensity. If two images are recorded, with two different misalignments of sample mask regarding the detector mask, corresponding to opposite sides of the illumination curve, the signal coming from refraction is reversed, but the absorption signal remains the same. Therefore, the refraction signal and the absorption signal can be separated with a phase retrieval algorithm using only these two images. (Diemoz, Hagen et al. 2013). With a 1D mask, the sensitivity of the phase is only in the direction of scanning. This can be overcome with a 2D mask (Kallon, Wesolowski et al. 2015).

---

[3] Width of a blocking element plus width of slit.

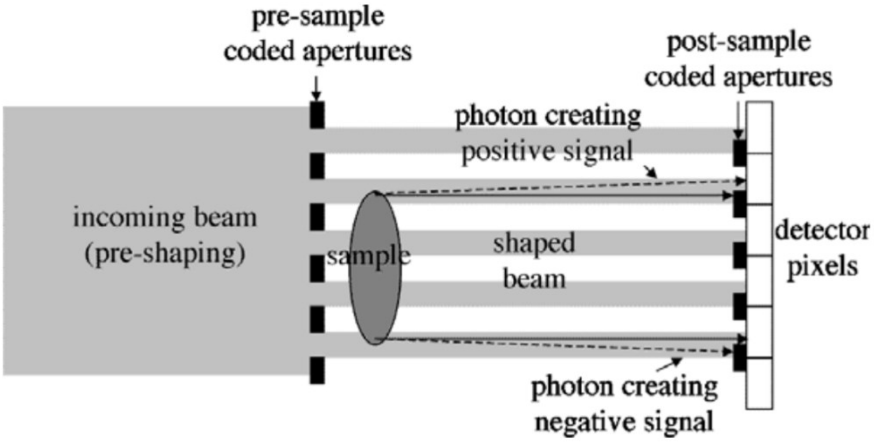

Figure 2.6 Schematic of the concept of the coded-aperture technique; the detector gets partly covert, an increase or decrease in intensity is reported depending on the refraction of the object. (Olivo and Speller 2007)

2.4.4. Grating interferometry

Grating interferometry (GI) or X-ray Talbot interferometry is a PCI technique, which is based on the interference of photons. The setup uses a phase grating and an analyzer grating, which are placed between the sample and the detector, as shown in Figure 2.7.

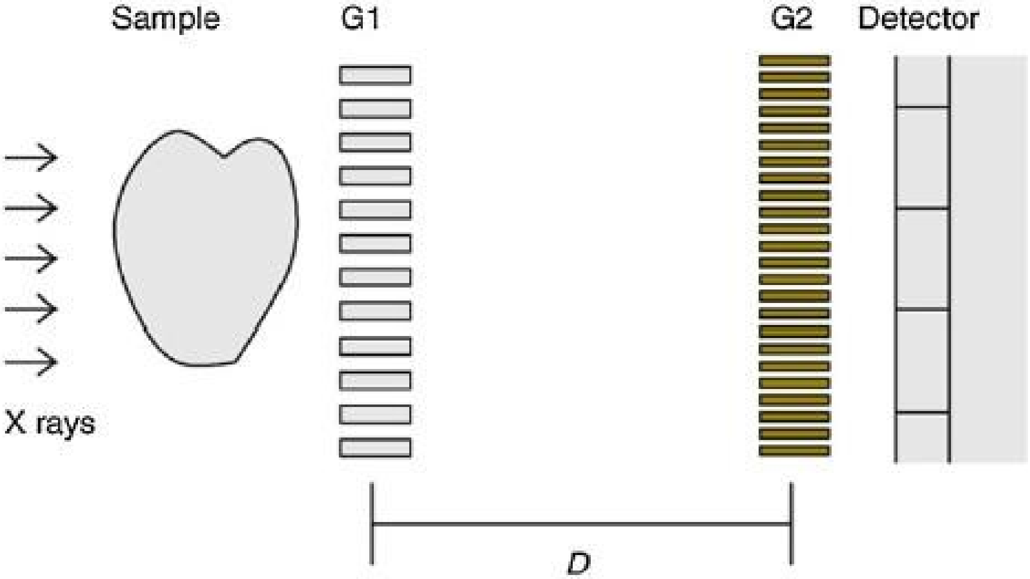

Figure 2.7 Setup of a grating interferometer: With the beam splitter G1,- a pattern of X-ray interference fringes is formed; the local distortions from its ideal regular shape enclose information on the sample structure. The fringes are too small to be resolved by the pixel detector; an additional analyzer grating (G2) in front of the detector is placed on transforming fringe-position information into intensity. (Weitkamp, David et al. 2008)

This technique's basic physical principle is the so-called optical Talbot effect, a near field diffraction effect first observed by Henry Fox Talbot in 1837 (Talbot 1837). When an incident wavefront passes through a diffraction grating, the image is repeated after certain distances. This regular distance is called the Talbot length d_t and can be expressed by this formula: $d_t = 2a^2/\lambda$ with a, as the period of the gratings and λ the wavelength of the incident light. The so-created interference pattern impinges on the sample with which it interacts. The absorption and scattering mechanisms experienced by the photons cause a local change in beam intensity. To retrieve this distortion of the interference pattern, the signals with and without samples are both acquired. A detector with a pixel size suitable to sample the interference fringes and a high photon flux is needed. This is why a second grating (the so-called absorption grating) is placed close to the detector and at a distance equal to the Talbot length. This grating is used to analyze the interference pattern. Two methods are used to separate the signal's different components; one is called phase stepping (Weitkamp, Diaz et al. 2005) and one Moiré fringes (Atsushi, Shinya et al. 2003).

An excellent spatial coherence is needed. To use a laboratory X-ray tube, a third grating is added just downstream the photon source (Talbot-Lau interferometer(Talbot 1836)) and before the sample (Weitkamp, Diaz et al. 2005).

2.5. Computed Tomography (CT)

In conventional radiographs, a 2D image is acquired, a projection of transmitted X-rays of a 3D sample but only in one direction. The depth information is lost on this radiograph. Computed Tomography (CT) overcomes this issue by combining different radiographs from different angles in order to get a 3D representation of the sample. Johann Radon laid the mathematical foundation for tomography by giving a solution for reconstructing a function from its projections; the method is presented in the article "Über die Bestimmung von Funktionen durch ihre Integralwerte längs gewisser Mannigfaltigkeiten" in 1917 (Radon 1917). More than 50 years later, Godfrey Hounsfield took the first medical tomographic image in 1973 (Hounsfield 1973).

There are two types of reconstruction algorithms: the analytical methods (Fourier transformation) and the iterative methods (algebraic and statistical).

The filtered back projection is the most commonly used algorithm for reconstruction (Kak and Slaney 1988, Herman 2009). Every projection gets convolved with a filter function to prevent star artifacts from occurring. The filtered projection is projected backward along the original line of sight, and the relevant physical parameter (i.e., photon attenuation) is summed up. This can also be applied for the refraction of X-rays because the change in phase introduced by an object is linearly proportional to the refractive decrement in the refraction index.

3D anatomical Planes

Three standard anatomic planes are also used to display data for *CT* scans. They are:

- Axial slice – slice which is perpendicular to the rotation axis
- Sagittal slice – parallel to the rotation axis and orthogonal to the shoulder plane
- Coronal slice – is parallel to the rotation axis and the shoulder plane of a human

This terminology is in the analogy of the anatomical plane used by medical doctors.

Coordination system

The coordination system used in this thesis is characterized in the following:

- the z-direction is the direction X-ray are traveling
- the x-direction is perpendicular to the travel of X-rays and is parallel to the horizon/ground of the earth
- y-direction is orthogonal to the travel of X-rays, and the x-direction

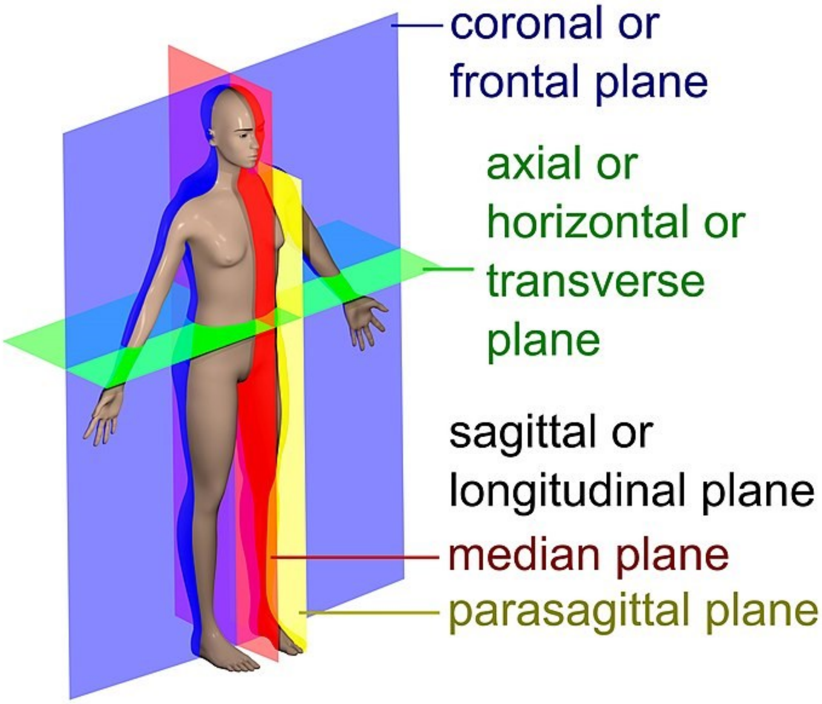

Figure 2.8 anatomical planes used in anatomy in this thesis a similar terminology is used; the axial plane is perpendicular to the rotation axis, coronal and sagittal plane is parallel to the rotation axis[4]

---

[4] https://en.wikipedia.org/wiki/File:Human_anatomy_planes,_labeled.jpg downloaded: 15.3.19

Bibliography

Als-Nielsen, J. and D. McMorrow (2011). Elements of modern X-ray physics, John Wiley & Sons.

Arhatari, B. D., A. P. Mancuso, A. G. Peele and K. A. Nugent (2004). "Phase-contrast radiography: Image modeling and optimization." Review of Scientific Instruments **75**(12): 5271-5276.

Atsushi, M., K. Shinya, K. Ichiro, H. Yoshitaka, T. Kengo and S. Yoshio (2003). "Demonstration of X-Ray Talbot Interferometry." Japanese Journal of Applied Physics **42**(7B): L866.

Born, M. and E. Wolf (1999). Principles of Optics: Electromagnetic Theory of Propagation, Interference and Diffraction of Light. Cambridge, Cambridge University Press.

Chapman, D., W. Thomlinson, R. E. Johnston, D. Washburn, E. Pisano, N. Gmür, Z. Zhong, R. Menk, F. Arfelli and D. Sayers (1997). "Diffraction enhanced x-ray imaging." Physics in Medicine & Biology **42**(11): 2015.

Chou, C.-Y., M. A. Anastasio, J. G. Brankov, M. N. Wernick, E. M. Brey, D. M. Connor Jr and Z. Zhong (2007). "An extended diffraction-enhanced imaging method for implementing multiple-image radiography." Physics in Medicine & Biology **52**(7): 1923.

Cloetens, P., W. Ludwig, J. Baruchel, D. Van Dyck, J. Van Landuyt, J. P. Guigay and M. Schlenker (1999). "Holotomography: Quantitative phase tomography with micrometer resolution using hard synchrotron radiation x rays." Applied Physics Letters **75**(19): 2912-2914.

Diemoz, P. C., C. K. Hagen, M. Endrizzi and A. Olivo (2013). "Sensitivity of laboratory based implementations of edge illumination X-ray phase-contrast imaging." Applied Physics Letters **103**(24).

Guigay, P. (1977). "Fourier-transform analysis of Fresnel diffraction patterns and in-line holograms." Optik **49**: 121-125.

Gureyev, T., C. Raven, A. Snigirev, I. Snigireva and S. Wilkins (1999). "Hard x-ray quantitative non-interferometric phase-contrast microscopy." Journal of Physics D: Applied Physics **32**(5): 563.

Herman, G. T. (2009). Fundamentals of computerized tomography: image reconstruction from projections, Springer Science & Business Media.

Horng, A., E. Brun, A. Mittone, S. Gasilov, L. Weber, T. Geith, S. Adam-Neumair, S. D. Auweter, A. Bravin, M. F. Reiser and P. Coan (2014). "Cartilage and Soft Tissue Imaging Using X-rays: Propagation-Based Phase-Contrast Computed Tomography of the Human Knee in Comparison With Clinical Imaging Techniques and Histology." Investigative Radiology **49**(9): 627-634.

Hounsfield, G. N. (1973). "Computerized transverse axial scanning (tomography): Part 1. Description of system." The British Journal of Radiology **46**(552): 1016-1022.

Jackson, J. D. (1999). Classical electrodynamics. New York, {NY}, Wiley.

Kak, A. C. and M. Slaney (1988). "Principles of computerized tomographic imaging. The Institute of Electrical and Electronics Engineers." Inc., New York.

Kallon, G. K., M. Wesolowski, F. A. Vittoria, M. Endrizzi, D. Basta, T. P. Millard, P. C. Diemoz and A. Olivo (2015). "A laboratory based edge-illumination x-ray phase-contrast imaging setup with two-directional sensitivity." Applied Physics Letters **107**(20): 204105.

Keyriläinen, J., M. Fernández, M.-L. Karjalainen-Lindsberg, P. Virkkunen, M. Leidenius, K. v. Smitten, P. Sipilä, S. Fiedler, H. Suhonen, P. Suortti and A. Bravin (2008). "Toward High-Contrast Breast CT at Low Radiation Dose." Radiology **249**(1): 321-327.

Kitchen, M. J., R. A. Lewis, N. Yagi, K. Uesugi, D. Paganin, S. B. Hooper, G. Adams, S. Jureczek, J. Singh, C. R. Christensen, A. P. Hufton, C. J. Hall, K. C. Cheung and K. M. PAvlov (2005). "Phase-contrast X-ray imaging of mice and rabbit lungs: a comparative study." The British Journal of Radiology **78**(935): 1018-1027.

Larsson, D. H., W. Vågberg, A. Yaroshenko, A. Ö. Yildirim and H. M. Hertz (2016). "High-resolution short-exposure small-animal laboratory x-ray phase-contrast tomography." Scientific reports **6**: 39074.

Momose, A. and J. Fukuda (1995). "Phase-contrast radiographs of nonstained rat cerebellar specimen." Medical Physics **22**(4): 375-379.

Olivo, A. and R. Speller (2007). "Modelling of a novel x-ray phase-contrast imaging technique based on coded apertures." Physics in Medicine & Biology **52**(22): 6555.

Oltulu, O., Z. Zhong, M. Hasnah, M. N. Wernick and D. Chapman (2003). "Extraction of extinction, refraction and absorption properties in diffraction enhanced imaging." Journal of Physics D: Applied Physics **36**(17): 2152.

Paganin, D., S. Mayo, T. E. Gureyev, P. R. Miller and S. W. Wilkins (2002). "Simultaneous phase and amplitude extraction from a single defocused image of a homogeneous object." Journal of microscopy **206**(1): 33-40.

Paganin, D., S. C. Mayo, T. E. Gureyev, P. R. Miller and S. W. Wilkins (2002). "Simultaneous phase and amplitude extraction from a single defocused image of a homogeneous object." Journal of Microscopy **206**(1): 33-40.

Peter, C., B. Raymond, B. José, G. Jean-Pierre and S. Michel (1996). "Phase objects in synchrotron radiation hard x-ray imaging." Journal of Physics D: Applied Physics **29**(1): 133.

Radon, J. (1917). "Über die Bestimmung von Funktionen durch ihre Integralwerte längs gewisser Mannigfaltigkeiten." Berichte über die Verhandlungen der Königlich-Sächsischen Gesellschaft der Wissenschaften zu Leipzig **69**(Mathematisch-Physische Klasse): 262-277.

Raven, C., A. Snigirev, I. Snigireva, P. Spanne, A. Souvorov and V. Kohn (1996). "Phase-contrast microtomography with coherent high-energy synchrotron x rays." Applied Physics Letters **69**(13): 1826-1828.

Rigon, L., F. Arfelli and R.-H. Menk (2007). "Three-image diffraction enhanced imaging algorithm to extract absorption, refraction, and ultrasmall-angle scattering." Applied Physics Letters **90**(11): 114102.

Röntgen, W. C. (1896). " Ueber eine neue Art von Strahlen (Vorläufige Mittheilung)." Stahel'sche K. Hof- und Universitätsbuch- und Kunsthandlung **1**: 1.

Snigirev, A., I. Snigireva, V. Kohn, S. Kuznetsov and I. Schelokov (1995). "On the possibilities of x-ray phase-contrast microimaging by coherent high-energy synchrotron radiation." Review of Scientific Instruments **66**(12): 5486-5492.

Talbot, H. F. (1836). "LXXVI. Facts relating to optical science. No. IV." The London, Edinburgh, and Dublin Philosophical Magazine and Journal of Science **9**(56): 401-407.

Talbot, H. F. (1837). "LXXII. An experiment on the interference of light." The London, Edinburgh, and Dublin Philosophical Magazine and Journal of Science **10**(62): 364-364.

Weitkamp, T., C. David, O. Bunk, J. Bruder, P. Cloetens and F. Pfeiffer (2008). "X-ray phase radiography and tomography of soft tissue using grating interferometry." European Journal of Radiology **68**(3, Supplement): S13-S17.

Weitkamp, T., A. Diaz, C. David, F. Pfeiffer, M. Stampanoni, P. Cloetens and E. Ziegler (2005). "X-ray phase imaging with a grating interferometer." Optics Express **13**(16): 6296-6304.

Wernick, M. N., O. Wirjadi, D. Chapman, Z. Zhong, N. P. Galatsanos, Y. Yang, J. G. Brankov, O. Oltulu, M. A. Anastasio and C. Muehleman (2003). "Multiple-image radiography." Physics in Medicine & Biology **48**(23): 3875.

Wilkins, S. W., T. E. Gureyev, D. Gao, A. Pogany and A. W. Stevenson (1996). "Phase-contrast imaging using polychromatic hard X-rays." Nature **384**: 335.

Zachariasen, W. H. (2004). Theory of X-Ray Diffraction in Crystals, Dover Publications.

Zhou, T., U. Lundström, T. Thüring, S. Rutishauser, D. H. Larsson, M. Stampanoni, C. David, H. Hertz and A. Burvall (2013). "Comparison of two x-ray phase-contrast imaging methods with a microfocus source." Optics express **21**(25): 30183-30195.

3. Experimental facilities and setups

The experiments presented in this Thesis manuscript were carried out by using different X-ray light sources. Most of the work has been performed at synchrotron radiation (SR) facilities. Still, for comparison, other sources like rotating anode X-ray tubes and the recently developed liquid metal jet X-ray sources have been used too. In this chapter, I will provide a brief description of the X-ray facilities and beamlines, where I have realized my experimental work, and I will describe the main characteristics of the used X-ray beams.

3.1. Synchrotron radiation

In 1947, a group at the General Electric Synchrotron Facility in New York reported that they saw an "arc in the tube" when they switched on their 70 MeV particle accelerator. Lamgmuir realized that this was a beam of light named 'synchrotron radiation' (Elder, Gurewitsch et al. 1947). In 1968 the first spectrum of the Tatantalus I Synchrotron with a storage ring (first generation) was measured at the University of Wisconsin. This storage ring was used for a two-fold purpose: as a source of X-rays and for positron-electron collision experiments at the same time. The facility evolved in the next years and had, at its peak, ten beamlines, which were operational at the same time. This concept served as a model for the modern multi-user synchrotron facilities (Robinson 2009). Because of the multipurpose of first-generation synchrotrons, the ring current was still low as needed for the collision experiments. The second generation of synchrotrons was built with the only scope of producing X-ray beams. The first one of this generation was built in 1981 at the Daresbury Laboratory in the United Kingdom and had a 2-GeV electron storage ring. The third generation of synchrotron sources was constructed to improve the machine's emittance and brightness and introduced insertion devices, such as undulators and wigglers. The first third-generation was the European Synchrotron Radiation Facility (ESRF) in Grenoble, with its 6 GeV storage ring, which started its operation in 1994 (Kunz 2001). Besides the ESRF, there are other third-generation Synchrotrons, which are operational today, like the Advanced Photon Source in Chicago, US or the Spring 8 (Super photon ring – 8 GeV) in Japan. Other intense sources, i.e., the free-electron lasers (FEL), have been developed in parallel. They accelerate electron linearly and use undulators. FELs are improving the brightness and pulse length compared to the third generation of synchrotrons. The first one with "hard" X-ray was the Linear Coherent Light Source at the National Accelerator Laboratory in California, which started its operation in 2009 (McNeil 2009). Nowadays, major synchrotron facilities, such as the ESRF, have started or will soon start an important upgrade program, aiming to increase the brilliance of synchrotron radiation, setting the basis for new science shortly.

3.1.1. Synchrotron source

Synchrotron radiation is the electromagnetic field emitted by a relativistic charged particle moving in a homogeneous magnetic field. The force, which a charged particle moving with a momentum $\vec{p} = m\vec{v}$ experiences in a constant magnetic field $\vec{\mathrm{B}}$, is called the Lorentz force $\vec{L} = \frac{d\vec{p}}{dt} = -e\vec{v} \times \vec{\mathrm{B}}$. The produced radiation is highly collimated and emitted in the tangential direction of the trajectory of the electron within the field $\vec{\mathrm{B}}$. The emitted spectrum can be described with the critical wavelength, which is the wavelength. This value is defined as the wavelength where half of the total power is radiated: $\lambda_c = \frac{4\pi}{3}\frac{R}{\gamma^3}$ with R the radius of the curvature and γ speed of the electrons ($\gamma = 1/\sqrt{(1-(v/c)}^{2}$, with v the velocity of an electron). The emitted synchrotron cone's opening angle is given by 1/γ (Baruchel, Hodeau et al. 1993).

There are bending magnets, wigglers, and undulators installed along the electron beam. A bending magnet consists of only one magnet. In contrast, wigglers and undulators (i.e. insertion devices) have multiple magnets ordered in an opposite magnetic direction along the electron beam to force the electrons on a sinusoidal course through the device. The optical properties of a wiggler and undulator can be described by the K value, a dimensionless parameter defined as $= \alpha\gamma$, with α the wiggling angle of the trajectory (Figure 3.1).

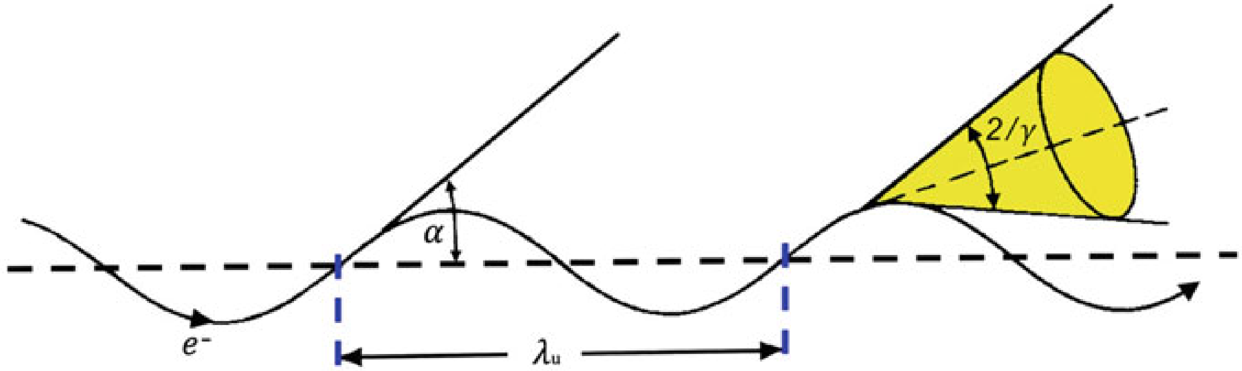

Figure 3.1 Schematic view of the electron trajectory of a wiggler, with $\boldsymbol{\alpha}$ *the wiggling angle of the trajectory and* $\boldsymbol{\lambda_u}$ *the period of the magnets (Balerna and Mobilio 2015)*

The K value for electrons can be written as $K = \frac{e}{2\pi\, mc}\boldsymbol{\lambda_u B_0} = \mathbf{0.934}\boldsymbol{\lambda_u}[\boldsymbol{cm}]\boldsymbol{B_0}[\boldsymbol{Tesla}]$. Wiggler has a K larger than 1; the emitted pulses do not interfere with each other. For undulators, $K \approx 1$ and α is in the order of the photon emission angle 1/γ (Balerna and Mobilio 2015), thus the different photon beamlets produced as each curve of the electrons within the undulator interfere

3.1.2. Synchrotron Radiation characteristics

Several aspects of an X-ray source determine the quality of the X-ray beam it produces. They can be combined into a single quantity called *brilliance B*, defined as:

$$\boldsymbol{brillance} = \frac{\boldsymbol{photons\ per\ sec}}{\boldsymbol{divergences(mm^2)\ source\ area(mm^2)\ energybandwith(0,1\%\ BW)}} \tag{3.1}$$

In other words, the brilliance is the photon density in a given time for a specific area within a specific energy bandwidth. The energy spectrum of a synchrotron source can go from infrared light until hard X-ray; this depends on the insertion device used to produce the light.

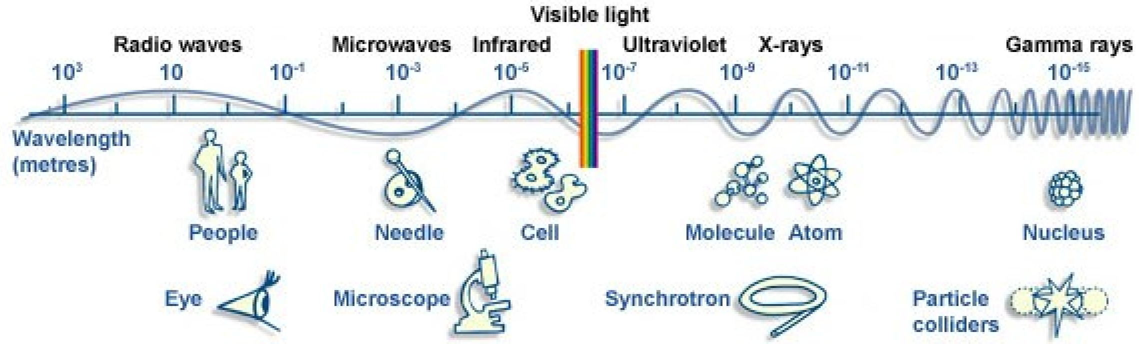

Figure 3.2 A sketch about the entire electromagnetic spectrum with a comparison of the wavelength with objects and the observer method to visualize the object.[5]

Synchrotron radiation is characterized by a high degree of coherence (paragraph 2.3 Coherence), making experiments possible, which are difficult with other X-ray sources. The coherence can be regarded as the property of radiation that enables a wave to produce observable interference and diffraction effects. For example, a monochromatic plane wave is, in this sense, perfectly coherent, while the light emitted by a standard light bulb is entirely incoherent.

3.1.3. The European Synchrotron (ESRF)

The European Synchrotron Radiation Facility has recently started an upgrade program called "Extremely Brilliant Source", which foresees the **construction of a new – the first of a kind – storage ring and new beamlines.** The new machine parameters are reported in the so-called Orange book, i.e. the technical design study (Dimper, Reichert et al. 2015). The machine that I will describe here is the one that was running until December 2018 (before the upgrade) and with which I have performed the experiments included in this Ph.D. Thesis work.

The ring has a circumference of about 844 m and an electron beam energy of 6.04 GeV. The electron beam current could be up to 200 mA (depending on the filling mode of the electron ring), and the natural emittance was 4000 pm×rad, and it had an energy spread of 0.106 % (Dimper, Reichert et al. 2015). Forty-two beamlines were operational simultaneously.

---

[5] http://www.esrf.eu/files/live/sites/www/files/about/synchrotron-science/emspectrum.jpg Download: 30.11.18

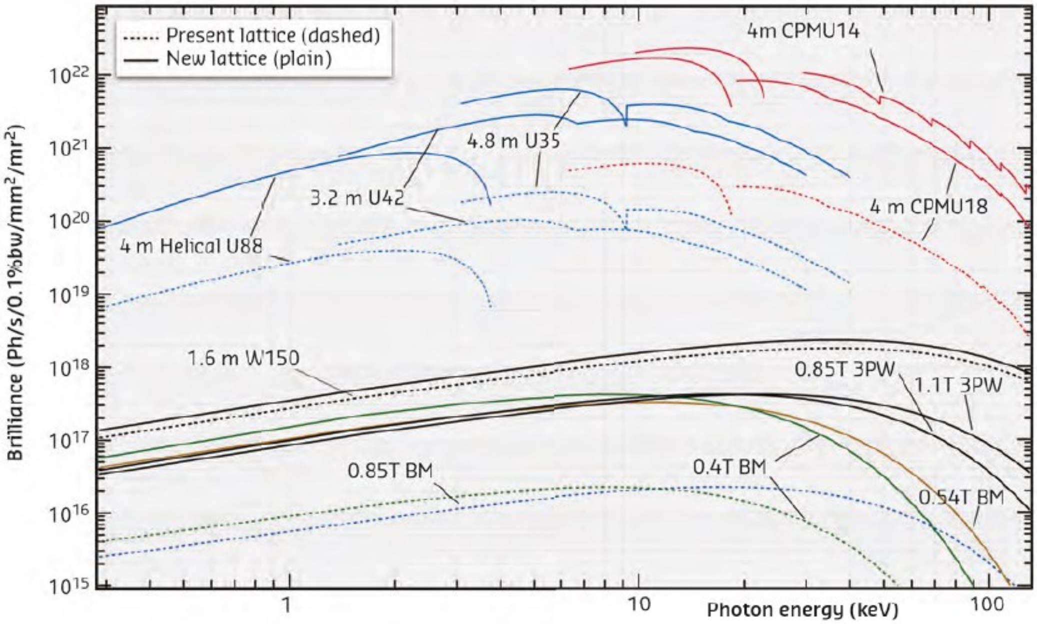

Figure 3.3 Brilliance for Bending Magnets (BM) sources, undulator sources (U or CPMU (cryogenic permanent magnet undulator and wiggler (W150), for the existing and the new machine, Bending Magnets BM (Dimper, Reichert et al. 2015)

In Figure 3.3 Brilliance for Bending Magnets (BM) sources, undulator sources (U or CPMU (cryogenic permanent magnet undulator and wiggler (W150), for the existing and the new machine, Bending Magnets BM (Dimper, Reichert et al. 2015) The current machine can have a brilliance up to 10^{21} photons/s/0.1%bw/mm^2/mr^2 with a CPMU18 undulator. With the new lattice, this undulator gains a factor of 10 in flux, whereas the W150 wiggler does not gain much flux from this new lattice.

3.1.4. The Swiss Light Source synchrotron (SLS)

The Swiss Light Source (SLS) at the Paul Scherrer Institute (PSI) in Villingen Schwitzerland, has a storage ring with 288 m of the circumference and electron energy of 2,5 GeV. There are 17 beamlines operational (Böge 2002). The beam current is 400 mA; this number is kept constant using the so-called top-up mode for the storage ring injection. This means that every 2-3 min, there is a 2 mA electron current injected in the storage ring (Ludeke and Munoz 2002). The beam emittance is 5.5 nm rad; this is achieved using 177 quadrupole magnets to focus the beam. The synchrotron radiation spectrum produced by undulators ranges from ultraviolet to hard X-rays (Andersson, Böge et al. 2008).

3.2. The ESRF Biomedical Beamline (ID17)

The ID17 beamline is one out of three long beamlines at the ESRF, with a total length of 150 m. It is entirely dedicated to biomedical research, including imaging and radiotherapy programs. At a 40 m distance from the SR source, an experimental hutch called the 'MRT hutch', where the high resolution "pink" beam experiments of this Thesis work took place. The second experimental hutch is located 150 m away from the source; it is called imaging hutch. The experiments with the monochromatic beam of this Thesis were done in this hutch.

3.2.1. The ID17 source

The ID17 beamline has two wigglers as insertion devices and X-ray sources. The first wiggler (W150) has 21 poles and an adjustable gap, a period of 150 mm and a maximum magnetic field of 1.6 T at a minimum gap of 24.8 mm. This wiggler has critical energy of 38.1 keV (unfiltered radiation); the K value is between 5 and 25 depending on the gap (magnetic field). The second wiggler (w125) has 22 poles with a 125 mm period and a maximum magnetic field of 1.8 T at a gap of 11 mm. The second wiggler can be added to the first one to increase the photon flux.

The source size has been calculated at 50 keV to be about 162 µm FHWM wide (horizontally) and 8 µm FHWM high vertically (LAISSUE, LE BASZ et al. 2000). Both hutches can be used for imaging. The X-ray beam is 65 mm wide (50 keV FWHM) and 3.1 mm high (50 keV FWHM) at the sample position in the MRT hutch. In the second hutch, the X-ray beam is at the detector position about 258 mm (FWHM) wide and 12.8 mm high (FWHM), at 50 keV. These beam dimension estimations have been obtained by using the OrAnge SYnchrotron Suite (OASYS) toolset [6].

The X-ray beam entering the second experimental hutch is monochromatic. Different monochromator systems are available at ID17, but for our experiments, we always used a Si(111) double bent Laue crystal. It gives a quasi-monochromatic beam ($\Delta E/E \approx 10^{-4}$) in the range of 25 keV – 100 keV (Suortti, Fiedler et al. 2000).

The X-ray spectrum is shown in Figure 3.4 Polychromatic spectrum of ID17 MRT hutch, calculated by a tool based on the XOP software. This wiggler W150 was used in the experiments at ID17 in this Thesis. The gap of the wiggler was set to 110 mm, and the machine current was 200 mA. Two filters are added to shape this spectrum: a 1.52 mm Aluminum and a 1.06 mm Cooper filter. The peak energy is 42.8 keV. The calculations from this spectrum come from XOP software developed at the ESRF[7].

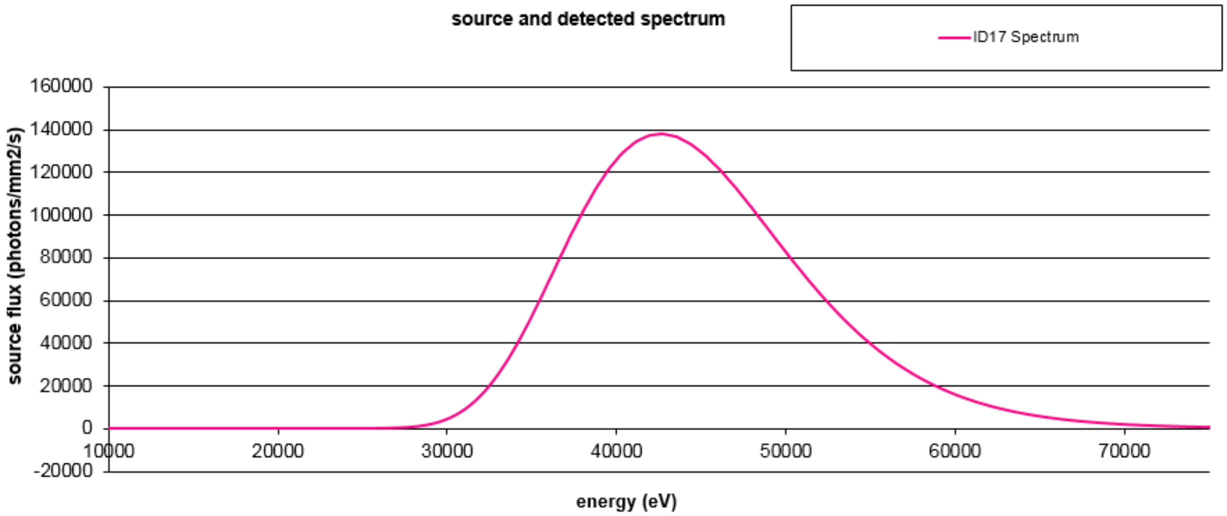

Figure 3.4 Polychromatic spectrum of ID17 MRT hutch, calculated by a tool based on the XOP software.

---

[6] http://ftp.esrf.eu/pub/scisoft/Oasys/ viewed:5.3.2019

[7] http://ftp.esrf.fr/pub/scisoft/xop2.3/ viewed: 5.3.2019

3.2.2. Experimental imaging setups

In the MRT hutch, the stage for micro-CT acquisitions can be positioned at different distances from the imaging detector (minimum 30 cm, maximum 2 m). The sample stage has at its bottom a motorized platform that can move in the vertical direction. The base platform is for a rough vertical adjustment. On top of that platform, a vertical motor stage with a range of 90 mm is placed. This motor can translate vertically with a precision below 3 µm.

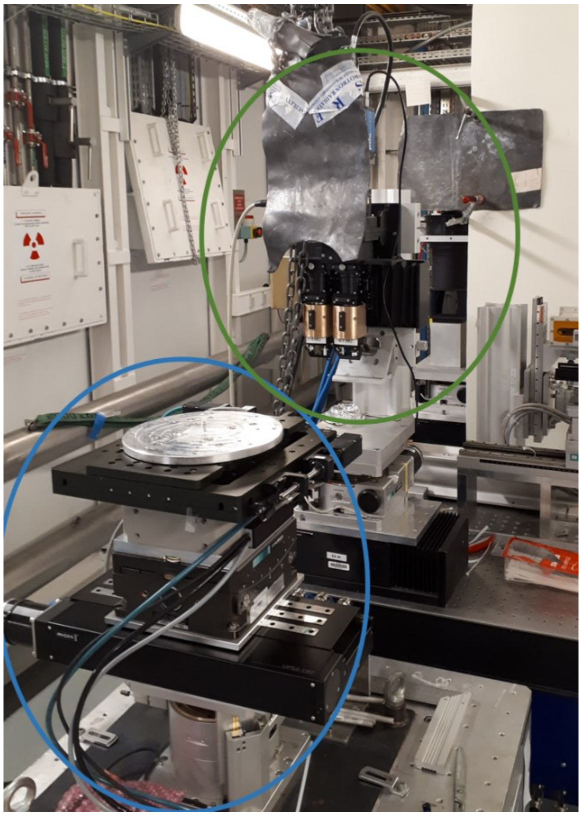

Figure 3.5 Picture of the sample stage and the detector system of the high resolution setup in the MRT hutch of the ID17; blue circle is the sample stage; green circle is the detector system with two different optical magnifications; by courtesy of Alberto Mittone

The setup tank includes a motor stage to move the sample horizontally and transversally with respect to the X-ray beam axis. The range of this displacement is about 150±0.001 mm. This stage is used to move the sample in and out of the beam and take reference images. Then there is a cradle motor stage on the top of that stage, which aligns the sample stage parallel to the beam direction. The next layer is the rotation stage, which is an air bearing to reduce friction. On top of that are two motor stages, which displace the sample in two linear directions, along the X-ray beam axis and the perpendicular direction. These displacements adjust the sample with respect to the center of rotation of the CT stage.

In the second hutch, there are two sample stages available; one at a fixed distance from the detector (12 m) and on a movable that can be placed between 3.4 m and 20 cm from the detector.

At the ID17 beamline, many imaging techniques are available. Propagation-based X-ray phase-contrast imaging with monochromatic and polychromatic X-rays is possible. There is an Edge Illumination setup available, with two masks, a sample, and a detector mask. An analyzer-based imaging X-ray phase-contrast imaging setup is also installed; the setup can be used in the second experimental hutch.

3.2.3. Detection systems

At the ID17 beamline, the X-ray imaging detector system portfolio includes different devices. There is a germanium detector cooled with liquid nitrogen. It consists of two monolithic germanium crystals with a length of 160 mm and a height of 10 mm electronically divided in 432 pixels. Therefore the pixel lateral (horizontal) size is 350 µm. Nowadays, this detector is mainly used for patient positioning (LAISSUE, LE BASZ et al. 2000) in radiotherapy programs performed at the beamline

The other detector available is the FreLoN camera developed at the ESRF and characterized by fast readout and low noise. This CCD camera is coupled to an optical system de-magnification lens system. The effective pixel size with this system is about 7,5 µm x 7,5 µm, the field of view is 15,3 mm x 15,3 mm (Mittone 2015). For the highest spatial resolution imaging experiments, a PCO Edge 5.5 detector is used, a metal-oxide-semiconductor (CMOS). This detector can be coupled with a different scintillator (fluorescent screens) depending on the spatial resolution to be achieved (i.e., on the microscope optics used). One of these scintillators is made of Lutetium Aluminum Garnet (LuAG) and has a thickness of 50 µm or 21 µm. With the 1x lens-based optics, an effective pixel size of 6.2 µm can be achieved. Other microscope optics allow 2x and 10x magnifications, providing effective pixel sizes of 3.1 µm and 0.7 µm, respectively (Mittone, Manakov et al. 2017). All images acquired in the experiments at the ID17 in this work were taken by using the PCO Edge 5.5.

3.3. The ESRF ID16a Nano-Imaging Beamline

ID16a is one of the most recently built beamlines at the ESRF, and it is one out of three longest located outside the synchrotron ring walls in satellite buildings. Long beamlines, i.e. long source-to-sample distances, allow to increase the degree of spatial coherence and to obtain larger beam sizes, where required. This beamline's mission is to address problems in biology, biomedicine, and nano-technology with X-ray fluorescence and nanotomography.

3.3.1. The ID16a source

The beamline source consists of two undulator insertion devices, called the U18_3 and the U22_4. The U18_3 has 152 periods with a period length of 18.3 mm; the deflection parameter K is 0.49, the photon energy range is 16.9 – 18.1 keV. At 17 keV, this source has a brightness of 8.2 x 10^{20} ph/s/mrad^2/mm^2. The U22_4 undulator has 124 periods of 22.4mm in length. The K parameter is 0.88, and it covers the energy range of 33-40 keV. The brightness is 2 x 10^{19} ph/s/mrad^2/mm^2 at 33.4 keV (Dr. Cecilia Blasetti 2018). The beamline operates at these two selected energies, 17 keV and 33.4 keV.

3.3.2. Experimental setups

The sample stage is placed at 185 m away from the source and is in a vacuum chamber with a base pressure of $10^{-7} – 10^{-8}$ mbar. Before the sample stage, there is a Kirkpatrick-Baez (KB) mirror, which focuses the beam down to a size of 13 nm (FWHM) at 33.4 keV (Cesar da Silva, Pacureanu et al. 2017).

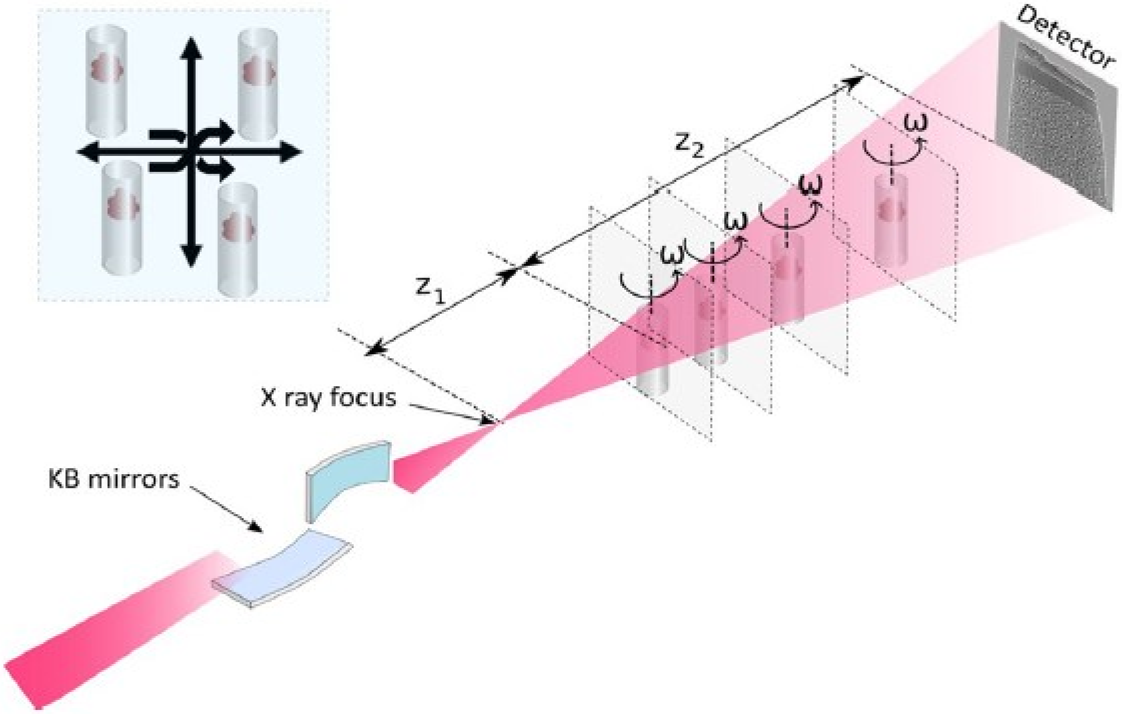

Figure 3.6 Schematic representation of the ID16a experimental setup with a KB mirror and images was taken at a different distance from the focal spot; the inset represents the sample's random displacement to improve image quality (Hubert, Pacureanu et al. 2018).

After the focus, the sample is placed on a hexapod with piezo controlled motor stages used for the nanometer sample alignment and movements during the CT acquisition. The sample is displaced by a random number of pixels orthogonally to the beam direction between two successive angular projections of the tomography scan. This is not compatible with a continuous tomographic scan; thus, a step-by-step acquisition is chosen. This method's result is that the scanning times are long(synchrotron micro-CT with 0.7 µm pixel size at ID17: 7 min scan time – holotomography scan with 0.1 µm pixel: 4 x 1 hour scan time). However, this random sample movement improves the reconstructed image quality because the ring artifact gets removed (Hubert, Pacureanu et al. 2018). The entire sample stage and the vacuum chamber are constructed to be very stable to achieve nanometer precision.

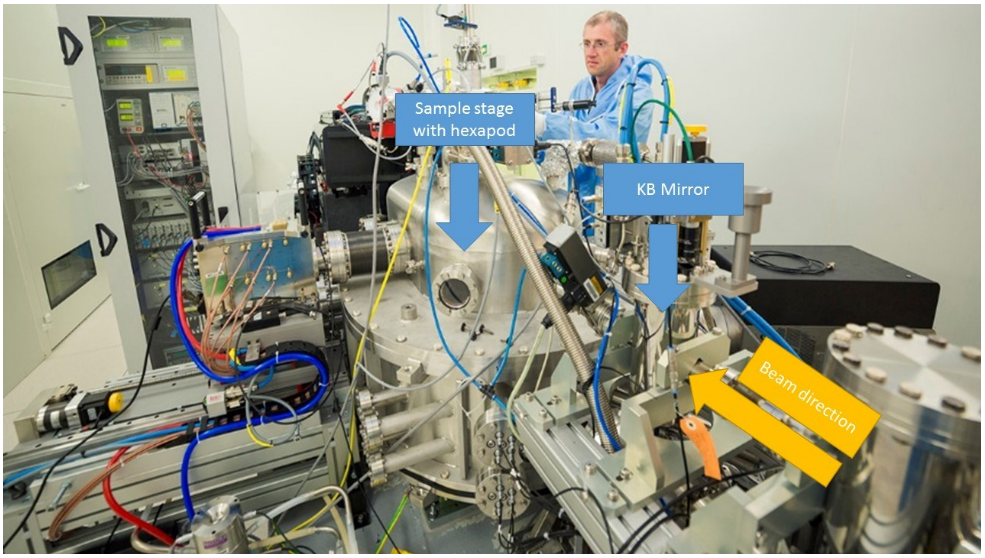

Figure 3.7 Picture of the end station at the ID16A Beamline at the ESRF, the beam gets focused by a KB mirror, the sample receives placed firmly after focusing spot achieve a small effective pixel due to the magnification effect[8]

3.3.3. Detection System

The detection system is a FReLON CCD camera coupled with a GGG:Eu ($Gd_3Ga_5O_{12}$:Eu) scintillator. The pixel size is 1.5 µm x 1.5 µm with 4096 x 4096 pixels. The detector is about 1.2 m away from the focal plane. The magnification $M = (D_1 + D_2)/D_1$ with D_1 is the distance between the focal plane and sample and D_2 the sample to detector distance is due to the beam divergent. The distance between the focal plane and sample can range from 10 mm up to 80 mm, depending on the effective pixel to be used. The effective pixel size can be as low as 25 nm. During the four tomographic scans, the sample is moved in the direction of the beam away from the focal spot between 2mm and 30 mm, to vary the phase shift (Khimchenko, Bikis et al. 2018).

3.4. The ESRF ID19 – microtomography beamline

The ID19 microtomography beamline is mainly devoted to phase-contrast (propagation-based) micro CT. The beamline also pushes the limits in terms of temporal resolution (Rack, Scheel et al. 2014) with an increasing number of ultra-fast imaging experiments for dynamic studies. The ID19 beamline is one of the long beamlines located outside of the synchrotron ring walls (to make large beams and a high spatial coherence).

---

[8] http://www.esrf.eu/files/live/sites/www/files/com%20photos/Users-Science/Beamlines/ID16A_PIERREJAYET.jpg downloaded 08.03.2019

3.4.1. ID19 source

The beamline has as a primary insertion device a W150 wiggler and two U32 undulators. The electron beam source size (expressed as FWHM) is horizontally 135 µm wide and 25 µm vertically high. The beamline's energy range is between 7 and 100 keV, but the best energy range for the beamline is between 12 keV and 60 keV. The second U32 undulator can be replaced by a U17.6 undulator (Weitkamp, Tafforeau et al. 2010).

3.4.2. Beamline optics

The attenuators are located in the first optical hutch between 26 m and 35 m from the source. At 140 m, there is a double crystal monochromator (DCM) water-cooled with two silicon-111 crystals, and at 143 m, there is a Bragg geometry Multilayer monochromator (ML) installed. The DCM accepts energy up to 60 keV, whereas the ML can go up to 100 keV.

The beam size with the DCM is about 45 mm in width, and for 20keV and below 15 mm in height, for 50 keV, the beam height is only 6 mm. The flux density at 20 keV is about 10^{11} photons per second per mm^2; this drops down at 50 keV to about 10^{10} photons per second per mm^2 (Weitkamp, Tafforeau et al. 2010).

3.4.3. Imaging techniques

The beamline is dedicated to propagation-based X-ray micro CT imaging, but it has setups for diffraction-based imaging and laminography. For the propagation-based imaging, two end stations are permanently installed, one for "high-resolution" and lightweight samples and one for "medium-resolution" for heavy samples. The CCD used is the FReLoN detector developed by the ESRF (Labiche, Segura-Puchades et al. 1996, Labiche, Mathon et al. 2007) with a physical pixel size of 14 µm. Different detector optics offer a range of effective pixel sizes between 0.18 µm and 30 µm (Weitkamp, Tafforeau et al. 2010). A full tomography scan can be as fast as 1s for 1.1 µm effective pixel size, which allows time-resolved tomography studies (Boller, Tafforeau et al. 2017). A unique sample stage, the so-called 'tomopress' is available, a horizontal sample holder and rotation stage, combined with a physical press to compress the sample. This tomopress is used in the dynamic cartilage study, which I present in chapter five.

3.5. The SLS - TOMCAT beamline

The name of the beamline, TOMCAT, stands for TOmographic Microscopy Coherent rAdiology experimenTs. It is a laboratory entirely dedicated to tomographic analysis at micron- and sub-micron scales at the Swiss synchrotron facility SLS.

3.5.1. The TOMCAT source

The beamline source is a bending magnet with a magnetic field of 2.9 T and critical energy of 11.1 keV. The photon source size is 53 µm x 16 µm (width x height). With a double crystal multilayer monochromator, the beamline can work with monochromatic radiation in the energy range of 8 – 45 keV (Stampanoni, Groso et al. 2007).

The TOMCAT end station provides a translation of the sample in three directions with a resolution of less than 1 µm. It is a stable setup with reproducibility of about 0.1 µm in the x-direction (perpendicular to the beam).

The rotation stage is an air-bearing-based system from Aerotech, its maximum rotational speed is 3600 deg/s (10 Hz), and it has an error of 1 µm per 100 mm (Stampanoni 2019). The sample holder system is very flexible; it is a plate with balls attached to it, where the magnetic sample holder (Figure 3.8 B) can be easily attached and removed. A robot can automatically change this sample holder. On top of this sample holder, pins (Huber pin Figure 3.8 C) and an area holder (Figure 3.8 D) with a diameter of 3.15 mm can be attached.

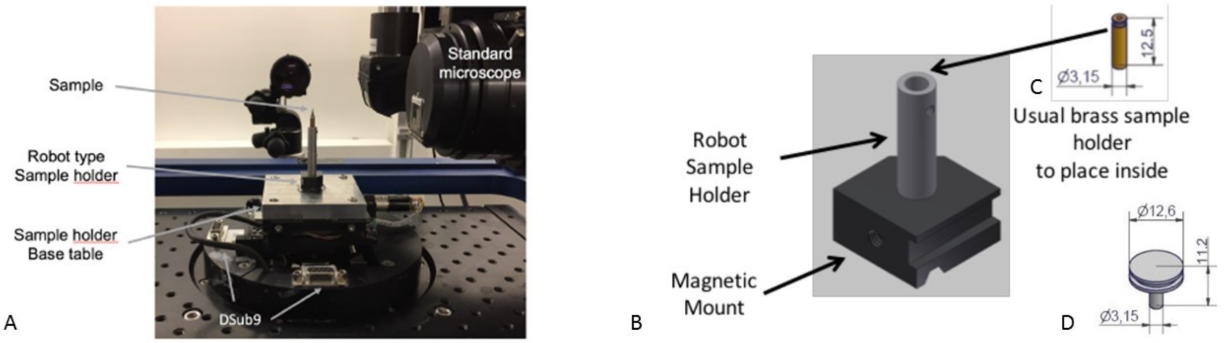

Figure 3.8 Sample holder setup at the TOMCAT Beamline, A) sample holder base plate with sample holder and sample in front of the revolving microscope B) Magnet sample holder C) Huber pin for small sample attachment D) area holder for large sample attachment.

3.5.2. Detection systems

The TOMCAT beamline uses a PCO Edge 5.5 with an LSO:Tb scintillator for high-resolution phase-contrast imaging. Coupled to this detector, a revolving microscope with a magnification of 1.25x, 2x, 4x, 10x, 20x and 40x provides effective pixel sizes of 5.2 µm x 5.2 µm (1.25X magnification) up to 160 nm x 160 nm (40x). For this Thesis work, the 20x and the 40x magnification were used. The 20x magnification has a UPLAPO20x objective, which has a numerical aperture of 0.7, the field of view is 0.8 mm x 0.7 mm, and the effective pixel size is 0.33 µm x 0.33 µm. The magnification mode 40x has a UPLAPO40x objective, which has a numerical aperture of 0.9. The view is 0.4 mm x 0.3 mm, and the pixel size is 160 nm x 160 nm (Marone, Mokso et al. 2011).

3.6. Conventional laboratory X-ray tubes

Conventional X-ray tubes are around for centuries; there is some innovation since Wilhelm Conrad Röntgen built the first X-ray tube in 1896 (Röntgen 1896). The core principle has not changed: an electron beam hits a metal anode from which X-ray photons are emitted, principally, by the photoelectric effect inside atoms and the bremsstrahlung (Coolidge 1912). The resulting spectrum is given by the overlap of the continuous spectrum of the bremsstrahlung radiation and the emitted characteristics lines (characteristic X-rays) of the anode material (an example is reported in Figure 3.9).

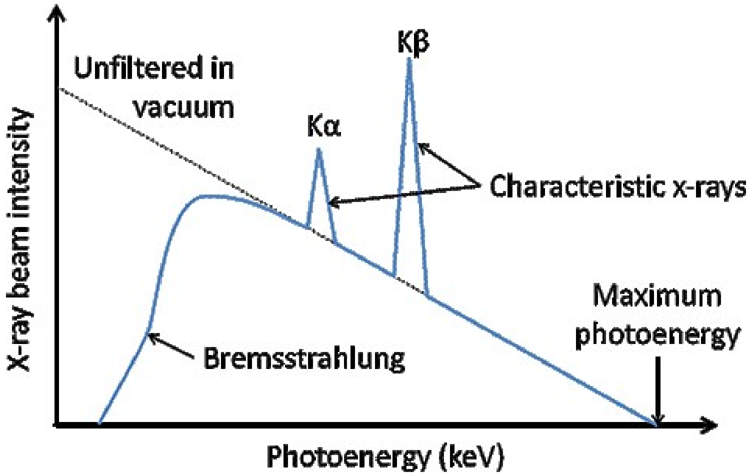

Figure 3.9 Graph of an X-ray tube spectrum, with two peaks indicating the K-edges of the anode material and the continuous bremsstrahlung component. The maximum photon energy and output depend on the voltage applied in the tube[9] *and the tube current.*

The highest brilliance an X-ray tube can get is about 10^{10} photons per mm² s 0.1% bandwidth, whereas the brilliance of synchrotron radiation can as high as 10^{18} photons per mm² s 0.1% bandwidth (see Figure 3.9).

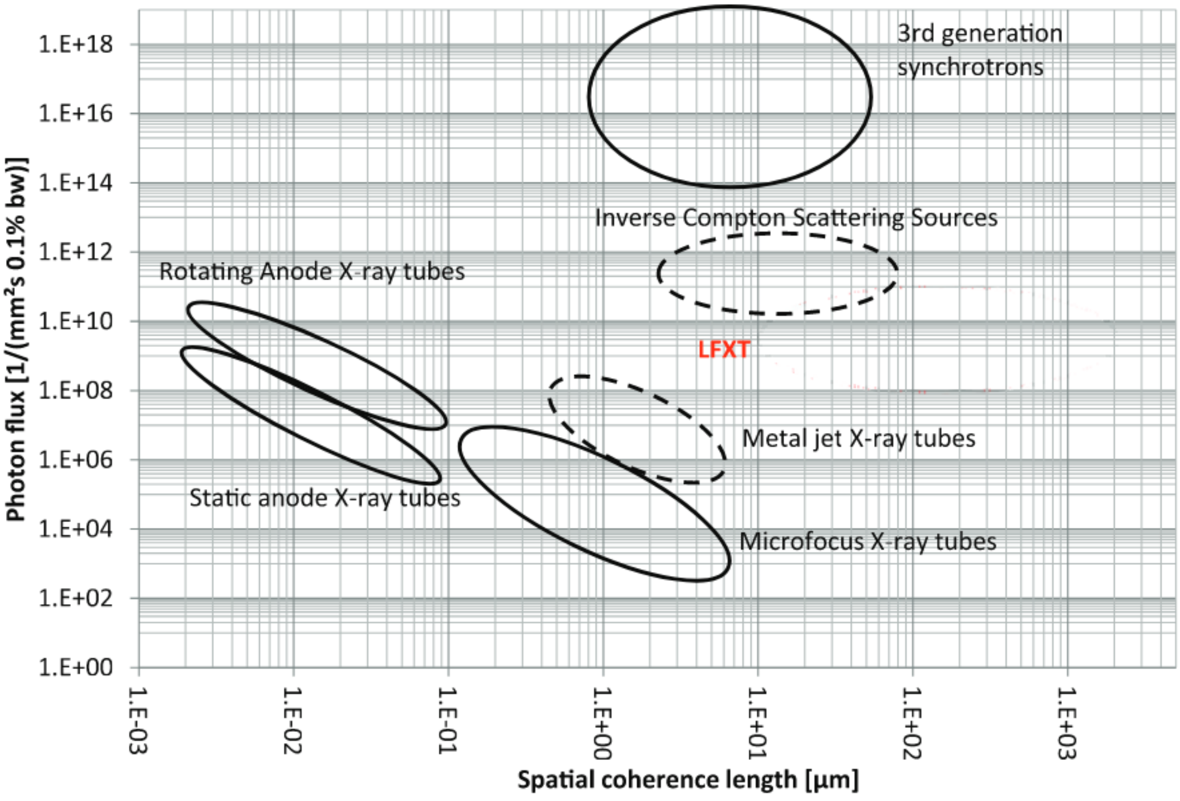

Figure 3.10 Performance of various X-ray tubes in comparison with synchrotron radiation (Bartzsch and Oelfke 2017).

---

[9] https://www.radiologycafe.com/radiology-trainees/frcr-physics-notes/production-of-x-rays Download: 3.1.19

In this Thesis, three different types of X-ray tubes have been used: one rotating anode and two liquid metal jet sources.

3.6.1. Rotating microfocus tube

The rotating anode X-ray tube used for some of the experiments of this Thesis work is from the company XRayWorx[10]. This source is located in Würzburg (Germany), and it is operated by the group NanoCT systems of the Fraunhofer Institute for integrated circuits. It is a 190 KV source, with a maximum current of 1 mA. The target material is Beryllium and Tungsten. The detector in this setup is the PerkinElmer Dexela 1512 NDT CMOS detector with a pixel size of 74.8 x 74.8 μm^2 and a matrix of 1944 x 1536 pixels, with a resulting field of view of 154.4 mm x 114.9 mm and with a Csl scintillator.

3.6.2. Liquid metal jet microfocus X-ray tubes

The liquid metal jet microfocus tube developed by Excillium[11] is located at the Georg-August University of Göppingen/ Germany in the Institute for X-ray physics. The group of Prof. Tim Salditt operates it. It has a liquid metal alloy, which gets pumped through the target area. This means that the heat generated in the target area gets transported away with the alloy. Therefore, a higher electron current can be shot on the target area than standard rotating anode systems—the possibility of using high electron current results in higher X-ray flux. The tube used in this Thesis for micro-CT experiments is called metal jet D2+ and has an alloy of 95 % gallium and 21% Indium. The tube voltage ranges from 21-70 kV, and it has a maximum current of 4.3 mA. The focal spot size is about 5 µm; it does not move its position more than 1 µm. The minimum source to sample distance is 18 mm [12].

3.6.3. 'NanoTube' source

Excillium develops the Nano Source within the project NanoXCT, and it is commercially available under the name "NanoTube". This source is also placed in Würzburg at the ILS Fraunhofer Institute, and the NanoCT System group operates it. To achieve good heat dissipation, the tungsten transmission target is set on the top of a 100 µm thick diamond window. The source size is about a few hundred nanometers. The peak energy of this source is around 60kV. The detector used for this system is the hybrid photon counting "SANTIS" from DECTRIS. The detector has 2048 x 514 pixels with an edge of 75 µm. With this system, the innermost 150 nm lines of a Siemens-star could be resolved (Fella, Dittmann et al. 2018).

---

[10] https://x-ray-worx.com/ Viewed: 25.5.2019

[11] https://www.excillum.com/ Viewed: 25.6.2019

[12] https://www.excillum.com/products/metaljet-sources/metaljet-d2-70-kv/ Viewed: 3.1.2019

Bibliography

Andersson, Å., M. Böge, A. Lüdeke, V. Schlott and A. Streun (2008). "Determination of a small vertical electron beam profile and emittance at the Swiss Light Source." Nuclear Instruments and Methods in Physics Research Section A: Accelerators, Spectrometers, Detectors and Associated Equipment **591**(3): 437-446.

Balerna, A. and S. Mobilio (2015). Introduction to synchrotron radiation. Synchrotron radiation, Springer**:** 3-28.

Bartzsch, S. and U. Oelfke (2017). "Line focus x-ray tubes—a new concept to produce high brilliance x-rays." Physics in Medicine & Biology **62**(22): 8600.

Baruchel, J., J.-L. Hodeau, M. S. Lehmann, J.-R. Regnard and C. Schlenker (1993). Neutron and synchrotron radiation for condensed matter studies, Springer.

Böge, M. (2002). First operation of the swiss light source. EPAC.

Boller, E., P. Tafforeau, A. Rack, V. Fernandez, L. Helfen, M. Rénier, J. Valade, H. Vitoux, J. Villanova and P. Cloetens (2017). "Synchrotron-tomography with micro, nano and high temporal resolution for industrial and academic use." Proceedings ICTMS.

Cesar da Silva, J., A. Pacureanu, Y. Yang, S. Bohic, C. Morawe, R. Barrett and P. Cloetens (2017). "Efficient concentration of high-energy x-rays for diffraction-limited imaging resolution." Optica **4**(5).

Coolidge, W. (1912). "Metallic tungsten and some of its applications." Proceedings of the American Institute of Electrical Engineers **31**(6): 865-874.

Dimper, R., H. Reichert, P. Raimondi, L. S. Ortiz, F. Sette and J. Susini (2015). "ESRF upgrade programme phase II (2015-2022), Technical design study." The orange book, ESRF.

Dr. Cecilia Blasetti, S. D., Emiliano Coghetto (2018). "way for light." Retrieved 21.12., 2018, from Emiliano Coghetto.

Elder, F., A. Gurewitsch, R. Langmuir and H. Pollock (1947). "Radiation from electrons in a synchrotron." Physical Review **71**(11): 829.

Fella, C., J. Dittmann, D. Muller, T. Donath, D. Murer, T. Tuohimaa, A. Sofiienko, S. Zabler and R. Hanke (2018). "Implementation of a Computed Tomography System based on a laboratory-based nanofocus X-ray source." Microscopy and Microanalysis **24**(S2): 236-237.

Hubert, M., A. Pacureanu, C. Guilloud, Y. Yang, J. C. da Silva, J. Laurencin, F. Lefebvre-Joud and P. Cloetens (2018). "Efficient correction of wavefront inhomogeneities in X-ray holographic nanotomography by random sample displacement." Applied Physics Letters **112**(20): 203704.

Khimchenko, A., C. Bikis, A. Pacureanu, S. E. Hieber, P. Thalmann, H. Deyhle, G. Schweighauser, J. Hench, S. Frank and M. Müller-Gerbl (2018). "Hard X-Ray Nanoholotomography: Large-Scale, Label-Free, 3D Neuroimaging beyond Optical Limit." Advanced Science **5**(6): 1700694.

Kunz, C. (2001). "Synchrotron radiation: third generation sources." Journal of Physics: Condensed Matter **13**(34): 7499.

Labiche, J.-C., O. Mathon, S. Pascarelli, M. A. Newton, G. G. Ferre, C. Curfs, G. Vaughan, A. Homs and D. F. Carreiras (2007). "Invited article: The fast readout low noise camera as a versatile x-ray detector for time resolved dispersive extended x-ray absorption fine structure and diffraction studies of dynamic problems in materials science, chemistry, and catalysis." Review of scientific instruments **78**(9): 091301.

Labiche, J. a.-C., J. Segura-Puchades, D. Van Brussel and J. Moy (1996). "FRELON Camera: fast readout low noise." ESRF newsletter **25**: 41-43.

LAISSUE, J., J. LE BASZ, G. LE DUCI, N. LYUBIMOVA, C. NEMOZ and M. RENIERI (2000). "RESEARCH AT THE EUROPEAN SYN CHROTRON RADIATION FACILITY NIEDICAL BEAMLINE." Cellular and Molecular Biology **46**(6): 1053-1063.

Ludeke, A. and M. Munoz (2002). Top-up operation experience at the Swiss Light Source. EPAC.

Marone, F., R. Mokso, P. Modregger, J. Fife, B. Pinzer, T. Thüring, K. Mader, G. Mikuljan, A. Isenegger and M. Stampanoni (2011). Present and Future X-ray Tomographic Microscopy at TOMCAT. AIP Conference Proceedings, AIP.

McNeil, B. (2009). "Free electron lasers: First light from hard X-ray laser." Nature Photonics **3**(7): 375.

Mittone, A. (2015). Development of X-ray phase-contrast imaging techniques for medical diagnostics, lmu.

Mittone, A., I. Manakov, L. Broche, C. Jarnias, P. Coan and A. Bravin (2017). "Characterization of a sCMOS-based high-resolution imaging system." Journal of synchrotron radiation **24**(6): 1226-1236.

Rack, A., M. Scheel, L. Hardy, C. Curfs, A. Bonnin and H. Reichert (2014). "Exploiting coherence for real-time studies by single-bunch imaging." Journal of synchrotron radiation **21**(4): 815-818.

Robinson, A. (2009). "X-Ray Data Booklet Section 2.2 history of synchrotron radiation." Center for X-ray Optics and Advanced Light Source, Berkeley.

Röntgen, W. C. (1896). " Ueber eine neue Art von Strahlen (Vorläufige Mittheilung)." Stahel'sche K. Hof- und Universitätsbuch- und Kunsthandlung **1**: 1.

Stampanoni, D. (2019). "Enstations." Beamline Information Retrieved 07.03.2019, 2019, from https://www.psi.ch/sls/tomcat/endstations.

Stampanoni, M., A. Groso, A. Isenegger, G. Mikuljan, Q. Chen, D. Meister, M. Lange, R. Betemps, S. Henein and R. Abela (2007). TOMCAT: A beamline for TO mographic M icroscopy and C oherent r A diology experimen T s. AIP Conference Proceedings, AIP.

Suortti, P., S. Fiedler, A. Bravin, T. Brochard, M. Mattenet, M. Renier, P. Spanne, W. Thomlinson, A. Charvet and H. Elleaume (2000). "Fixed-exit monochromator for computed tomography with synchrotron radiation at energies 18–90 keV." Journal of synchrotron radiation **7**(5): 340-347.

Weitkamp, T., P. Tafforeau, E. Boller, P. Cloetens, J. P. Valade, P. Bernard, F. Peyrin, W. Ludwig, L. Helfen and J. Baruchel (2010). Status and evolution of the ESRF beamline ID19. AIP Conference Proceedings, AIP.

4. Multiscale phase-contrast imaging of cartilage

X-ray phase-contrast imaging allows visualizing soft materials like cartilage with multiple spatial resolutions. The multiscale approach is essential to study the hierarchical organization of many biological tissues and understand the macro-changes induced by pathology in an organ by analyzing small sub-structures within sub-regions. There is always a tradeoff between pixel size and the size of the field of view. Large pixel size leads to a large field-of-view in a detector with a fixed number of pixels. Consequently, when you increase the spatial resolution (i.e., smaller pixel size), the field of view gets smaller, and one can investigate only sub-volumes. In this study, a series of experiments were conducted using different spatial resolutions to access one side the overall cell distribution within the cartilage tissue and, on the other side, the structure of the single cell.

The objective of this work was to visualize the cartilage and its changes due to osteoarthritis. Many experiments on different beamlines with different techniques and optical systems were carried out and presented here. Experiments were performed at different synchrotron beamlines: we used pixels sizes of 6 µm and 0.7 µm at the biomedical beamline ID17 at the ESRF (Mittone, Fardin et al. 2020), of 0.32 µm and 0.16 µm at the TOMCAT beamline at PSI and finally, an effective pixel size of 100 nm at ID16a at the ESRF.

In the first part of this chapter, the different sample preparations required for these measurements are described and the used experimental parameters. Then the results of the different experiments are shown and discussed. In the last section, the images acquired at the Synchrotrons are compared with images that were acquired with table-top laboratory X-ray sources.

This chapter's results are condensed in the paper "Multiscale X-ray Phase-contrast Imaging of human Cartilage for investigating Osteoarthritis Formation," which is currently in the review stage (Horng, Stroebel et al. 2020).

4.1. Description and preparation of the samples

The samples used for the experiments explained in the following were extracted from human patellae with different degrees of cartilage degeneration. For the different experiments and experimental stations, a specific preparation of the samples was needed.

4.1.1. Description of the samples

The cylindrical osteochondral samples were drilled from three human knee joints (from the femur or patella of a 73-year-old man and a 67-year-old woman). All specimens were harvested within 24 hours of death at the Forensic Medicine department of the Ludwig Maximilians University (Munich, Germany) after obtaining informed consent from the donor's next-of-kin. Samples were preserved in a 10% formalin-saline solution, which reportedly does not influence PCI results(Mollenhauer, Aurich et al. 2002, Li, Zhong et al. 2009).

The cartilage tissues were classified as healthy and slight to medium degenerated samples. The assignment was based on macroscopic visual evaluation of the cartilage surface and thickness, respectively, an experienced forensic doctor and a musculoskeletal-expert radiologist. A smooth surface was considered an indication of healthy cartilage, slight fibrillations and roughened surface as signs of a medium degenerated cartilage.

The specimens for the experiments at ID17 were from the 67-year-old (patella) women. For the ID16 experiment and the TOMCAT experiment samples, a 73-year-old man from the patella and femur was used.

Figure 4.1 An osteochondral plug harvest from a human patella. The plug has a diameter of 7 mm; the white part is cartilage, and the brown part the bone. The samples with dimensions were used in the experiment at ID17.

4.1.2. Sample preparation

Liquid environment

For the TOMCAT (SLS) experiments and Biomedical beamline ID17 (ESRF), the sample stage is usually under normal room pressure. Therefore, samples needed to be put in a sealed plastic container filled with formalin to keep the samples in a wet environment. The container was an Eppendorf Conical Tube (5 ml). The Eppendorf tube was positioned upside down with the bone fixed to the tube's head to prevent movements. All air bubbles were removed by gently shaking the tube.

Vacuum environment

For the experiment in vacuum at ID16a, the samples need to be prepared specially. The samples' size cannot exceed 0.5mm x 0.5mm x 3mm (width x depth x height) because a crane carries samples onto the sample stage. The crane can carry Huber pins, with an opening of 0.5 mm. The space above the Huber-pin was only 3 mm high.

Samples were decalcified in Ethylenediaminetetraacetic acid (EDTA) for about four days. Afterward, they were embedded in paraffin blocks and cut into slices of 0.5 mm thickness using a microtome. The slices were then cut manually into 0.5 mm thick sticks. The sticks were then glued into the Huber pin, as seen in Figure 4.2.

Figure 4.2 Three samples prepared for imaging at ID16a; the samples are in the dimension of 0.5mm x 0.5mm x 3mm (width x depth x height), samples are decalcified and fixed in paraffin.

4.2. Experimental Parameters

We performed experiments with different spatial resolutions at different beamlines.

4.2.1. Imaging experiments at ID17 (ESRF)

- Micrometer spatial resolution and monochromatic X-rays

The experiment was done in the second experimental hutch of ID17; the beam energy was 60 keV. The distance between the source and the sample was 150 m, and the sample to detector distance was 2.32 m. The PCO Edge, with no optics, was used and had an effective pixel size of 6.1 µm vertically and horizontally. The synchrotron storage ring was filled in 16 bunch mode; this means the photons' flux was relatively low compared to the 7/8 filling mode (used in general for micro-CT experiments). Therefore, each projection's integration time was 1.5 s; the number of CT angular projections was 4000 over 180 degrees in this experiment.

- Sub-micrometer spatial resolution experiment and pink beam

The acquisitions were made in the first experimental hutch, where a polychromatic beam is available. Therefore the flux is much higher than with a monochromatic beam, and fast integration times are possible. This also means fast CT acquisitions.

The beam was filtered with one Carbon filter of 1.15 mm thickness, two Aluminum filters of 0.28 mm and 1.24 mm and one 1.06 mm thick copper filter. The peak energy of this polychromatic beam was 44 keV. The propagation distance between samples and the detector was 1.22m. The detector system was the dual-lens system from Optique peter with a magnification factor of 10x (5x) coupled with the PCO Edge detector. The effective pixel size was 0.7 µm (1.4 µm) vertically and horizontally. The field of view was about 1.5 mm x 1.5 mm x 1.5 mm. This only covers a fraction of the cartilage plug, therefore to cover the height of interest in the sample, 2 to 3 scans were needed. For this experiment, 4000 projections over 180 degrees were used, and the integration time was 0.03 s.

4.2.2. Imaging at TOMCAT (SLS)

A monochromatic beam with an energy of 17 keV was used to perform a sub-micron resolution experiment. The effective pixel size of the detector system was 0.325 µm. This was achieved by coupling a PCO Edge 5.5 sCMOS detector with a UPLAPO20x objective. The field of view with this setup was 0.9 mm x 0.9 mm x 0.9 mm. The propagation distance between sample and detector was 103 mm. 2000 projections are acquired on a 180^o turn, with an integration time of 0.1 s per projection.

4.2.3. Imaging at ID16a (ESRF)

A monochromatic beam with an energy of 17 keV was used. In one acquisition, four 180^o CT scans were performed with a different focal plane -sample distances, between 10 mm and 80 mm. For every scan, 1800 projections were acquired. For every projection, the sample was displaced in x and y-direction (perpendicular to the beam) few pixels in a random pattern; this displacement is then corrected for before the CT data reconstruction phase. The procedure is applied to reduce the presence of ring artifacts in the reconstructed images. A step by shoot mode is thus needed, making the acquisition time longer compared to a continuous mode. One scan took in this experiment about 1 h. Therefore 4 h were required for collecting the full 4 scan acquisition for holotomography. The effective pixel size was 100 nm. The field of view for one acquisition was 0.25 mm x 0.25 mm x 0.25 mm. The detector system is a lens coupled to a FReLoN F_E230-84 (4096x4096 pixels, 1.5 um pixel size). Multiple acquisitions were made within each sample's cartilage tissue: one at the top of the sample (close to the cartilage surface), one in the middle and one close to the bone part of the sample.

4.3. Results

4.3.1. Multiscale overview

In Figure 4.3, examples of the CT images of a cartilage sample acquired at three different spatial resolutions are reported: A) pixel size of 6 µm; b) pixel size of 0,7 µm; c) pixel size of 0,1 µm. This collage shows in A) the entire cartilage with the three main layers (superficial, mid and deep layer), in B) a part of the superficial layer is shown and in C) a closer look at a small part of the superficial layer is depicted. Besides, this collage shows what the field-of-view of each experiment is.

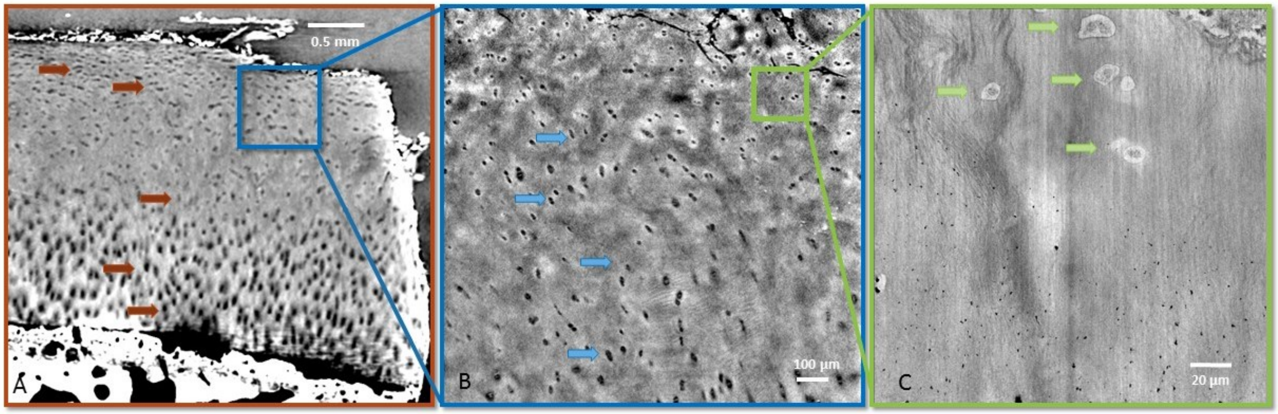

Figure 4.3 Multiscale images of the cartilage tissue acquired with different pixel sizes. Arrow indicating chondrocytes A) 6 µm pixel size and 60 keV X-rays, an overview of the cartilage with its different regions; B) 0.7 µm pixel size and filtered polychromatic X-ray beam, an image of a sub-region in the cartilage, a detailed view of the chondrocyte distribution are given; C) 0.1 µm pixel size, and 17 keV, details of the structure of the cells are visible.

4.3.2. Cartilage structure overview and chondrocyte arrangement

The cartilage tissue composition can be visualized in detail with X-ray PCI-CT as shown in Figure 4.4 that report sagittal views extracted from the micro CT reconstructed data sets of a healthy (A), and an OA degenerated (B) cartilage tissue acquired with a pixel size of 6 µm. These images visualize the complete layer of the articular cartilage and provide an overview of the tissue's general architecture. Cells of different sizes, distributions, and orientations, corresponding to chondrocytes and chondrons (as proved by the related literature and histology), are demarcated. The cartilage matrix is not homogeneous. Results depict an arrangement of those cells that varies throughout the tissue depth in the different samples. Differences between healthy and degenerated cartilage are visible on several levels of detail. The characteristic structure of a healthy cartilage sample with the three layers (superficial, transitional middle, deep layer) with the respective anticipated chondrocyte morphology and arrangement is visible (Figure 4.4 A).

Tissue degradation such as superficial defects, their spread within the tissue, and concomitant underlying changes of the tissue architecture with disturbances of the matrix is directly visualized (Figure 4.4 B) compared to the healthy tissue (Figure 4.4 A).

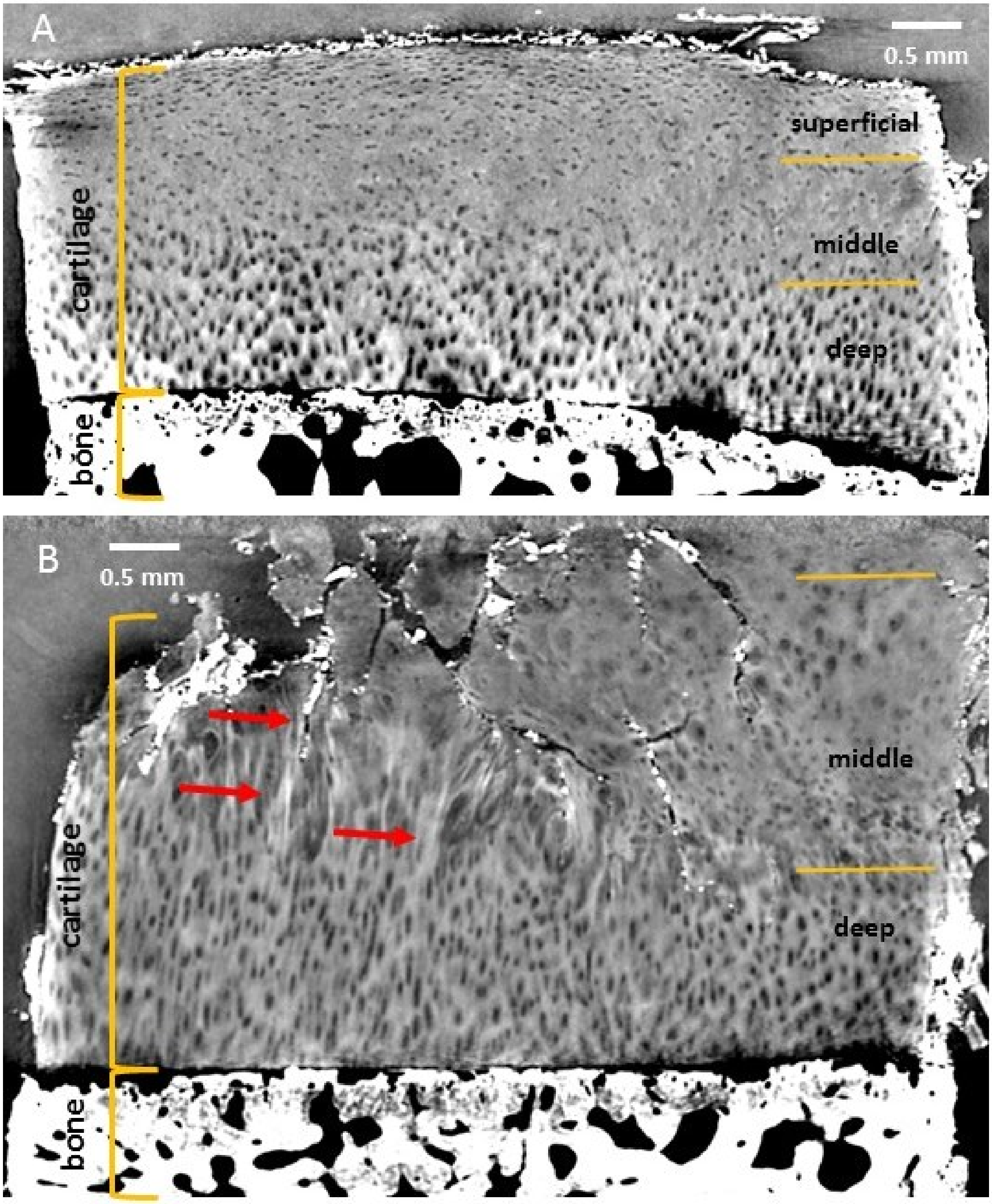

Figure 4.4 X-ray phase-contrast CT images of a healthy (A) and moderately degenerated (B) cartilage sample. Images were acquired using X-rays of 60 keV and a pixel size of 6.1 µm at the ID17 beamline. A: The three cartilage layers are visible and intact (superficial layer, middle layer, deep layer) B: The superficial layer and the middle layer show deep defects and fissures with disturbances of the matrix architecture (red arrows), while the deep layer is still preserved. The chondrocytes in the degenerated sample (B) show changes in their morphology throughout the superficial layer with loss of their flattened shape in the superficial layer as well as enlargement and initial clustering in the middle layer.

4.3.3. Healthy cartilage structure

The sub-micron spatial resolution PCI-CT images from TOMCAT (SLS) beamline (0.325 µm pixel size) enable a more detailed visualization of the chondrocytes and the tissue morphology throughout the cartilage layer (Figure 4.5). The findings of the X-ray PCI images are correlated with histological slice stained with Masson Goldner trichrome staining and imaged with a light microscope (5x and 20x magnification)(Figure 4.5 C, G, H, I). The chondrocytes are demarcated in the cartilage with a visible round core representing the cell nucleus as well as other small cell components, which appear as black dots.

In the superficial layer, the chondrocytes show a flattened shape and are horizontally oriented (parallel to the tissue surface) within the tissue matrix (Figure 4.5 A/D). This layer is thin.

The chondrocytes have a round to oval shape in the middle layer, arranged in pairs, triples or small clusters, which show no special arrangement within the matrix (Figure 4.5 E).

Further, into the cartilage's depth, there is a third, thicker layer with round to oval-shaped chondrocytes that are arranged in long columns with multiple cells oriented perpendicularly concerning the plane of the subchondral bone surface (Figure 4.5 B).

At the cartilage-bone interface, the chondrocytes cluster again partially within the deepest layer of the cartilage, partially within the subchondral bone. The transition zone between cartilage and calcified bone, the so-called tidemark, is well demarcated and shows a wavy interface (Figure 4.5 F).

The subchondral bone architecture is depicted with cell bodies arranged around lacunar structures (Figure 4.5 F).

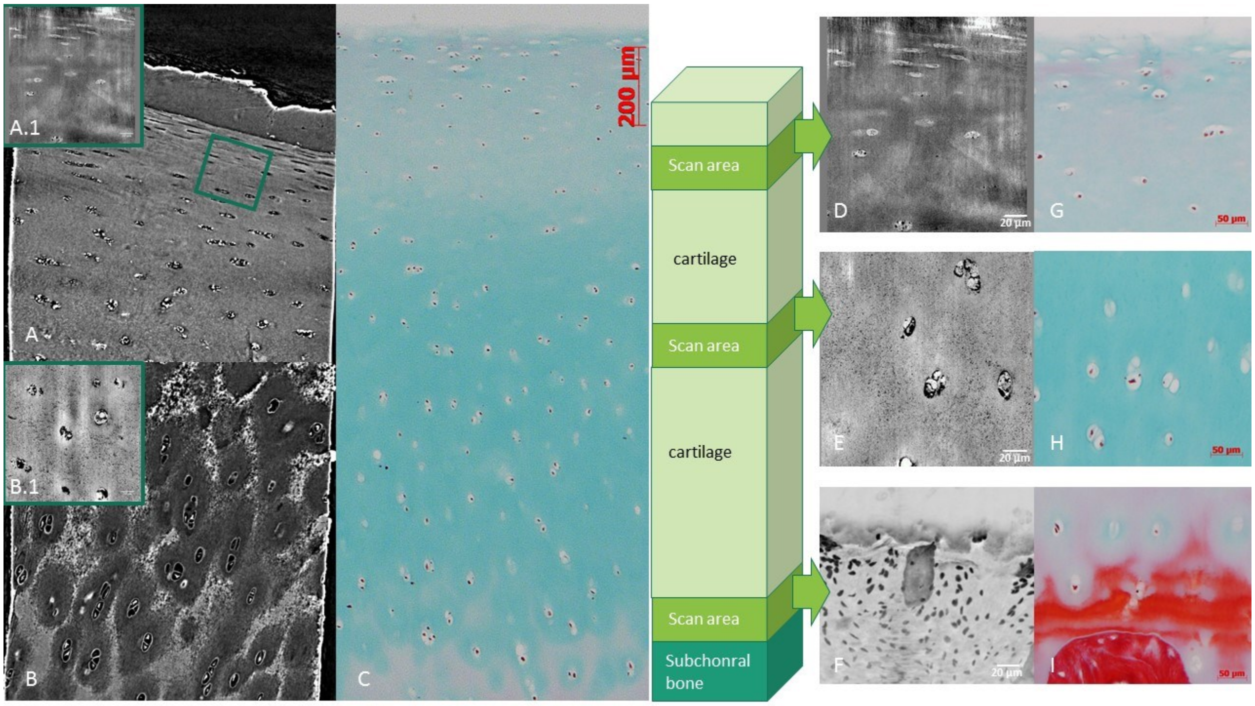

Figure 4.5 X-ray PCI of healthy sample in comparison with histology; A) + B) X-ray phase-contrast images from TOMCAT (SLS) beamline (pixel size 0.325 µm);A.1)+B.1)+ D)+E) nano-holotomography images 100 nm pixel size; F) X-ray tidemark image in Z-projection (ID17, ESRF, 0.7 µm pixel size); C) Histology images (magnification 5x) of the superficial, mid and deep zone (Masson Goldner trichrome staining) G)-I) Histology images (magnification 20x) of the superficial, mid and deep zone (Masson Goldner trichrome staining).

4.3.4. Mildly degenerated cartilage structure

The PCI-CT images of the degenerated samples show fibrillation, tears (Figure 4.6 C/F), cracks and/or delamination of the superficial (Figure 4.7 C) and often the middle layer as direct signs of damage. There were no samples with denuded cartilage as the goal in this study was to evaluate whether PCI can depict early stages of cartilage degradation.

The mildly degenerated cartilage samples showed different degrees of superficials defects and fissuring (Figure 4.6 and Figure 4.7). Additionally, to the surface defects, changes in the chondrocytes' morphology and arrangement are observable by PCI-CT (Figure 4.6 C/F). This can also be seen in the histology image (Figure 4.6 I)

The usually flattened chondrocytes from the superficial layer were rarefied and enlarged. The superficial layer with the horizontally oriented flattened chondrocytes is disrupted and, depending on the degree of degradation, is no longer visible in Figure 4.6. The shape of the chondrocytes in and just below that layer is rounded, and their original orientation changed, showing a more scattered formation (Figure 4.6 and Figure 4.7 C).

The normally rather roundish chondrocytes of the middle layer appear larger and form clusters of differently sized cells instead of columns (Figure 4.6 D/G and Figure 4.7 D). The clustering is also visible on the histology image (Figure 4.6 J). In the image of Figure 4.6 F and Figure 4.7 D, white parts/ lines appear; these are artifacts coming to form the not perfectly round sample edges.

In the deep layer, the chondrocytes still depict columns, but with some slight disarrangement not only in a vertical line but also showing partial clustering (Figure 4.6 E/H and Figure 4.7 E). On the histology image (Figure 4.6 K) the chondrocytes form columns, but the disarrangement and clustering can be depicted as well (Figure 4.7 H).

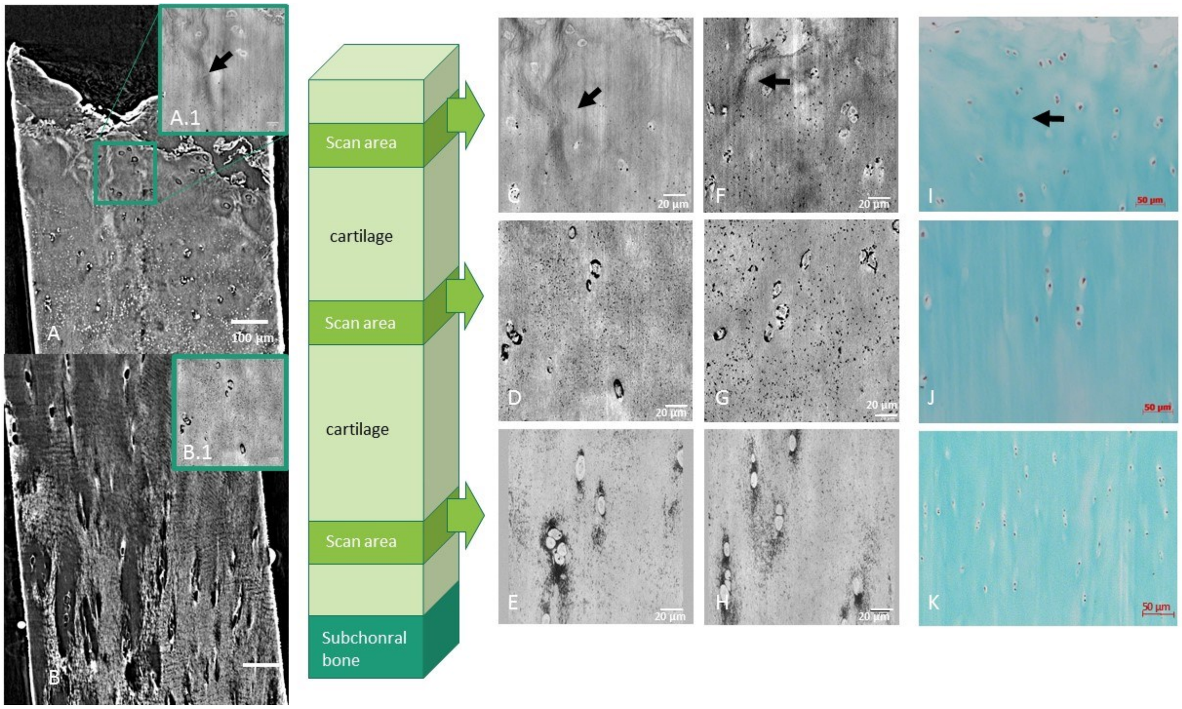

Figure 4.6 X-ray PCI and histology images of a mild degenerated sample from a superficial, mid and deep zone: A) + B) images from TOMCAT beamline 325 nm pixel size; A.1)+B.1)+ C)-H) nano holotomography images from ID16a, 100 nm pixel size; I)-K) histology images (20x magnification) with Masson Goldner trichrome staining. Black arrows are indicating the fiber bundles within the superficial layer.

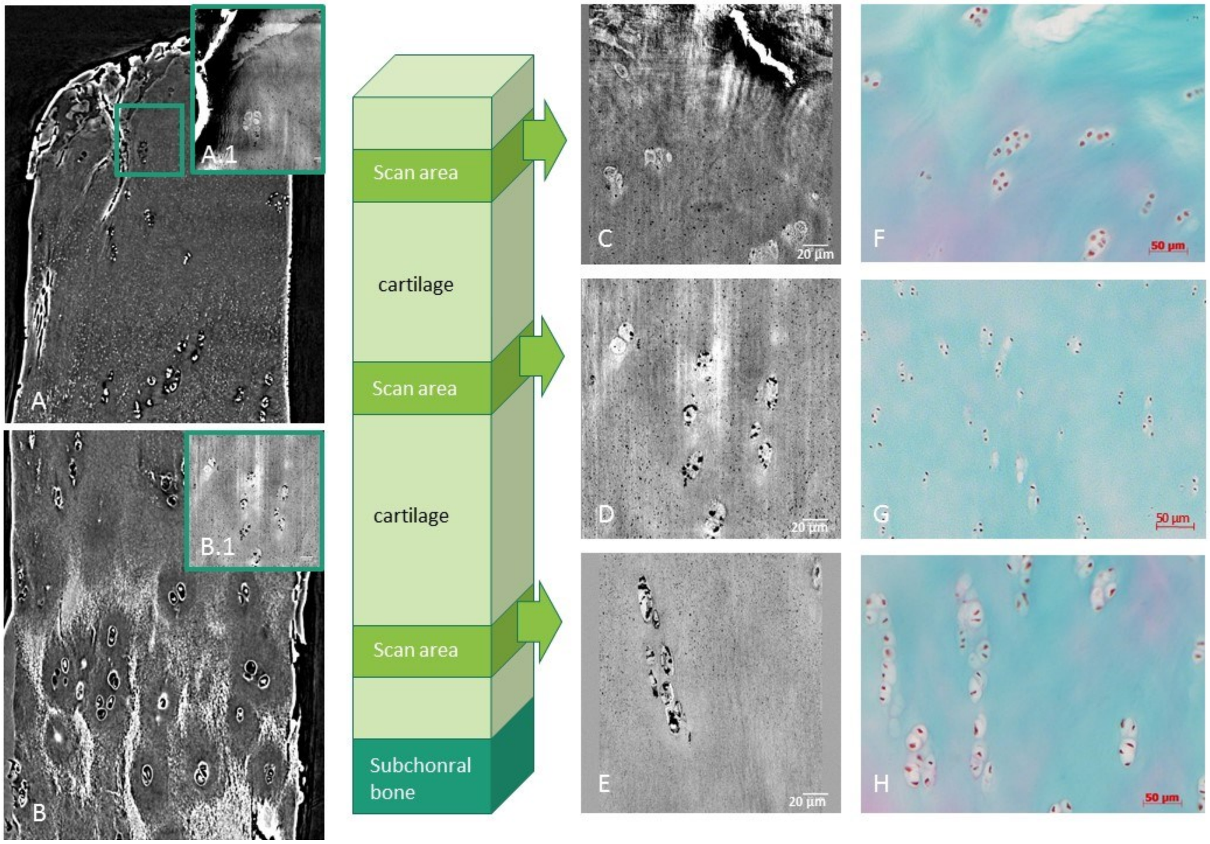

Figure 4.7 X-ray PCI in comparison with histology of a degenerated sample; A)+B) PCI images from TOMCAT beamline at Swiss Light Source (325 nm pixel size); C) – E) nano holotomography images with 100 nm pixel size; F)-H) histology images from the superficial, mid and deep zone (Masson Goldner trichrome staining).

Chondrocyte shape and environment

The cell bodies show structures with varying regional densities but also a halo around the single or clustered cells (Figure 4.6 B, Figure 4.7 B). Several samples show numerous high-density dots in the chondrocyte cells and at their border area, pronounced in the middle and lower cartilage layer (Figure 4.6 D/E and Figure 4.7 D/E). These high-density spots are between 1 and 10 µm wide and stick in the lower part of the cartilage at the chondrocytes (Figure 4.6 E/I and Figure 4.7 D/E). In one singular sample fiber-like linear dense structures are visualized in between the chondrocytes in the superficial layer (Figure 4.6 A.1/C/F – black arrow). Fractures are seen in the superficial layer of the degenerated samples. (Figure 4.7 A/A.1/C/F) This is a clear sign of advanced degeneration.

4.3.5. Visualization of the cartilage architecture

A three-dimensional dataset is difficult to visualize in 2D. There is the possibility of rendering, but this is computationally heavy and not easy. The chondrons are distributed scarcely in the tissue. Therefore advanced segmentation and rendering are need, to analyze the cell distribution. There is a better way to visualize the cell distribution by superimposing multiple slices. This superimposition is used to get a better depiction of the cell distribution. The images from ID17, with 0.7 µm pixel size, provide an improved depiction, especially of the arcade-like chondrocyte distribution in the transitional layer (Figure 4.8 B/F) below the horizontal superficial layer (Figure 4.8 A) and the column-like distribution of the chondrocytes in the deep layer in a healthy sample (Figure 4.8 C/G).

This superimposing method also reveals a detailed depiction of the tidemark showing that it is not just a smooth-linear border between cartilage and subchondral bone, but a wavy interdigitating surface in the horizontal plane (Figure 4.8 E), which plays a role an improving force distribution and biomechanical stability.

In the degenerated samples, the pattern of disruption of the chondrocyte arrangement can be visualized (Figure 4.9 A-C/F) and therefore can provide a suitable tool for further and improved analysis of the individual steps in cartilage matrix breakdown during degradation, which might then aid in understanding changes in biomechanical properties in this phase.

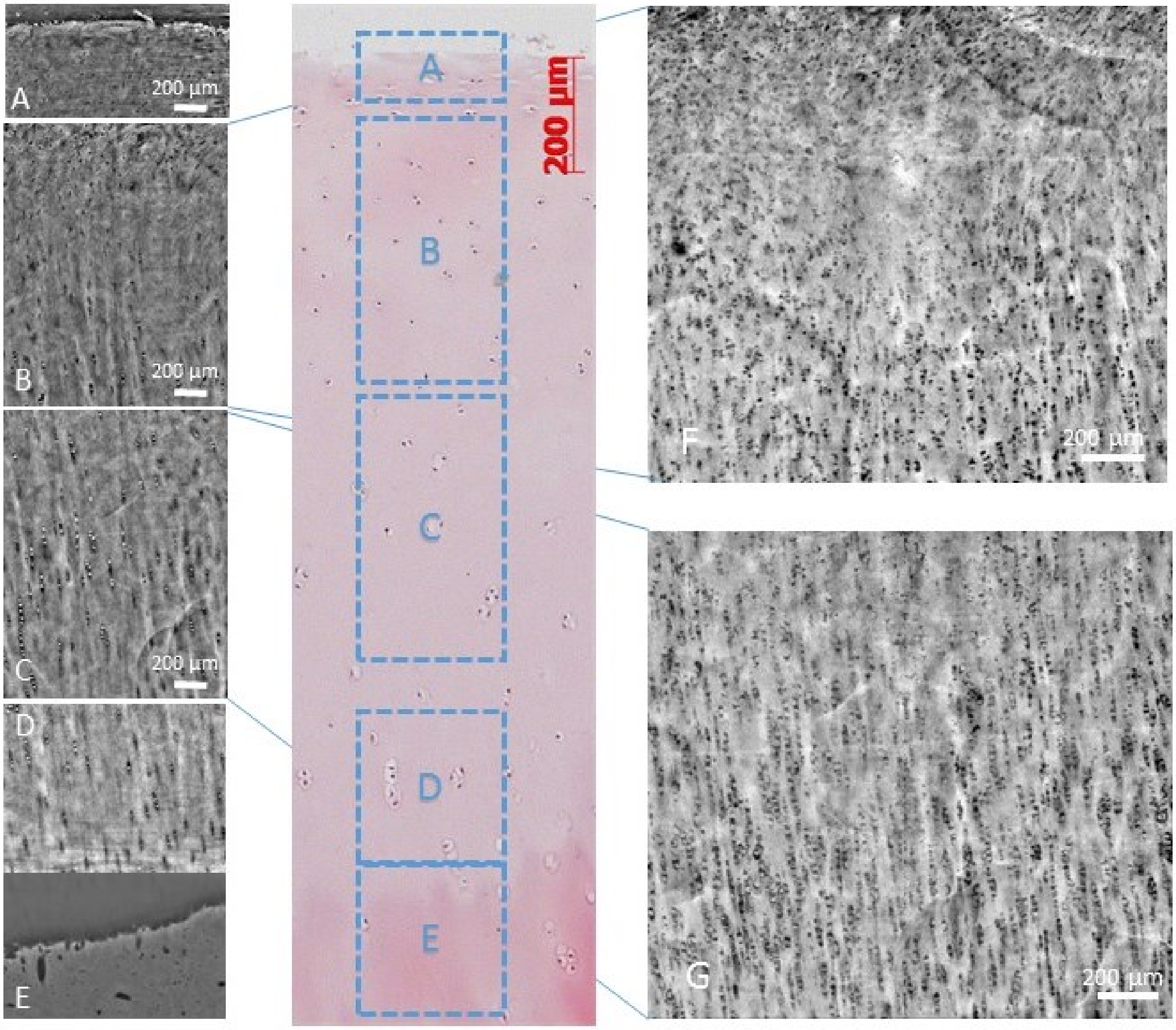

Figure 4.8 X-ray PCI sagittal images of healthy samples; the images come from ID17 with an effective pixel size of 0.7 µm; A)-D) four sagittal image of different cartilage zones. E) adjusted gray level for tidemark visualization F)+G) Z-projections from the mid zone, min values combined of 200 Slices H)-I) small healthy sample

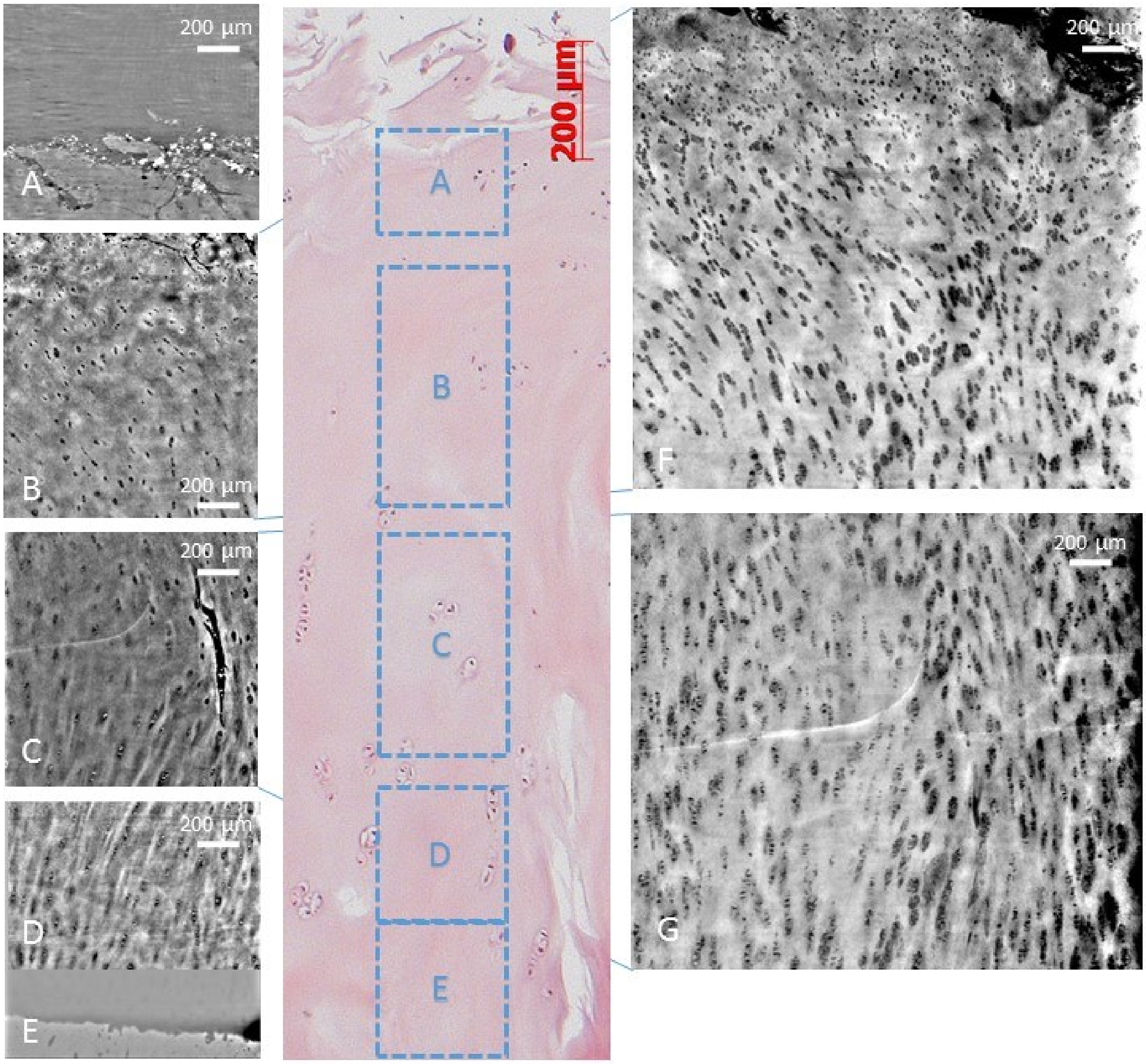

Figure 4.9 X-ray PCI sagittal images from ID17 high –resolution setup (effective pixel size 0.7 µm); A)-E) different images from different areas of sample F) Z-Projection of the transition between superficial zone and mid zone

4.3.6. 3D analysis of the chondrocyte distribution

The high detail and quality of the CT data sets acquired in these imaging experiments allow both visualizing and quantitatively analyzing in 3D and at different scales the cells' morphology in terms of shape, structure, form, size, and distribution. These tasks rely on the possibility of accurately performing the segmentation of the features of interest (chondrocytes or chondrons within the cartilage matrix).

In Figure 4.10, the results of the segmentation of cartilage cells from the PCI-CT datasets of a healthy (A) and OA degenerated (B) sample, respectively, are presented. The WEKA machine learning segmentation was done on nano-holotomography datasets, with an effective pixel size of 100 nm. Both datasets were acquired at the top of the sample; the superficial layer was still present for the healthy sample. This can be seen on the horizontally oriented cells. For the OA degenerated sample (Figure 4.10 B), the superficial layer is no longer present, and the cells are oriented vertically.

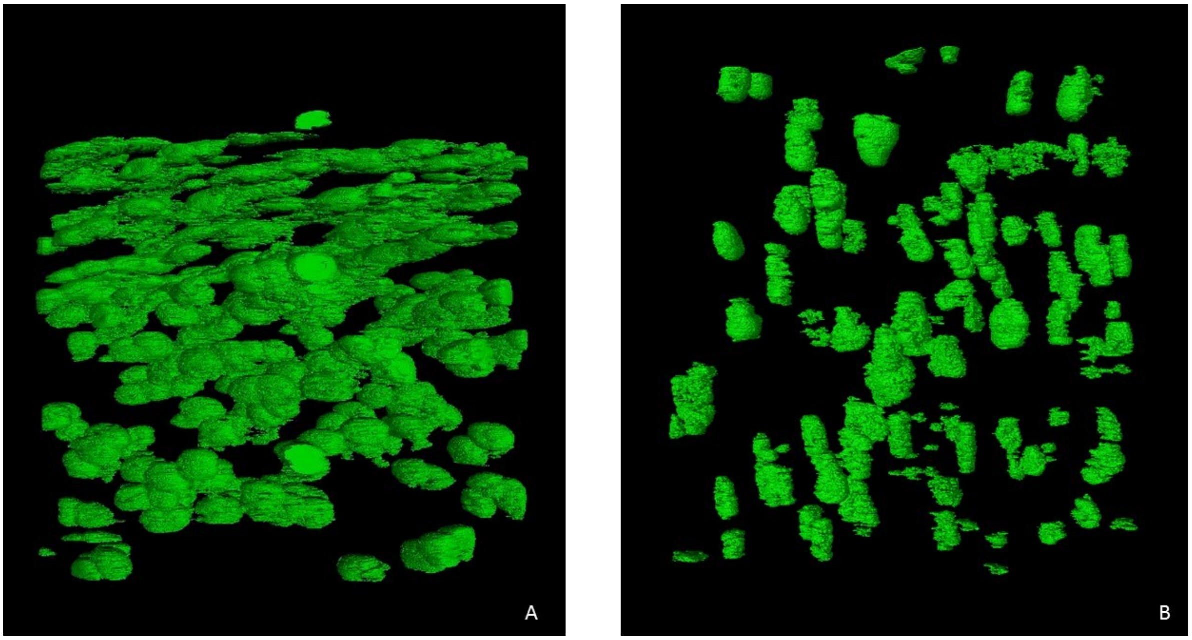

Figure 4.10 3D rendering (VGStudio max) of segmented chondrocytes/chondrons in a healthy cartilage sample (A) and a degenerated sample (B) in the superficial and underlying middle layer. The segmentation was performed with the advanced machine learning algorithm WEKA. Nano-holotomography in comparison with TEM

Using nano-holotomography CT, the structure of a single cell and details within the cell body can be depicted; the nucleus of the chondrocytes and even a shadow of the cell organelles are visible (Figure 4.11). The chondrocyte with the surrounding territorial matrix is observable (Figure 4.11 A yellow). In one mildly OA degenerated sample, some bundle-like structures are also depicted within the tissue, as shown in Figure 4.11.

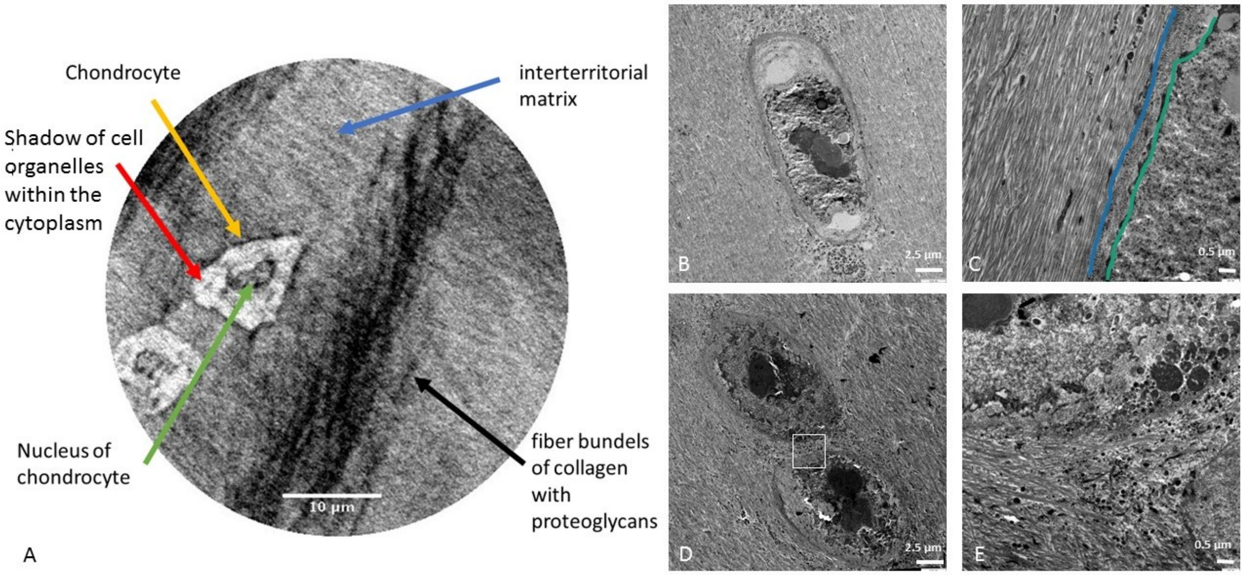

Figure 4.11 A) Excerpt of a mildly degenerated cartilage sample in a nano-holotomography image with 0.1 µm pixel size, showing two chondrocytes with their nucleus, shadows of cell organelles within their cytoplasm and unmasked fiber bundles, in between interterritorial matrix (scale 10 µm); B)-E) Transmission electron microscope images of cartilage; B)+D) chondron with 3000x magnification (scale 2.5 µm); C) Territorial matrix (left of blue line), immediately pericellular matrix (between lines), chondrocyte (right of green line), 12000 x magnification (scale 0.5 µm); E) territorial matrix close up from image D) (scale 0.5 µm).

4.4. Discussion

The potential of PCI: anatomy and condition of hyaline cartilage

PCI is the first X-ray based imaging modality which can directly visualize hyaline cartilage tissue and its reported known organized layered composition consisting of a superficial, transitional middle, deep and calcified layer(Pearle, Warren et al. 2005) and provide a clear depiction of shape and localization of the chondrocyte subpopulations. Around the chondrocytes, differences in electron density can be visualized that might correspond to the differing composition of the extracellular matrix, which is known to be produced and altered by the chondrocytes (Archer and Francis-West 2003).

The extracellular matrix has been described to express biochemical as well as morphological variations throughout the depth of the cartilage, with chondrocytes also differing regionally in shape and expression of biochemical secretion. Previous studies have reported that the chondrocytes of the different layers produce different kind of collagen, proteoglycans and other biochemicals and also show differing morphology from being flat in the superficial layer (Schumacher, Block et al. 1994), rounded in the mid zone (Lorenzo, Bayliss et al. 1998). Larger rounded in the deep zone (Schmid and Linsenmayer 1985), suggesting that the differing morphology might come with a different function for matrix homeostasis.

Besides histology and transmission electron microscopy (TEM), this is the first time a principally non-invasive imaging technique reaches this kind of necessary resolution to resolve this morphological variation of the chondrocytes. However, the variation of the extracellular matrix itself can only be assumed due to electron density variations. Collagen fiber-like structures were only depictable in one sample so that it remains unclear under what circumstances collagen might be visible. However, as this occurred in one mildly degenerated sample, a possible explanation might be the demasking of collagen bundles due to the loss of proteoglycans.

With the ability to depict the morphology of the chondrocyte subpopulations within cartilage tissue as well as their changes in degenerated samples, for the first time, a suitable technique has emerged for classifying cellular changes in different stages of cartilage aging and degeneration. Knowing that the chondrocyte subpopulations have different properties regarding the matrix homeostasis as well as different colony-forming capabilities, studying morphological changes and possible chondrocyte migration might aid in understanding matrix composition alterations and biomechanical properties throughout the development of cartilage degradation.

Being able to depict the exact condition of the cartilage matrix may aid in the analysis of OA. The ultimate aim is to replace cartilage defect with functional tissue in order to defeat OA.

Sample degradation

No changes within the samples were noticed while applying high radiation doses for the 4 hour-holotomography acquisitions thanks to a sample environment under vacuum conditions. The TOMCAT Beamline and the ID17 beamline, with their high-spatial-resolution setups, can provide CT scan times of about 10 min. Degradation of the sample is possible because the sample environment is under normal pressure. The TOMCAT beamline can reach the detector system (pixel size up to 160 nm possible) at a higher resolution than the ID17 (0.7 µm effective pixel size). In terms of resolution, the ID16a outperforms the two other beamlines (100 nm effective pixel size). Still, the scan time with 4 hours per scan is much longer, and the change of sample is much slower because the sample environment is under vacuum. However, the image quality at ID16a is outstanding in comparison with the other beamlines.

Limitations

X-ray PCI ex-vivo studies, e.g., cartilage studies, can be done with state-of-the-art X-ray tubes or dedicated synchrotron facilities. Synchrotron radiation facilities provide the highest image quality and the shortest acquisition time, because of their brilliance, compared to table-top X-ray tubes. However, synchrotron radiation facilities are not easily accessible. Technically, PCI is a non-invasive imaging technique. Even though larger objects are penetrable and depictable (Horng, Brun et al. 2014, Geith, Brun et al. 2018), to reach a cellular resolution, currently only small samples can be examined. Besides the currently limited sample size, the technique also still has a certain/high radiation dose, making it still an experimental technique for non-living samples if micrometer or sub-micrometer spatial resolution are used. Because of the limited granted experiment time on the specific beamlines, this study only has examined a limited sample number. There are still many elements we cannot interpret yet, such as when and why fiber bundles are visible or not visible. Some samples also show many dark spots, which are not understood yet; they may represent sediments caused by either storage time of the tissue in formalin, tissue preparation before or after imaging.

A potential application for the future

The capacity of details depictable within cartilage matrix architecture using X-ray PCI and the possibility to characterize different degradation stages could aid in the generation of a pictorial atlas, which might foster understanding of changes and possible implications for the biomechanical function of the cartilage tissue. This kind of knowledge – seeing these stages - is crucial for understanding the tissue properties, the way of its breakdown and also a potential way of healing and, therefore, potential points for intervention such as therapeutic options. Even though the technique still needs further refinement for future non-invasive applications on larger objects, it is already usable today as a tool for experimental studies with ex-vivo human or animal samples. Histology provides only 2D depiction and multiple preparation steps, e.g., calcification; cutting is necessary to produce histological plates. Whereas with the PCI imaging, the specimen only needs to be conserved in formalin and no staining, therefore the specimen is closer to their natural state than in histology. Moreover, with PCI, the imaged area is much larger than in histology due to the 3D data. Though histology and TEM can already provide a depiction of the cartilage tissue on a cellular basis, PCI provides an additional high-resolution technique, which despite the small samples, can visualize tissue in their native compound gaining information beyond the two-dimensional sections, but on a three-dimensional level, which might give more insight to the properties of cartilage tissue.

4.5. Comparison of X-ray Tube

Three different X-ray tubes were used to evaluate table-top source feasibility for high spatial resolution cartilage imaging. Table-top sources are, in principle, easier to access than synchrotron facilities.

4.5.1. Rotating Anode

The X-ray source used in this comparison is the XRayWorx source (located inWürzburg at the group NanoCT systems of the Fraunhofer Institute for integrated circuits) with an applied voltage of 100 kV, with an Al filter; the beam is a 60 keV pink beam. The distance between the source and the sample was 1.98 cm, and the samples to detector distance 23.95 cm. The imaging detector was the PE Dexela1512NDT CMOS detector from Perkin Elmer with a pixel size of 75 µm. The effective pixel at the sample position was 6.1 µm. The integration time was 0.5 s for a 180-degree scan with 1804 projections. Figure 4.12 shows that the CT image of a healthy sample acquired with the XRayWorx source is shown and compared with the data obtained at ESRF ID17 with an energy of 60 keV and an effective pixel size of 6 µm.

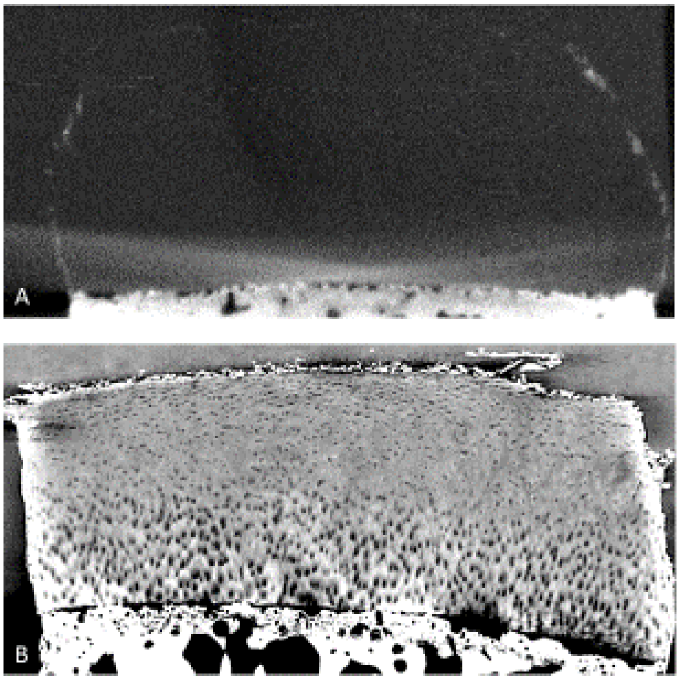

Figure 4.12 Two sagittal slices from a healthy cartilage sample with the same effective pixel size of 6 µm but with different X-ray sources. A) Rotating anode X-ray source; the edges of the sample are visible, but no other detail within the tissues are depicted B) Synchrotron radiation source (ID17); the cartilage structure (chondrons, interterritorial matrix) is well shown due to the additional phase signal.

The comparison is about the visibility of the structural part in cartilage. Figure 4.12 A) the cartilage part of this plug is not visible; only the edges are visible, but no structure of the cartilage "inside" is revealed. In comparison to that, the "inside" structure of the cartilage is observable in Figure 4.12 B), which is a sagittal slice taken at the synchrotron (ESRF ID17).

4.5.2. Liquid metal jet X-ray source

The spectrum of an X-ray tube is less brilliant than that of synchrotron radiation. Still, innovations based on the use of a liquid alloyed as anode material led to increased photon fluxes in the field of tube technology. The experiment with an Excillium X-ray liquid metal jet source took place at the Institute for X-ray physics at the Georg-August University of Göppingen/ Germany. The sample used for this experiment were healthy cartilage sticks (0.5 mm width x 0.5 mm depth x 1mm height) embedded in paraffin. For this experiment, the number of projections was 1800 projections over a 180 ° turn. The integration time for each projection was 20 s; therefore, the total acquisition time 13 hours. The effective pixel size was 0.5 µm. The reconstructed CT results are shown in Figure 4.13.

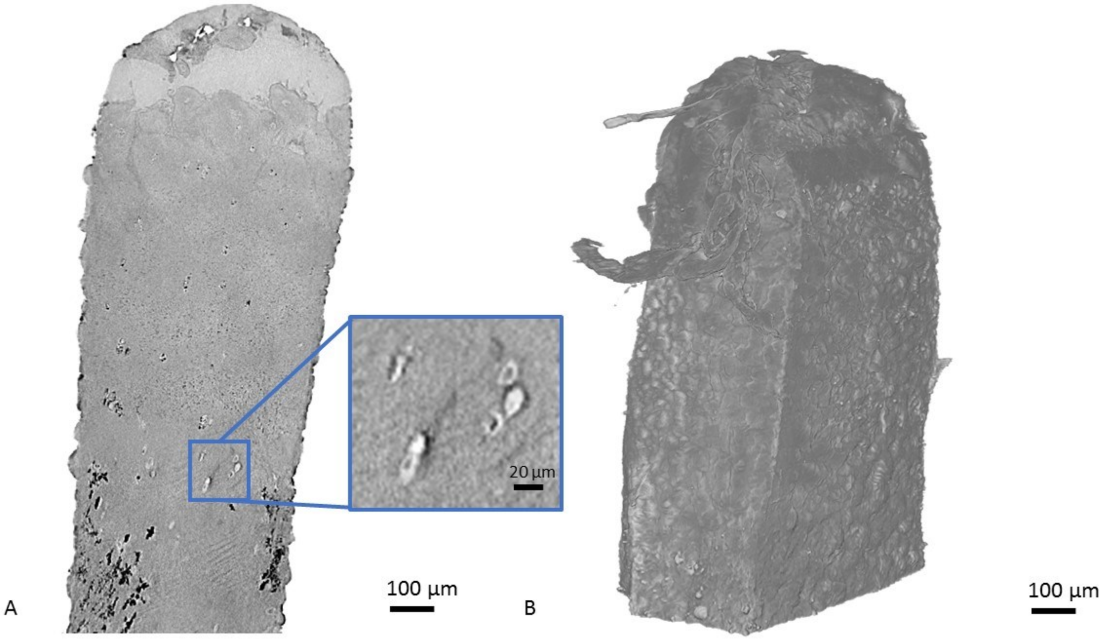

Figure 4.13 Images of a healthy cartilage stick embedded in paraffin acquired by using an Excillium liquid metal jet X-ray tube and an effective pixel size of 0,5 µm. A) sagittal view of cartilage B) 3D rendering of the volume

On the sagittal slice, single cells with the cell kernel area and cell cluster are observable, also parts of the interterritorial matrix. In figure 1.13 B, the 3D rendering of the same CT data set is shown.

In comparison with the high-resolution images from the synchrotron experiments, the liquid jet images cannot show the same details of a cell cluster and parts of the cell then synchrotron images. But it is possible to visualize the orientation and distribution of the cartilage cells. Due to the low energy range the liquid jet source provides, the sample needs to be small in diameter. Therefore only samples with a diameter of 0.5 mm could be imaged.

4.5.3. Nano focus X-ray tube

For this experiment, the "Nano Tube" from Excillium with the "SANTIS" detector from DECTRIS was used. The number of projections was 900 and the integration time was 50 second per projection, the acquisition time of a sample with a dimension of 0.5 mm width x 0.5 mm depth x 1mm height was 14 h long. The effective pixel size that was used was 450 nm. A comparison between the results obtained with the "Nano Tube" and those collected during synchrotron experiments is shown in Figure 4.14. Figure 4.14 A) reports an axial image of a healthy cartilage stick; chondrons are visible, the cell nucleus is no visible. The image in Figure 4.14 B) is from the high-resolution experiment at ID16a, with an effective pixel size of 100 nm. The acquisition time for that 3D data set of the healthy cartilage stick was 4 hours. The chondrons are observable, and the cell nucleus and fiber bundles in the cell matrix are visible.

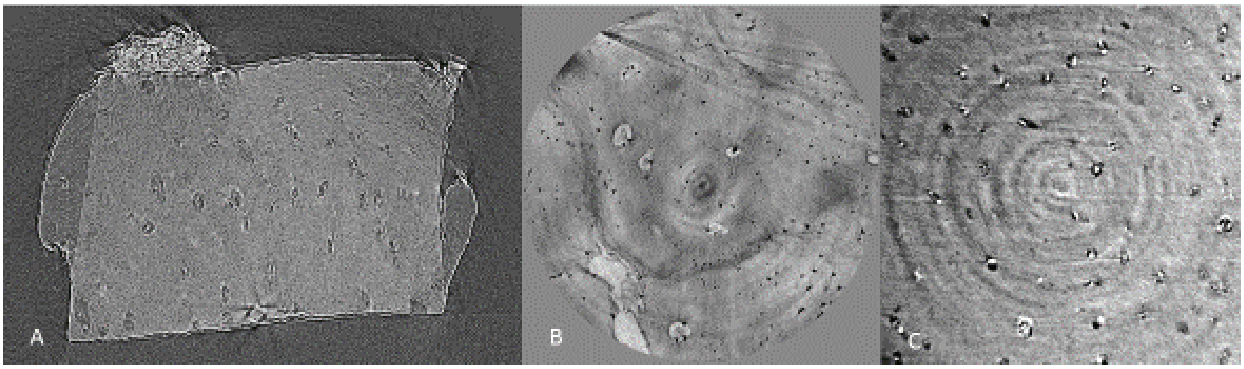

Figure 4.14 Three images of the same healthy cartilage sticks from different experimental sites with different sources and resolutions A) "Nano Tube" Excillium source; effective pixel size 450 nm B) ESRF ID16a synchrotron source; effective pixel size 100 nm C) TOMCAT SLS synchrotron source; effective pixel size 325 nm

The image C) of Figure 4.14 is from the TOMCAT beamline; it has an effective pixel size of 325 nm. Here the chondrons, as well as some cell nuclei, are visible on that image. The acquisition time for that image was about 15 min.

4.5.4. Discussion

The results obtained by applying PCI with a rotating anode X-ray tube are not comparable with the results obtained at a synchrotron. The rotating anode tube's coherence length is too small due to the extended source size and the low source to sample distance. No details can be seen in the experiment with the XRayWorx source, and the cartilage edge is hardly visible.

PCI-CT of cartilage samples using spatial resolution in the order of 300nm-500nm and small source sizes like in the "Nano Tube" Source is comparable with images acquired with synchrotron sources, as seen in Figure 4.14. The acquisition times are very large, with 13 h and 14h for the Liquid jet and "Nano Tube" respectively, compared to the times at the synchrotron with 4 h at ID16a and 15 min at TOMCAT. However, laboratory X-ray sources are easily available. In contrast, the synchrotron experiments need to go through a competitive review process, and beamtime is always limited to a few days.

Synchrotron CT dataset offers more detailed images, and the contrast is much better due to the higher flux and higher coherence of synchrotron radiation. This high flux also enables fast acquisition time.

4.6. Conclusion

In this chapter, the produced X-ray phase-contrast CT results show that it is possible to visualize cartilage with different spatial resolutions providing a different kind of information on the analyzed tissue. With the high-resolution (100nm effective pixel size), cell structures inside the cell could be depicted. With a lower resolution (about 0.7 µm effective pixel size) but a higher field of view, the cell distribution throughout the cartilage can be depicted. Early signs of degeneration, such as cracks, deformation of chondrocytes, could be seen at different scale levels.

The PCI images could be correlated with histology (Figure 4.5 - Figure 4.9) and TEM images (Figure 4.11) to verify the degradation signs and correctly interpret the PCI data. The 3D dataset can be used for "virtual" histology, which is a step forward.

X-ray phase-contrast imaging cannot only be performed at synchrotrons but also with standard lab X-ray sources. High-resolution X-ray phase-contrast images (450 nm – 500 nm) obtained with table-top sources can depict the cell structure, but not as detailed as with synchrotron sources of the same resolution. The acquisition of table-top X-ray sources for high-resolution PCI images (450 nm – 500 nm) takes about 13-14h, which is acceptable for cartilage samples embedded in paraffin because they didn't show any deformation signs. In general table-top X-ray source PCI setups are useful for experiments with a sample that does not change over the long acquisition (>12h).

The results reported in this chapter show that the table-top X-ray PCI setup can be a useful tool for cartilage and OA research. The technique can be a puzzle piece for understanding and visualizing the development of OA in cartilage.

Bibliography

Archer, C. W. and P. Francis-West (2003). "The chondrocyte." Int J Biochem Cell Biol **35**(4): 401-404.

Geith, T., E. Brun, A. Mittone, S. Gasilov, L. Weber, S. Adam-Neumair, A. Bravin, M. Reiser, P. Coan and A. Horng (2018). "Quantitative Assessment of Degenerative Cartilage and Subchondral Bony Lesions in a Preserved Cadaveric Knee: Propagation-Based Phase-Contrast CT Versus Conventional MRI and CT." AJR Am J Roentgenol **210**(6): 1317-1322.

Horng, A., E. Brun, A. Mittone, S. Gasilov, L. Weber, T. Geith, S. Adam-Neumair, S. D. Auweter, A. Bravin, M. F. Reiser and P. Coan (2014). "Cartilage and soft tissue imaging using X-rays: propagation-based phase-contrast computed tomography of the human knee in comparison with clinical imaging techniques and histology." Invest Radiol **49**(9): 627-634.

Horng, A., J. Stroebel, T. Geith, S. Milz, A. Pacureanu, Y. Yang, P. Cloetens, G. Lovric, A. Mittone, A. Bravi and P. Coan (2020). "Multiscale X-Ray Phase-contrast Imaging of human Cartilage for investigating Osteoarthritis Formation " Osteoarthritis and Cartilage **still under review**.

Li, J., Z. Zhong, D. Connor, J. Mollenhauer and C. Muehleman (2009). "Phase-sensitive X-ray imaging of synovial joints." Osteoarthritis Cartilage **17**(9): 1193-1196.

Lorenzo, P., M. T. Bayliss and D. Heinegard (1998). "A novel cartilage protein (CILP) present in the mid-zone of human articular cartilage increases with age." J Biol Chem **273**(36): 23463-23468.

Mittone, A., L. Fardin, F. Di Lillo, M. Fratini, H. Requardt, A. Mauro, R. A. Homs-Regojo, P.-A. Douissard, G. E. Barbone and J. Stroebel (2020). "Multiscale pink-beam microCT imaging at the ESRF-ID17 biomedical beamline." Journal of Synchrotron Radiation.

Mollenhauer, J., M. E. Aurich, Z. Zhong, C. Muehleman, A. A. Cole, M. Hasnah, O. Oltulu, K. E. Kuettner, A. Margulis and L. D. Chapman (2002). "Diffraction-enhanced X-ray imaging of articular cartilage." Osteoarthritis Cartilage **10**(3): 163-171.

Pearle, A. D., R. F. Warren and S. A. Rodeo (2005). "Basic science of articular cartilage and osteoarthritis." Clin Sports Med **24**(1): 1-12.

Schmid, T. M. and T. F. Linsenmayer (1985). "Immunohistochemical localization of short chain cartilage collagen (type X) in avian tissues." J Cell Biol **100**(2): 598-605.

Schumacher, B. L., J. A. Block, T. M. Schmid, M. B. Aydelotte and K. E. Kuettner (1994). "A novel proteoglycan synthesized and secreted by chondrocytes of the superficial zone of articular cartilage." Arch Biochem Biophys **311**(1): 144-152.

5. Cartilage X-ray imaging at rest and under pressure conditions

The mechanisms with which the cartilage tissue reacts to loading and how it relaxes are not well understood yet. Daily activities, such as walking, running, or sports, subject the articular cartilage to stress and pressure, and the biomechanical response of the tissue may change between healthy and pathological tissues. In order to shed light on this question, two experiments have been designed to image cartilage plugs extracted from human knee joints while applying different pressures to them. X-ray phase-contrast microtomography was used to visualize the morphological changes induced in the tissue by compression in 3D.

This work's objective was to develop an experimental and analytical methodology to quantify and visualize the cartilage structure in 3D, cell distribution and tissue mechanical behavior at rest and under load conditions in healthy and degenerated tissue specimens. The series of routines tested and optimized for this analysis have been described in section 5.3 (Image processing). This quantitative study targets the resident cartilage cells, which are the chondrocytes or clusters of chondrocytes. Chondrocytes have many tasks within the cartilage structure; they provide a new matrix and repair the existing one. The segmentation of the tissue cells is done with the WEKA machine learning toolbox, performing a decision tree algorithm, as described in the method section. After the segmentation, an object counting function is applied to the segmented data, which provides quantitative information on the chondrocytes within the selected region of interest, i.e., the cell volume and the mean standard deviation distance to the surface (msdds). The latter measures the mean standard deviation distance to the surface and indicates the shape of the chondrocyte/chondron: a sphere has a lower msdds than a cylindrically shaped object. In the next step, the skeletonization of the chondrons, the length and the angle of the chondrons are calculated.

These experiments and the data analysis were performed in collaboration with a Master student (Thomas Vannieuwenhuyse) who was working within a group and whom I have directly co-supervised. I assigned Thomas mainly the CT data reconstruction part, the software's implementation and the visualization of the results. All ideas and input for data analysis and the quantification method came from my side, as well as the organization and preparation of the experiment at the ESRF (including the choice of the experimental setup and the adaptation of the sample environment).

Part of the work reported in this chapter is presented in the published article "TomoPress—In Situ Synchrotron-Based Microtomography under Axial Load" which together with Alexander Rack was published in the journal Instruments (Rack, Stroebel et al. 2020).

5.1. Cartilage and Pressure

Human cartilage in the knee joint is always under pressure when walking or standing. Experiments reported in the literature have revealed that on the knee joint, which is one of the most stressed synovial joints in humans, the average magnitude of the applied force is 150 ± 70 % of body weight while standing, and this goes up to a maximum of 250±60% of body weight for walking during the process of flexion and extension (Glitsch, Lundershausen et al. 2009). Biomechanical studies with the human knee were conducted. The pressure got a record with electronic pressure-sensitive film to find the pressure distribution in the medial joint space. The tibial plateau was measured with a three-dimensional tracking system. (Agneskirchner, Hurschler et al. 2004, Lee Koh, Kowalski et al. 2006, Agneskirchner, Hurschler et al. 2007) These Biomechanical studies show the pressure distribution and movement in between the cartilage. For simulation within the cartilage, finite element simulation is used based on magnetic resonance imaging (MRI) (Corezzi, Urbanelli et al. 2009, Mononen, Mikkola et al. 2012) or based on X-ray images (Maki, Inou et al. 2003). With angle-sensitive nuclear magnetic resonance, the orientation of the collagen network structure could be depicted under pressure. This experiment used small cylindrical plugs harvested from a patella or a femur (Gründer, Kanowski et al. 2000). A study in 2002 about the quantitative structural feature of articular cartilage with confocal microscopy was carried out. From semi-thin slices, 2D microscope images are taken, and the volume is then calculated with stereological estimators (Hunziker, Quinn et al. 2002). The only three-dimensional study of pressurized cartilage found in the study of Youn Choi, et al. from 2007; they used confocal microscopy in combination with immunolabeling of type VI collage to identify the border of the cartilage cells. Pressure with different strains was applied to the pig cartilage plugs (5 mm in diameter), which got buffered with phosphate saline and fixed under pressure with 4% paraformaldehyde. 40 µm thick sections were cut from each fixed block (Choi, Youn et al. 2007).

All the mentioned studies show the effect of pressure on the outside layers of cartilage, simulate the cartilage, or they are destructive and estimate the 3D properties from the 2D image. The only two exceptions are the NMR study on the collagen structure and the 3D confocal measurements on pressurized cartilage. However, these works are again destructive, and samples need to be fixed. In this chapter I present a study in which the 3D cellular distribution within a large cartilage sample (7mm diameter) and its modifications under pressure conditions are obtained with great detail, without the need for sample fixation or labeling.

5.2. Sample preparation and experimental setup

This experiment was performed at the micro-tomography beamline ID19 of the ESRF. The samples were harvested from two human knees. Thirteen plugs were drilled from the femur and patella cartilage. The osteochondral plugs had a diameter of about 7 mm and consisted of a cartilage part and a bone part. Half of the samples were healthy (samples 1-7), while the other half showed signs of degeneration associated with the early stages of osteoarthritic disease (samples 8-13). Most plugs came from the femur cartilage, except for samples 9, 12 and 13, which were parts of the patella. Before imaging, each plug's length (along with the cylinder axis) and the height of the cartilage layer and bone portion were measured. The sample length varied between 9.7 mm (sample 1) and 21.3 mm (sample 6). The cartilage height varied between 1.8 mm (sample 7) and 5.0 mm (sample 13). The average diameter of one plug is 7.1 mm. These measurements are reported in Table 5.1, and the estimated error of these measurements is ±0.5mm. In the last column of the table, the number of different pressures applied to each sample is indicated.

Sample	***Body part***	***Tissue degeneration***	***Total length*** *(mm)*	***Cartilage thickness*** *(mm)*	***Bone thickness*** *(mm)*	***Diameter*** *(mm)*	***Pressure points imaged***
S1	Femur	No	9.7	2.3	6.3	7.2	3
S2	Femur	No	16.4	2.9	12.6	7.2	3
S3	Femur	No	11.0	2.8	7.7	7.0	6
S4	Femur	No	15.1	3.0	10.1	6.9	3
S5	Femur	No	12.8	2.2	10.9	6.8	3
S6	Femur	No	21.3	2.3	18.1	7.6	6
S7	Femur	No	17.9	1.8	16.5	7.2	3
S8	Femur	Yes	11.5	2.3	8.0	7.2	6
S9	Patella	Yes	15.8	4.0	10.8	7.1	3
S10	Femur	Yes	18.4	2.2	16.3	6.1	3
S11	Femur	Yes	11.9	2.1	9.0	7.1	3
S12	Patella	Yes	13.4	4.7	9.2	7.3	3
S13	Patella	Yes	18.3	5.0	10.7	7.4	3

Table 5.1 Measured samples' length and height of the cartilage and bone portions of each sample. In the last column, the number of different pressures applied to each sample is reported.

The X-ray beam energy was filtered-polychromatic and had mean energy of around 26 keV. The FReLon detector was used, which is a 14 bit dynamic CCD camera and has a 2048x2048 pixels chip with a pixel size of 14 µm. With the coupled X-ray optics, an effective pixel size of 5.1 x 5.1 μm^2 was achieved. The propagation distance between the sample and the detector was 5 meters.

The tomopress is a mechanical press with a horizontal rotation stage built-in. This press was designed by Pierre Bleuet and Yves Dabin, engineers at the ESRF, and is a unique device dedicated initially to experiments on a bone (Bleuet, Roux et al. 2004). The tomopress can apply a maximum pressure of 400 N. For this experiment, I had to design special adapters, which were then manufactured and installed to hold the sample in place in order to apply the forces homogeneously onto the sample surface.

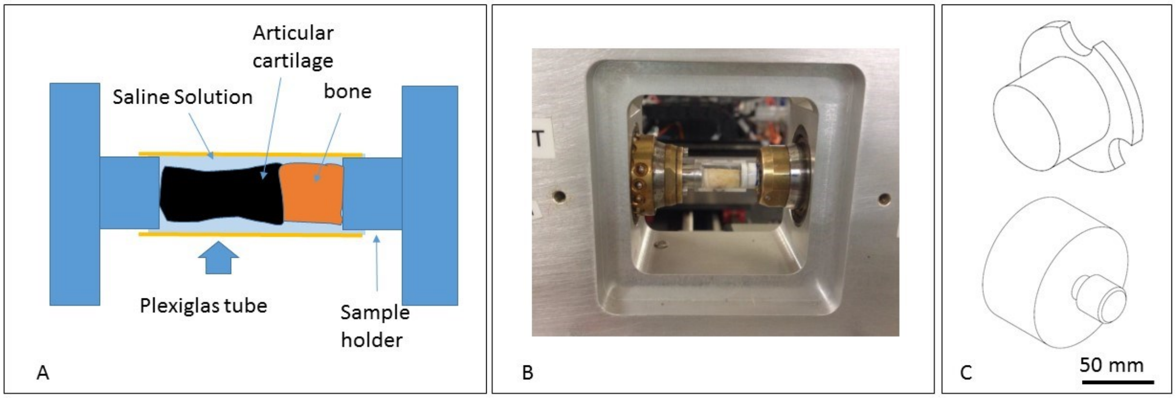

Figure 5.1 Tomopress configuration for the dynamic cartilage experiment: a schematic setup of sample holder, a Plexiglas tube surrounds the sample to keep it in water to prevent dry out; the Plexiglas tube was fixed on one side; B picture of sample in the tomopress; C drawings of the customized sample holder to apply a homogenous force onto the samples' cartilage surface.

For each CT scan, 2000 projections were acquired in a "step and shoot" mode in order to reduce the dose on the sample; the integration time was 0.2s per angular projection. During scans, samples were in a Plexiglas cylindrical container within a saline solution. One side of the cylinder (on the bone part of the specimen) was sealed with plastic fermit, on the other side, the tomopress could slide into the tube to apply pressure on the cartilage surface. A scheme is shown in e.

5.3. CT data reconstruction and image processing

The workflow of the image processing applied to the collected image datasets is described here. The different steps of the analysis were:

1) CT reconstruction using the sets of acquired angular projections in order to to obtain a 3D volume of the imaged specimens;

2) Selection of the region of interest to be considered for the analysis: the purpose is to remove the edge of the cartilage plug, thus reconstructing artifacts that appear in that area;

3) A filter is applied to the sagittal images obtained by reslicing the reconstructed volume data; this operation is performed to enhance the contrast;

4) The segmentation of the cartilage cells;

5) Cell counting on the segmented datasets to extract quantitative parameters such as volume or surface of the segmented cells;

6) All the cells are reduced to a line of pixels by skeletonization in order to determine the cell orientation within the cartilage tissue.

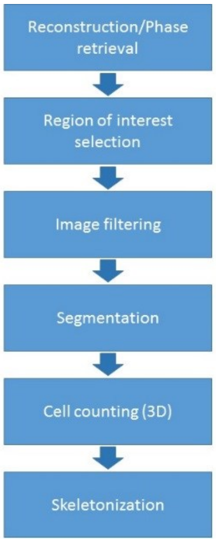

Figure 5.2 Schematic workflow of image processing

5.3.1. CT reconstruction

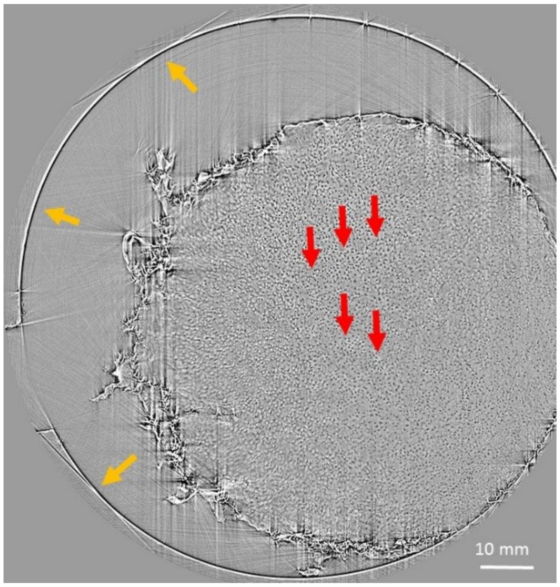

Figure 5.3 reconstructed axial slice of articular cartilage within the Plexiglas tube (green arrow); chondron structure is visible

The reconstruction of the acquired CT data sets was done with the PyHST2 software implemented at the ESRF (Mirone, Brun et al. 2014). Included in the software is the possibility for calculation of a single distance phase retrieval (the so-called "Paganin phase retrieval"), as described in chapter three. For phase retrieval, the following parameters were used:

- Paganin length: 1123.6
- Paganin marge: 110

Figure 5.3 is a reconstructed axial slice of a cartilage plug. There are small dark spots in the cartilage, which are the cells of the cartilage matrix (chondrons, red arrow). The large ring on this image is the Plexiglas container's cylindrical wall filled with saline solution (green arrow). The cartilage plug is jagged on the outside border because of the drilling process. The visible artifacts, i.e., vertical strips, come from these discontinuities on the cartilage's surface. For the quantitative analysis, the cartilage's outer layer was therefore removed as described in the next paragraph.

5.3.2. Selection of the region of interest

For each dataset, a region of interest (ROI) corresponding to the cartilage tissue and excluding the outer part, which contains artifacts needed to be selected. To do that, all the numbers of the slices of each reconstructed volume containing the cartilage tissue were selected manually and saved in a text file.

In a second step, an automatic localizer was designed to find the area covered by cartilage tissue within each slice. This tool detects circles with a radius within a given range in each 2D CT slice and returns the mean center and mean radius. The output of the routine is the averaged center and radius of all slices in the volume stack. The ROI for the volumetric stack is calculated from the mean average center. The underlying Python function is the 'HoughCircles' from the module OpenCV2. The Hough Circle function is based on the Hough Gradient transformation. The Hough Gradient transformation detects edges in the image and draws an orthogonal line at that edge. The average of the interception of these lines is the approximated center of the circle (Yuen, Princen, Illingworth, & Kittler, 1990). More information about the circle detection method can be found in the OpenCV2 online documentary[13].

The results of the multiple circle detection are shown in Figure 5.4. There can be some outlier in some detection iteration, but on average, the method finds a circle center close to the center of the cartilage disc.

---

[13] https://docs.opencv.org/2.4/modules/imgproc/doc/feature_detection.html

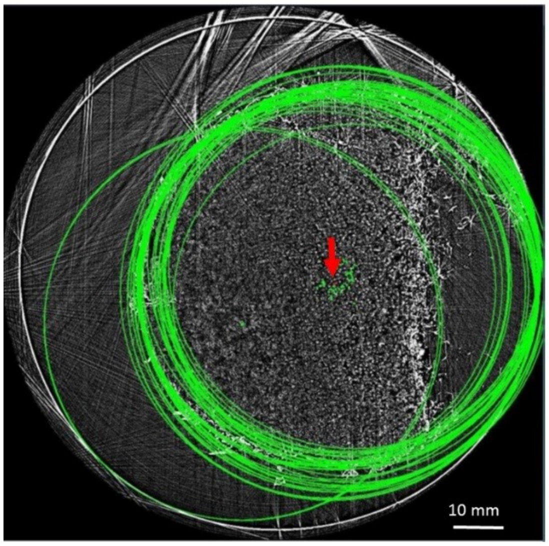

Figure 5.4 For every 2D slice (axial), the Hough Circle function calculates the center of a circle based on the edge of the sample. The red arrow indicates the average center of the circle throughout the volumetric 3D stack.

The calculated mean circle center and radius of one 3D stack are saved in a file. This calculation is repeated for all samples.

The first slice with cartilage on it and the last slice at the interface with bone on the axial image is determent by hand. This information is used together with the circle center and radii to crop volume occupied by the cartilage tissue from the full 3D volume data. In the last step of this tool, a circular mask is applied with a radius of 0.9 times the calculated averaged sample radius on each slice. This is done to make sure to exclude the jagged sample borders.

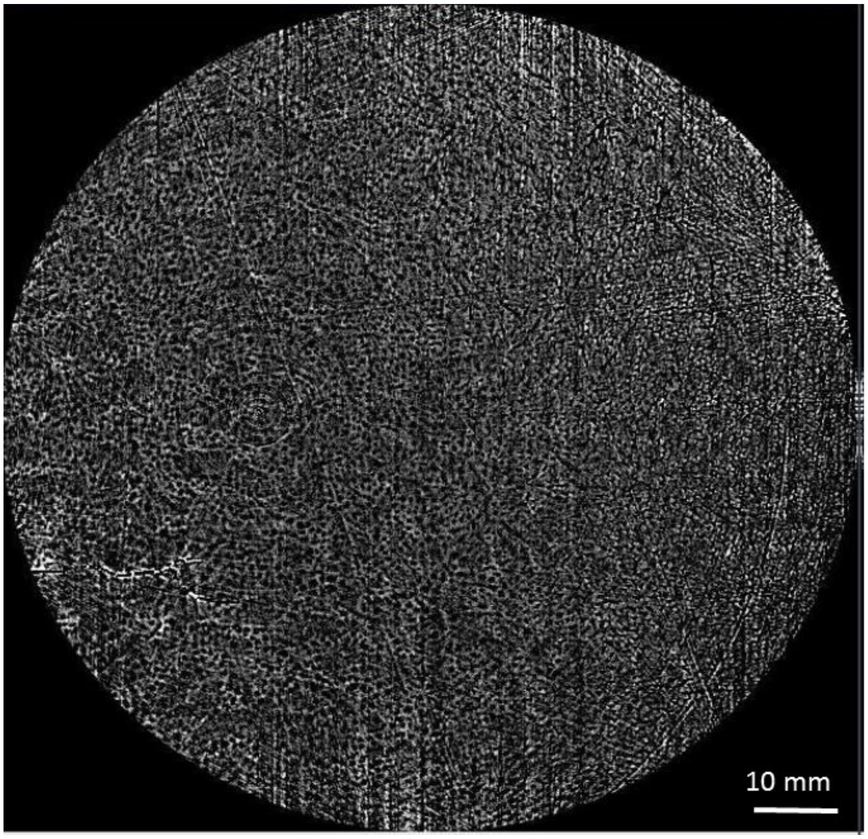

Figure 5.5 Exemplary slice after complete ROI selection of sample 12 with 0 N pressure stage. Black dots are chondrocytes. A cartilage crack can be seen in the lower left.

5.3.3. Image filtering

The next step in the workflow is to apply filters to the selected cartilage data to enhance chondrocytes and cartilage constituents' contrast.

Contrast enhancement (windowing)

The contrast stretching windowing method is used to enhance the contrast of the cartilage cells. New upper and lower pixel values are defined. Pixels with values above (below) these boundaries are saturated and set to the boundary value, and the values in between are scaled to the new range (e.g., stretching of the histogram).

$$P_{ec} = (P - c)\left(\frac{b - a}{d - c}\right) + a \qquad (5.1)$$

Where P (Pec) is the initial (contrast-enhanced) pixel value, a,b the initial value limits (0 and 255 for a 8-bit grayscale image), and c, d the new limits. The setting, e.g., c and d at the $5th$ and $95th$ percentile of the image histogram will saturate the 5% of the pixels with the lowest and highest values, and stretch the values in-between a and b (Fisher, Perkins et al. 2003).

Total Variation filter

The total variation filter is a denoising algorithm first proposed by Rudin and co-authors in 1992 (Rudin, Osher et al. 1992). Let us assume a noisy 2D signal (e.g., a noisy image). We can define the total variation of the signal as

$$J(u) = \sum_{i,j} \sqrt{\left|u_{i+1,j} - u_{i,j}\right|^2 + \left|u_{i,j+1} - u_{i,j}\right|^2} \tag{5.2}$$

where $u_{i,j}$ denotes the (noisy) signal at each pixel position *i,j*. Using the Euclidean norm, or sum of the square errors, as a measure of closeness between the noisy signal u and the denoised signal g

$$E(u,g) = \|u - g\|^2 = \frac{1}{2}\sum_{i_1 j}(u_{i,j} - g_{i,j})^2 \tag{5.3}$$

The total variation algorithm now becomes a minimization problem of J subject to constraints involving the noisy signal. That is, to find a signal g close to u but with a lesser total variation.

$$min_u E(u,g) + \lambda J(u) \tag{5.4}$$

With λ being the regularization parameter. If λ is set too high, the resulting image will still have less total variation than the noisy image but have less resemblance to it. If λ = 0, the problem reduces to the minimization of the sum of square errors.

The total variation denoising allows the averaging of pixel values in a specific area while preserving essential details like edges, critical features in PCI images. Applied to our data, it averages contrast variations within the intercellular matrix as well as within the chondrocyte while not blurring the chondrocyte edges. It is essential for our analysis.

The implementation of the total variation denoising algorithm in Python is done via the *restoration* module of the *skimage*[14] plugin, which is based on Chambolle's formulation of the problem (Chambolle 2004):

restoration.denoise_tv_chambolle(img, weight=0.3)

It takes the image and weight as arguments; the weight argument is the regularization parameter λ from the equation (5.4).

Contrast enhancement and total variation denoising filters are both applied to each ROI dataset. A careful comparison of the results obtained by using different settings for the involved parameters showed that the best outcomes are:

- for contrast enhancement: saturation of the lowest 2% and highest 2.8% of pixel values
- For total variation denoising: weight parameter, $\lambda=0.3$.

---

[14] http://scikit-image.org/

5.3.4. Image segmentation with advanced machine learning

The WEKA segmentation tool was used for this step, the procedures of which are based on machine learning algorithms.

WEKA is an acronym for *"Waikato Environment for Knowledge Analysis"* and was developed in Java at the University of Waikato in New Zealand (Witten, Frank et al. 2016). It is distributed as free software licensed under the GNU General Public License. It is available as a plugin in the open-source image processing environment Fiji[15] (based on ImageJ) (Arganda-Carreras, Kaynig et al. 2017). In the graphical user interface (GUI) of the *Trainable Weka Segmentation* plugin, the user can select areas manually within the loaded 2D or 3D image dataset and then assign these areas to a class. In this case, two classes are defined, one for chondrocytes and one for the background/matrix. The pixels within these areas are then assigned to the defined classes. Five *Training features* are used to train the classifier. On every assigned pixel in every class, the five selected features are calculated. As a classification algorithm, the *FastRandomForest* is selected (Ho 1995). This algorithm initializes multiple *decision Trees*. One decision tree has different leave nodes, which are the classes for the classification problem. And a decision tree has decision nodes. The decisions made in these nodes are based on the information gain, calculated by the Gini coefficient. (Kamiński, Jakubczyk et al. 2018)

To prepare a training dataset to construct the decision trees, about 200 pixels in a training image were assigned to a specific class. Different filters were applied to the training image to extract multiple features from every assigned pixel. The following filters were used: the *Gaussian blur filter, Sobel filter, Hessian filter, the difference between Gaussian filters and the membrane projection filter*. From the extracted features of the assigned pixel, the classifier with 200 decision trees was constructed.

The classifier is applied to the images, the segmentation should be performed. This classifier assigns a specific class to every pixel in the images based on the decision tree's outcome. Based on that classification, the segmentation can be done.

A screenshot of the WEKA plugin GUI is reported in Figure 5.6, together with the settings window. Some initial background and chondrocyte areas have already been traced, and the classifier can be trained via the *Train classifier* button. After successful classification, the result can be displayed and saved with the *Create result* button for further data analysis (more details in the official WEKA documentation (Witten, Frank et al. 2016)).

---

[15] http://fiji.sc/

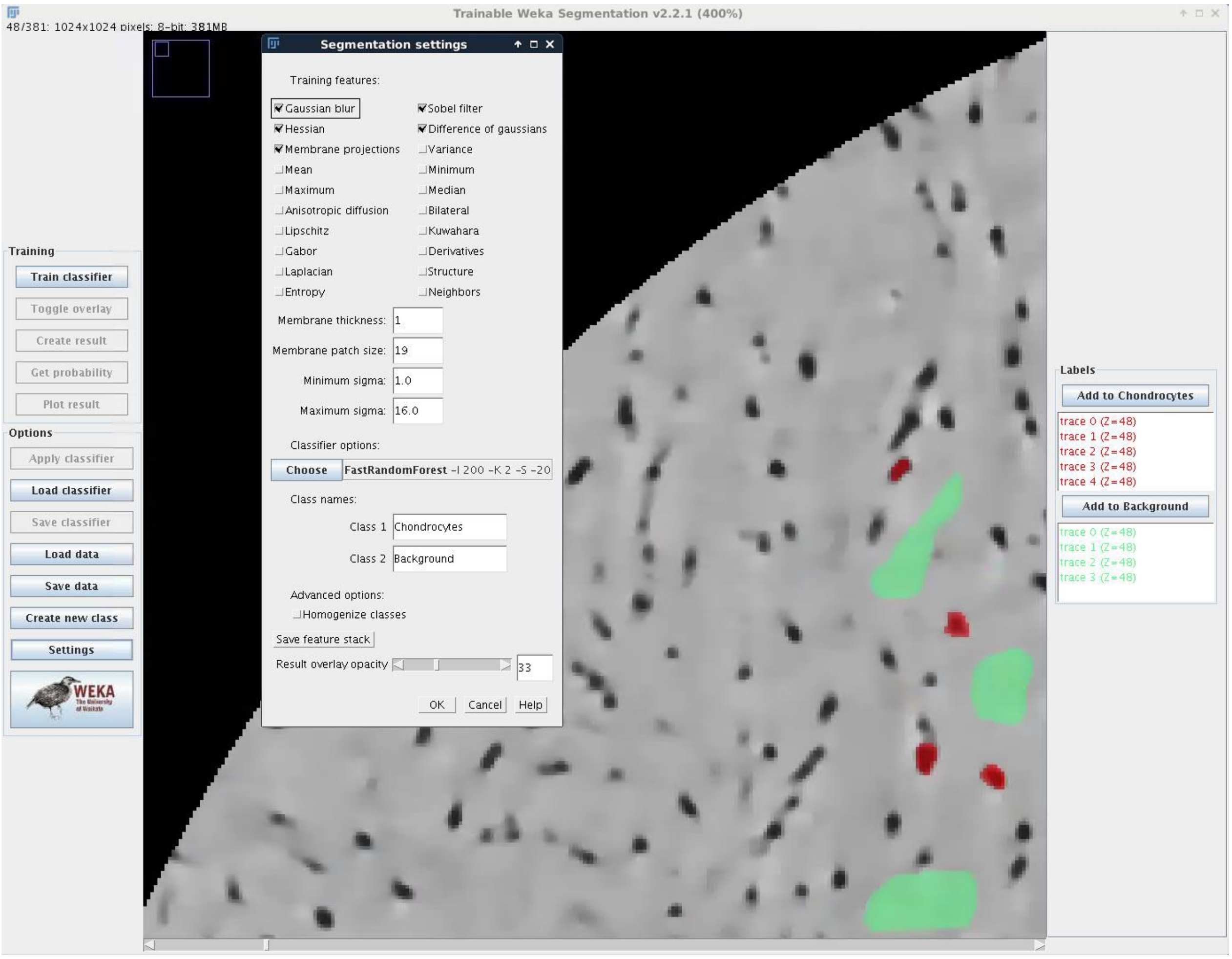

Training features:

☑ Gaussian blur ☑ Sobel filter
☑ Hessian ☑ Difference of gaussians
☑ Membrane projections ☐ Variance
☐ Mean ☐ Minimum
☐ Maximum ☐ Median
☐ Anisotropic diffusion ☐ Bilateral
☐ Lipschitz ☐ Kuwahara
☐ Gabor ☐ Derivatives
☐ Laplacian ☐ Structure
☐ Entropy ☐ Neighbors

Membrane thickness: 1
Membrane patch size: 19
Minimum sigma: 1.0
Maximum sigma: 16.0

Classifier options:
Choose FastRandomForest -I 200 -K 2 -S -20

Class names:
Class 1 Chondrocytes
Class 2 Background

Advanced options:
☐ Homogenize classes

Save feature stack
Result overlay opacity 33

OK Cancel Help

Figure 5.6 Screenshot of the GUI of the Trainable Weka Segmentation plugin in Fiji. Some chondrocytes (red) and background areas (green) are labeled. In the opened settings window, the training features of the machine learning algorithm can be checked. The Train classifier button can initiate training, and the segmentation result can be obtained via the Create result button.

5.3.5. 3D Cell Counting

After creating a dataset with the segmented chondrons and chondrocytes, the quantitative analysis of the cartilage cell characteristics and distribution can be performed. The first quantity that can be measured is the size of the cells. This was done with the *3D Objects Counter* function of Fiji (Analyze – 3D Objects Counter). A binary 3D dataset (mask) is given to this function. In the first step, the function is looking at a segmented pixel (value 1) and its neighboring pixels, if the neighboring pixel is also segmented (value 1), the function groups them as one object. This is done for all pixels. A different natural number is assigned to every grouped object of the binary volume. Using this assigned number, the number of objects can be counted. In a second step, the function looks at every object individually and measures the following values:

- Number of voxels in an object (Volume)
- Number of pixels at the edge of the object (Surface)
- Centroid or geometric center of the object
- Mean distance from the centroid to the surface of the object
- The standard deviation of the distance from the centroid to the surface of the object

- The bounding box (cuboid around the object)

These results are saved in a .csv file and can be extracted and plotted with a dedicated Python script. Filters are applied to exclude objects that are not chondrocytes: features with a volume larger than 20000 μm^3 ($\triangleq 151$ px^3) or with a surface larger than 5000 μm^2 ($\triangleq 193$ $px2$) are excluded. Besides, the *3D Object Volume analyzer* function creates three different "maps": one "map" (object map) with the result of step one, where every object has an assigned number, one "map" (surface map) with the surface voxels of each object and the third "map" (centroid map) with the position of the centroid of every object.

5.3.6. Image skeletonization for cell orientation quantification

The next step in the workflow is the skeletonization of the cells. The aim is to calculate the cells' length and the angle between the cells' central axis and the rotation axis of the cylindrical specimens (assuming the rotation axis of the tomopress is orthogonal to the sample surface). The Fiji plugin *Skeleton* is used to extract the chondrocytes' central axis from the obtained segmentation masks, produced in section 5.3.4. The skeletonization works by iteratively removing the one voxel layer on the edge (surface voxel) of the object. This is done until the innermost voxels are left. The result is a "skeleton" of each object, consisting of at least one branch. If the object is a perfectly round sphere, the skeletonizing result is one branch, which corresponds to one pixel, i.e., the sphere's center. The more complex the object, the more branches we get are identified in the skeleton. The *Analyze Skeleton* plugin provides the following features:

- Number of branches
- Number of junctions
- Average branch length
- Maximum branch length
- Bounding rectangle (minimum and maximum position of skeleton voxel in every direction)
- Start and end positions of the skeleton

The *plot_angles* function of the Python script **features.py** compares each start and endpoints of every branch in a skeleton. The longest distance is assumed to be the object's central axis. The encompassing two points allow calculating the angle of the object with respect to the sample rotation axis. This angle corresponds to the orientation of the object (cell) within the specimen.

5.3.7. Estimation of the segmentation and counting error

To evaluate the quality of the segmentation procedure, a test was performed to evaluate the counting error. First, four images were segmented with the WEKA machine learning segmentation tool and then cells/objects counted with the object counter. The same images were shown to 10 observers, with the task to count the cells. No restriction indications on how to count were given. After training the WEKA algorithm, the WEKA tool provides a probability map for cells and a matrix for the segmentation part. The pixel with a 75 % probability of being a cell is segmented. In the object counting part, segmented parts, five or more pixels are counted as one cell to filter out the noise. The images are shown in Figure 5.7

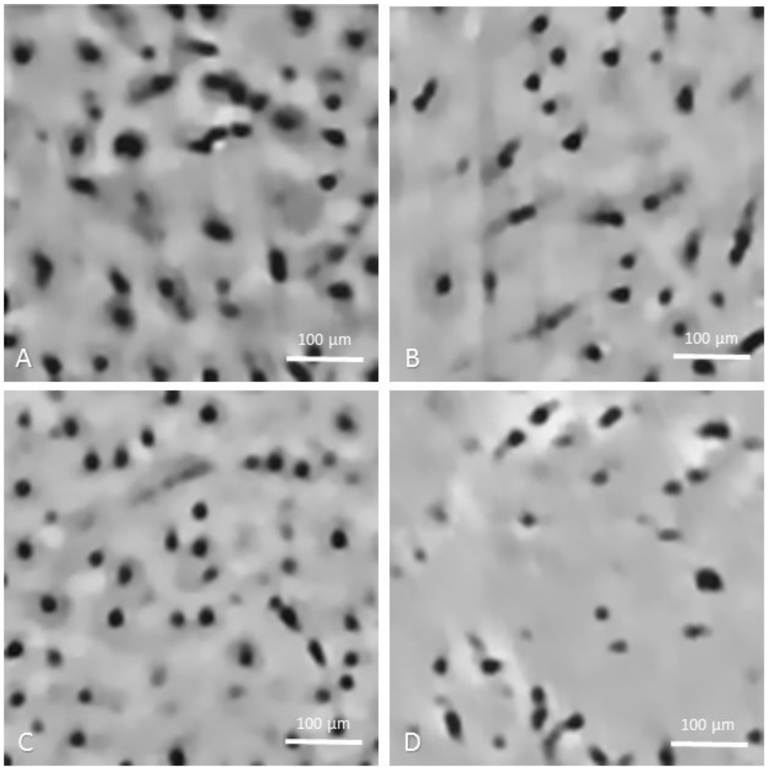

Figure 5.7 sagittal slice from 4 different heights of the cartilage for evaluating the accuracy of the segmentation and counting algorithm.

The following table shows the result of 10 persons who counted the cells.

Slice	***A***	***B***	***C***	***D***
Person 1	48	33	45	26
Person 2	50	36	48	28
Person 3	46	38	47	27
Person 4	47	34	48	30
Person 5	51	39	49	32
Person 6	51	38	49	31
Person 7	56	37	50	31
Person 8	45	35	51	31
Person 9	45	34	52	29
Person 10	47	37	42	25
Person Avg	48,6	36,1	48,1	29
Segmentation	45	33	48	25

Table 5.2 Chondrocyte count on cropped test slices for error estimation. Compared are counts of colleagues (unfiltered image), personal count (unfiltered image) and WEKA counts (unfiltered, filtered and Paganin image).

The average of the counting of the persons for Figure 5.7 A is 48,6, for Figure 5.7 B is 36,1, for Figure 5.7 C is 48,1, and for Figure 5.7 D is 29. For all four cases, the observers' counting results were always higher than the results obtained with the applied routines, except for image C. The reason for this discrepancy is that human eyes count cells, which are close together as two, whereas the algorithm does count such cases as one cell. There is only 0.1 difference between the observers' data and the algorithm count in image C because most cells are separated. Errors increase when cells are close one to the other.

5.4. Results

In this section, the CT results of this study are presented, and the cartilage tissue response (in terms of structure alteration) to the applied forces is qualitatively described. In the second part, the cartilage cell distribution and structure are quantified in the different considered cases.

The acquired CT datasets were reconstructed, and a series of axial CT slices (covering the entire volume of each osteochondral plug) was produced per each sample. Volumes were then resliced using ImageJ to obtain a sagittal view of the cartilage specimens, which allows for full representation of the different cartilage layers. Close to the bone surface, the chondrocytes/chondrons are vertically aligned. Close to the cartilage surface, chondrocytes are horizontally aligned. The white (brighter) color in the following images are material with high electron density, like bone, and the black parts have a low electron density instead. In Figure 5.8 A, the bone is at the top of the image, while the cartilage is below the bone. The CT image shown corresponds to a case in which no pressure is applied to the sample (sample at rest). The black dots within the cartilage are the chondron cells; the gray part is the interterritorial matrix. The superficial zone is not visible in this experiment because the top cartilage layer is in contact with the tomopress. In these images, the bone signal is partially saturated to increase the visibility of the soft tissue.

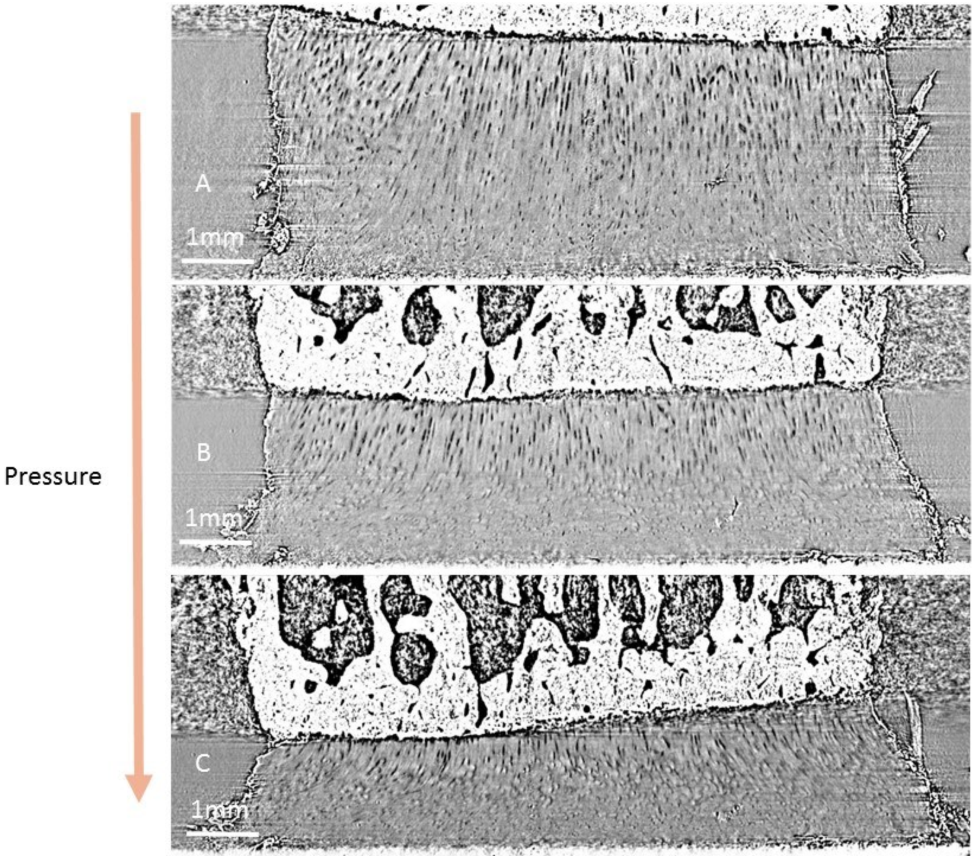

Figure 5.8 Sagittal images of osteochondral plugs subject to different pressures; A) no pressure on cartilage; B) medium pressure on the cartilage (12,4N); C) highest pressure on the cartilage (24N), i.e., largest compression of cartilage.

Figure 5.8 B and C show two sagittal slices of the same osteochondral plug to which different pressures are applied. The applied forces on this plug were 12,4 N (B) and 24 N (C). The compression is visible by the lateral enlargement of the cartilage tissue. The cartilage's compression causes a reduction in height, which is 29 % with respect to condition A (cartilage at rest) for case B and 53 % for case C. The lateral expansion of cartilage is comparable in B and C.

5.4.1. Artifacts due to compression

Without pressure, the cartilage matrix is very homogenous. This changes when force is applied to the cartilage. Figure 5.9 A is an axial slice of sample 2 at rest. When pressure is applied, the interterritorial matrix gets deformed as visible in the regions indicated by red arrows in Figure 5.9 B. When the applied force increased, the area of deformation becomes larger (Figure 5.9 C).

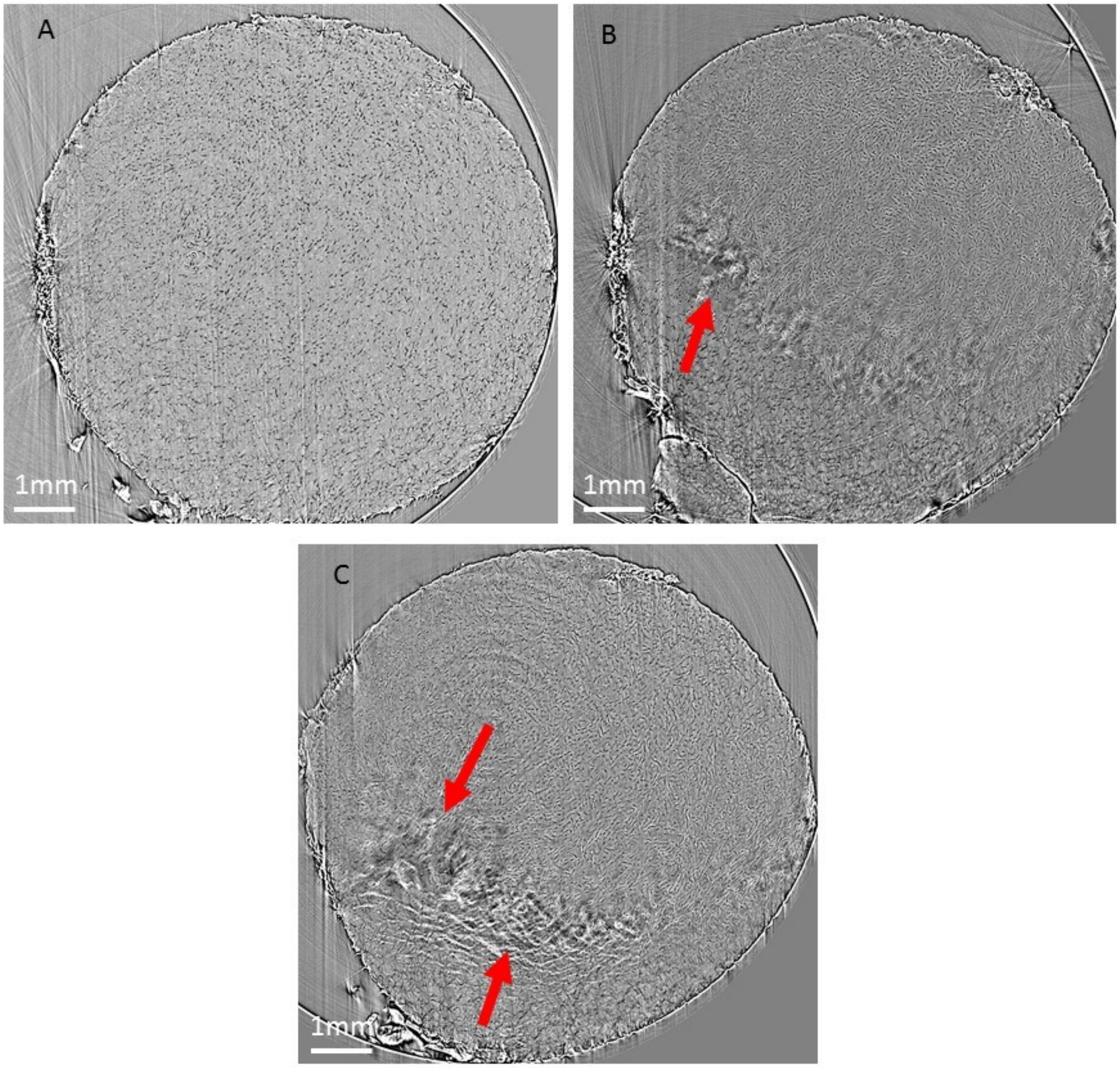

Figure 5.9 Axial image of the cartilage tissue of sample 2 at different pressure points; A) no pressure applied; B) pressure of 9 N; C) applied pressure of 30 N. The red arrows indicate the deformation of the cartilage under pressure conditions.

The cartilage tissue alteration can also be seen in the sagittal view (red arrows in Figure 1.11B and C). Again, Figure 5.10A corresponds to the case at rest, with no pressure applied. In Figure 5.10 B the applied pressure is 9N and C is 30N. The compression artifact area in Figure 5.10B (red arrow) is parallel to the cartilage surface, whereas in Figure 5.10 C the compression effects describe an arc (red arrow). The effect regions are shifted between images B and C. This kind of compression effect within the cartilage matrix can be seen in every sample we imaged. In Figure 5.10B and C, other artifacts within the cartilage tissue are visible (indicated by a star symbol); they derive from the bone (discontinuities in the refraction index). These artifacts appear like horizontal lines.

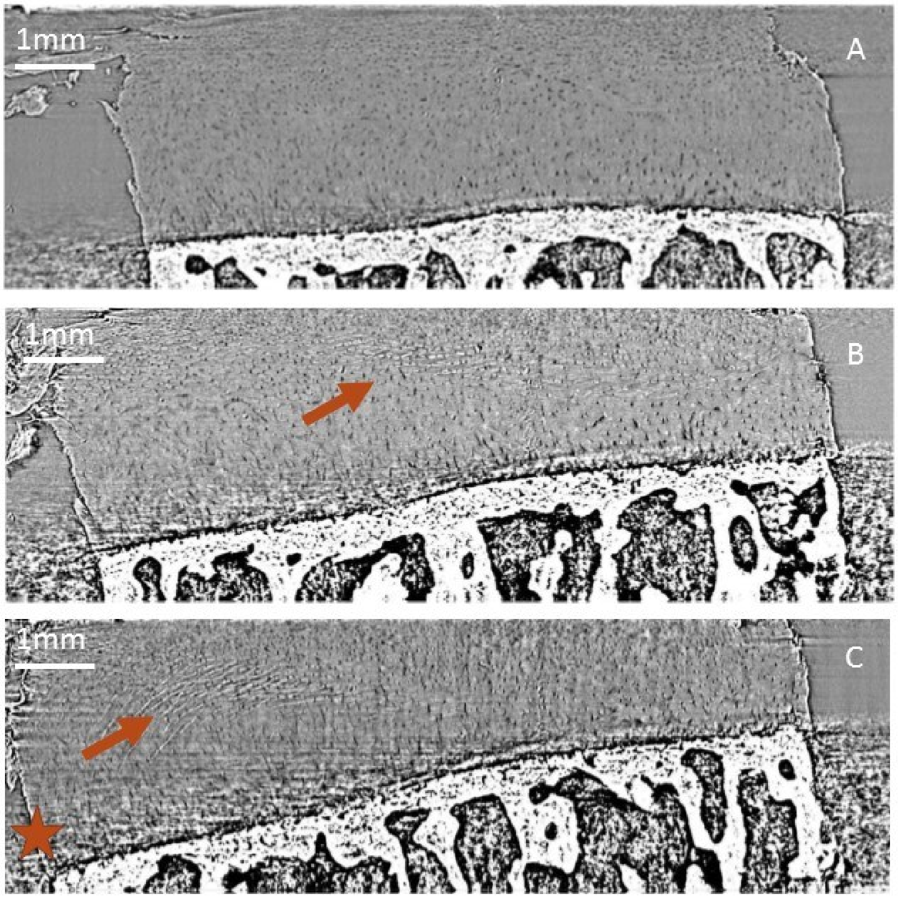

Figure 5.10 sagittal views of sample 2; red arrows are indicating the compression zones. A) cartilage plug without pressure B) cartilage plug with 9 N pressure C) cartilage plug with 30 N pressure the horizontal lines indicated by the star are artifacts coming from the bone.

5.4.2. 3D data rendering

A 3D and 'Z-projection' rendering of the different PCI-CT datasets was performed to visualize better and evaluate the measured data. A 3D representation of an entire cartilage plug (which has a diameter of about 1400 pixels (7 mm)) is too big to handle. Therefore a sub-volume corresponding to a cylinder with its axis parallel to the normal to the cartilage surface and with a diameter of 50 pixels (25 microns). Within this cylinder, the entire height of cartilage tissue with the different zones is visualized. Another way to display 3D images easily in 2D is with the Z-projection. This method projects 3D data into 2D data, where the third dimension (Z-dimension) is projected (summed) onto an X-Y- plane. In the images in Figure 5.11, there are 200 slices reduced into one slice.

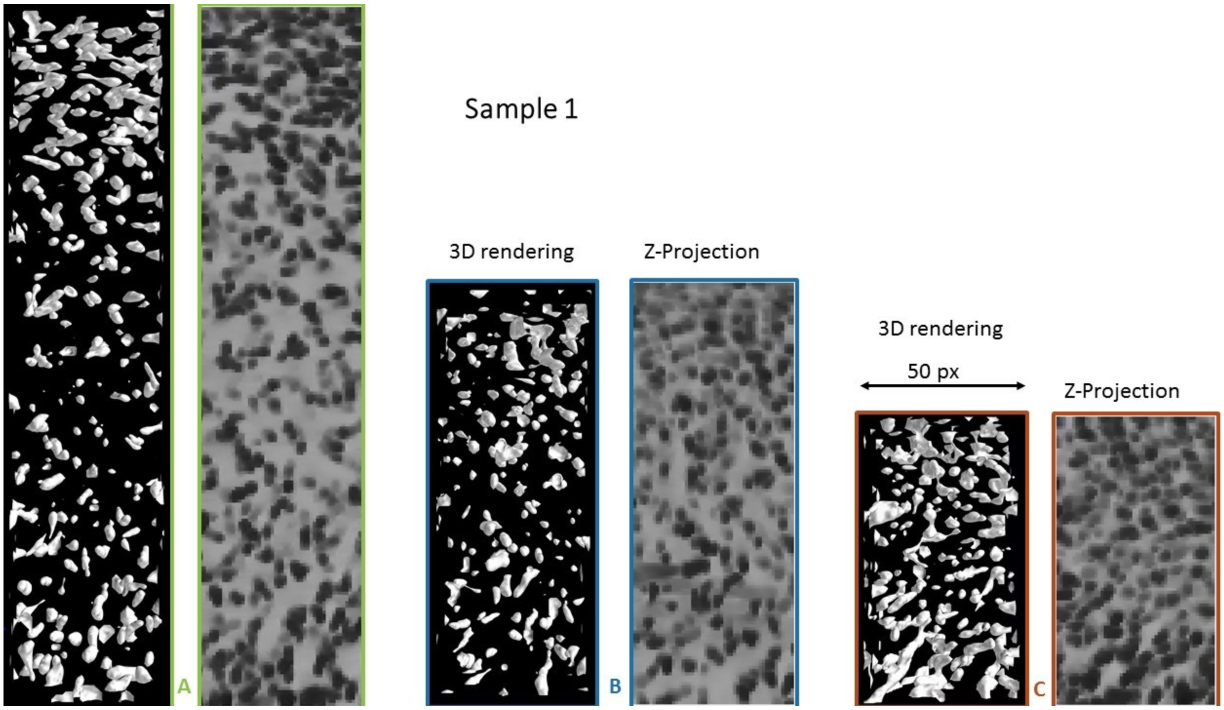

Figure 5.11 3D - rendering and Z-projection of the datasets of a non-degenerated cartilage sample (sample 1): A cylinder of 50 pixels diameter from the middle of the sample is chosen for the 3D rendering of the datasets acquired at the different pressures. A) Pressure point 1: no pressure. B) Pressure point 2: 54 N. C) Pressure point 3: 82 N.

With the 3D and Z-projection rendering shown in Figure 5.11A, it is possible to interpret better the results presented in Figure 5.14 on the cell orientation. In the top region of this volume (A), chondrocytes are mainly horizontally oriented, while in the bottom part of the sample, chondrocytes/chondrons are more vertical. If this is compared with images in Figure 5.11C, the orientation of the chondrons is not well defined as in Figure 5.11A. This can also be seen in the histograms in the upper row of Figure 5.14, where the orientation/angle between the different heights in the sample is not much changing. Another aspect that is well visible in this 3D representation is that the segmentation of chondrons corresponding to pressure point 3 is not easy because cells are closer and more difficult to distinguish and separate. Therefore, this can lead to an overestimation of the mean volume of the chondron (see Figure 5.13 top upper row).

5.4.3. Quantitative study

The quantitative analysis for quantifying the structure of the cartilage cells has been performed by using the procedure described in section 5.3.4 - 5.3.6.

To improve the methodology's accuracy, the analysis has been performed on sub-volumes obtained by dividing the cartilage into ten discs with the same height. This allowed studying the behavior of the different cartilage zones independently. This sampling is shown on a sagittal slice in e A).

In the following, the results for some of the selected samples from the examined groups are reported.

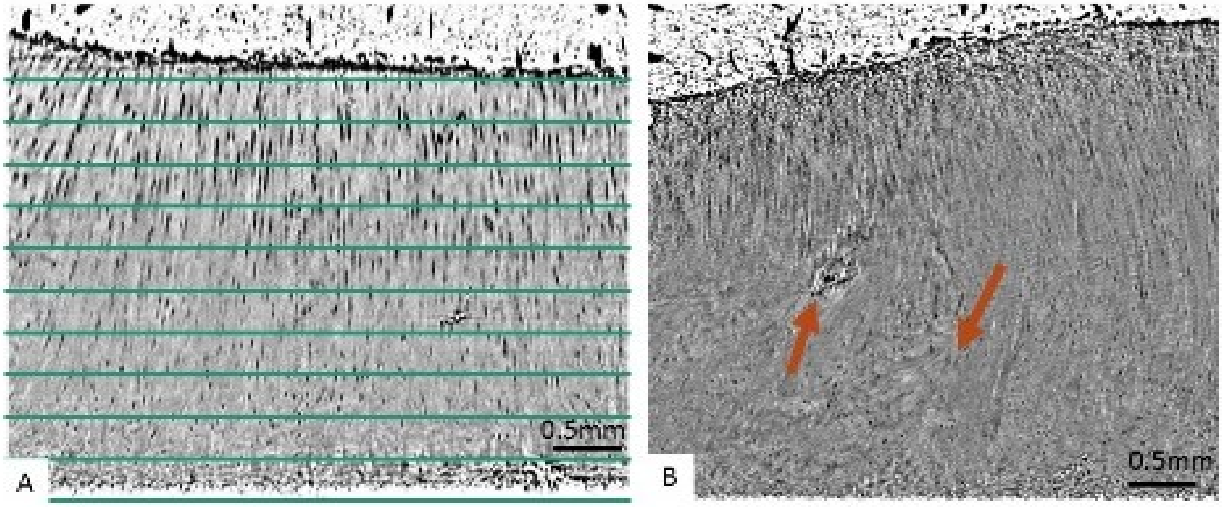

Figure 5.12 A) Sagittal slice of a non-degenerated sample with ten equidistant sections, to get a proper subsampling of the cartilage in the vertical direction. B) sagittal slice of a degenerated sample; arrows indicating degeneration signs in the sample.

The image in Figure 5.12 B shows a sagittal slice of the degenerated sample with signs of it indicated by the red arrows.

5.4.3.1. Non-degenerated cartilage

In Figure 5.13, the histograms of the mean chondrocyte volume and of the number of chondrocytes/chondrons for each of the ten vertical segments in which the cartilage tissue is divided are presented for a healthy (non-degenerated) (i.e., sample 1) and osteochondral plug (i.e., sample 10). Data are reported for three different levels of the applied pressure, and the bar error for each value (i.e., standard deviation) is also included. The most left bar (bar number 1) in the histogram represents the vertical section, which is close to the cartilage's surface, whereas the rightest bar (bar number 10) is the one close to the bone. The three pressure conditions correspond to applied forces of 0 N (1), 54 N (2) and 82 N (3), respectively.

For pressure 1, bar segments 1-2-3 (superficial layers) have almost the same mean cell volume as bar segments 8-9-10 (close to the bone). When increasing the applied pressure, the mean cell volume of the first six segments decreases, whereas the values do not change in the last four segments or rise like pressure 3.

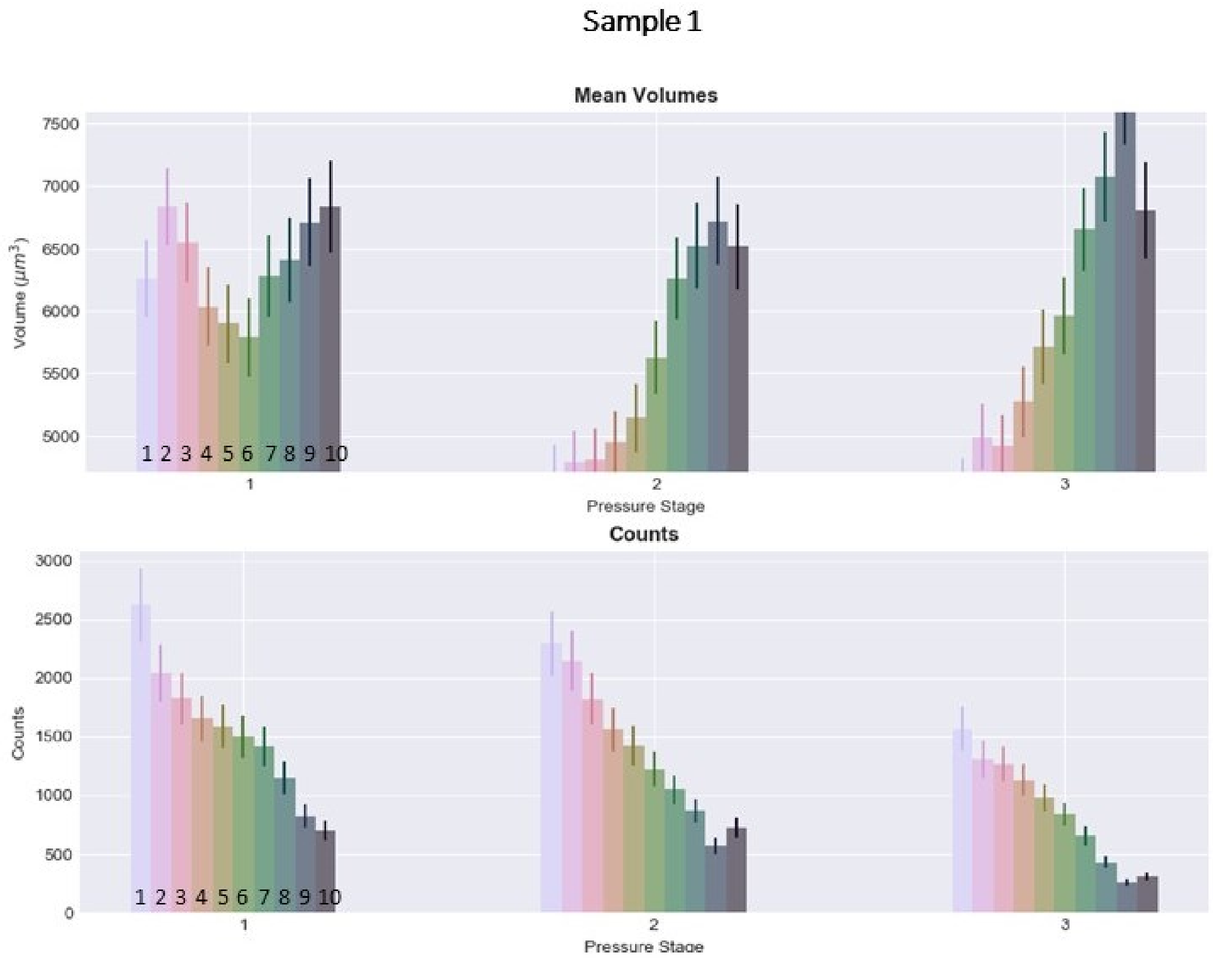

Figure 5.13 Histograms for a non-degenerated osteochondral plug (sample 1) of the mean cell volumes and cell number within each of the ten vertical segments of the cartilage (see figure 1.11) for three different applied pressures (1: 0 N, 2: 54 N; 3: 82 N).

The highest number of cells/chondrocytes is observed in the first bar segments at rest and compression conditions. Beyond this region, the value monotonically decreases. For pressure 3, the trend is the same, but the average number of cells in all segments is lower than pressures 1 and 2.

Figure 5.14 shows that the histograms for the mean angle and mean standard deviation distance to the surface are shown for the same sample. The angle of 90 degrees corresponds to cells with their axis parallel to the cartilage's surface (i.e., the cell axis is perpendicular to the surface's normal vector). The angle of 0 degrees corresponds to cases where cells are oriented perpendicularly to the surface (i.e., cell axes parallel to the surface's normal vector). For segment one at rest (pressure point 1), a mean angle of 70^o has been calculated. The mean angle decreases in the following segments: the mean angles calculated in segments 9 and 10 are 48^o and 50^o, respectively. This is different for pressure points 2 and 3. For point 2, the mean angle stays around 57^o for segments 1 to 5 and decreases between segments 6 to 9 to 47^o. The last segment has a larger mean angle than the second segment with 54^o. In the third pressure stage, the mean angle is around 60^o for all segments of the cartilage.

Concerning the mean standard deviation distance to the surface, one can observe that for pressure point 3, the mean values are higher for all segments with respect to the values obtained for pressure point 3.

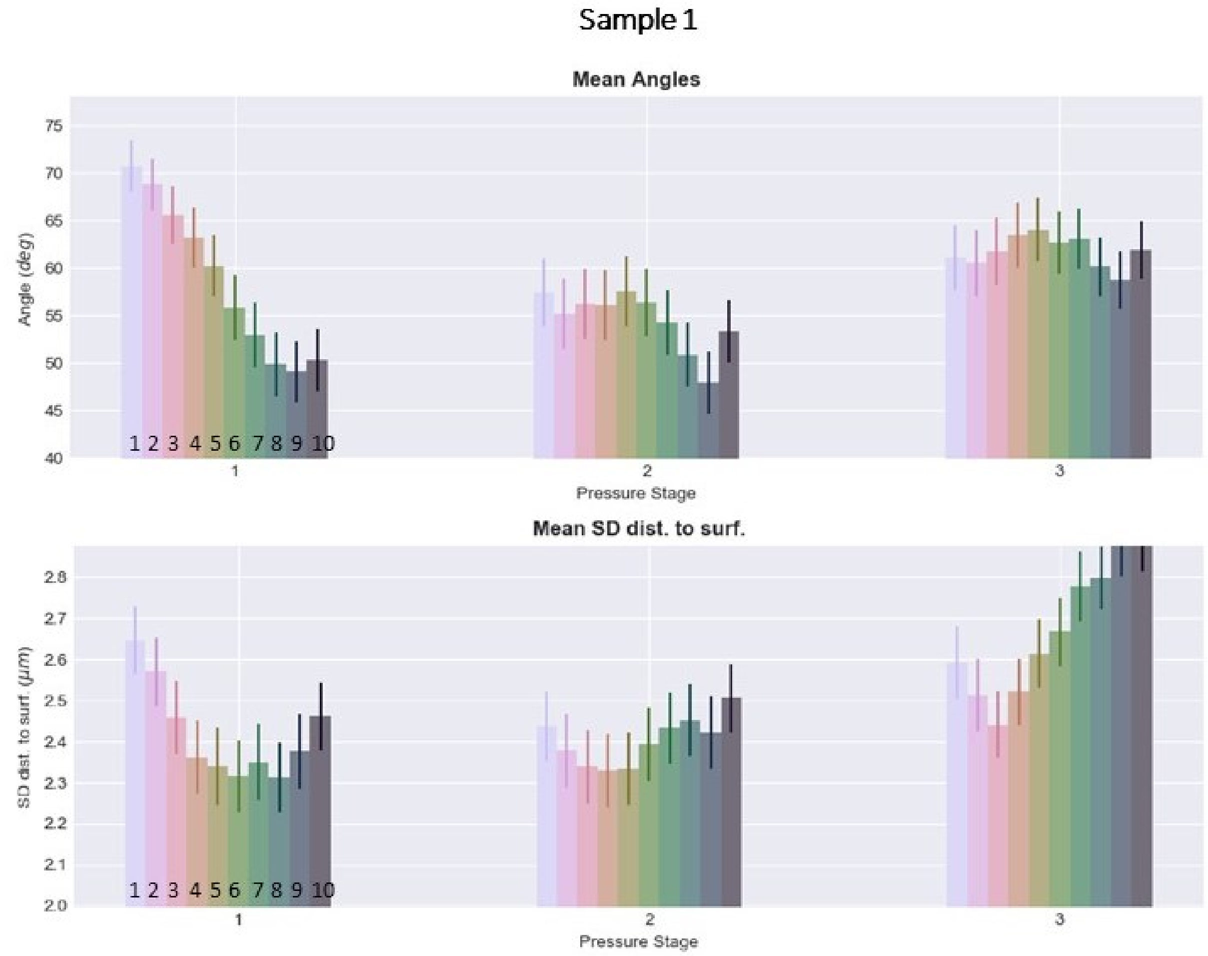

Figure 5.14 Histograms of the mean angle and the mean standard deviation distance to the surface for a non-degenerated cartilage specimen (sample 1).

5.4.3.2. Degenerated cartilage (sample 10)

In this paragraph, the quantitative analysis results on a degenerated osteochondral plug (sample 10) are reported (Figure 5.15). The forces applied to this specimen were 0 N (pressure point 1), 14 N (pressure point 2) and 24 N (pressure point 3).

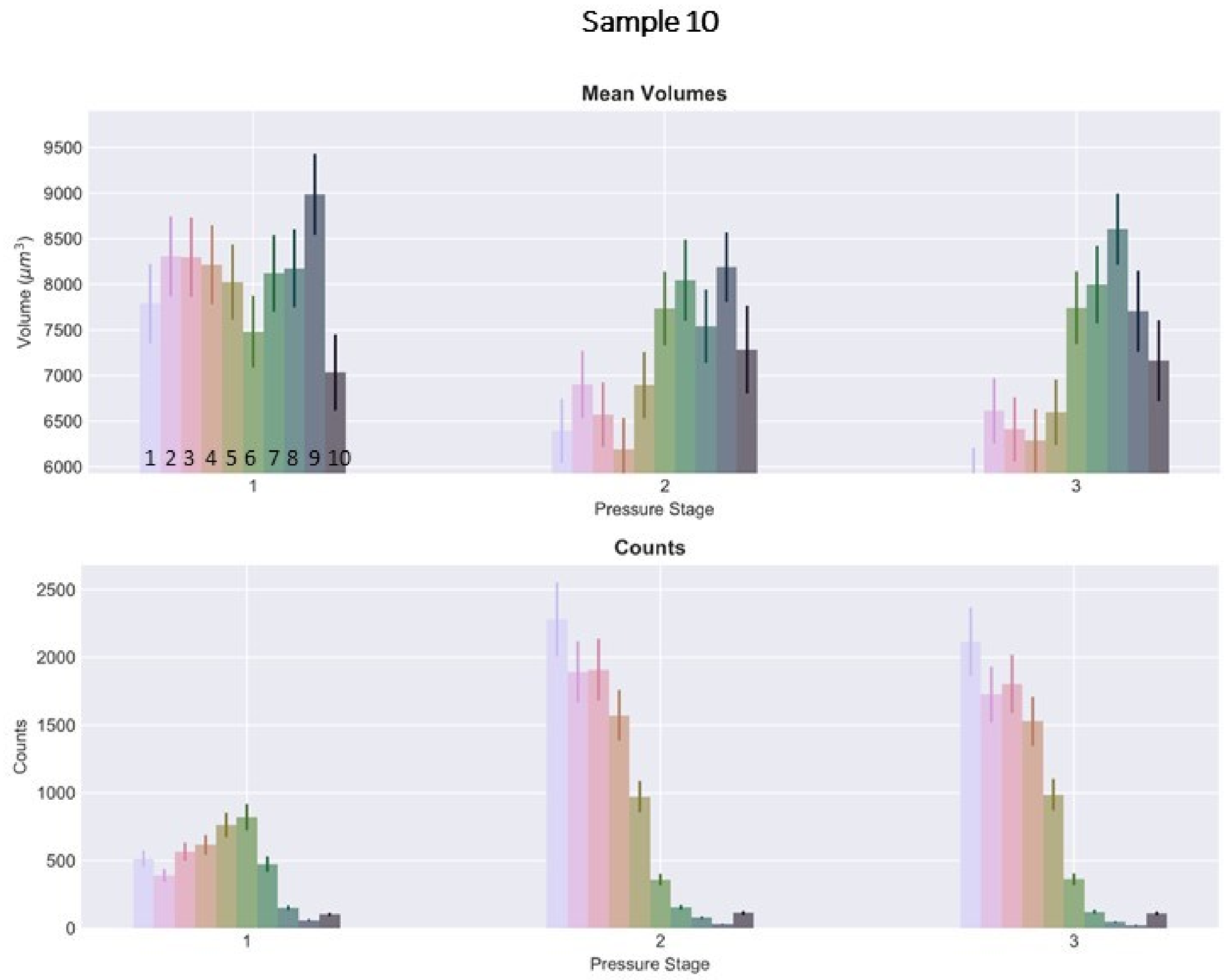

Figure 5.15 Histograms of the mean volume (upper row) and of the number of chondrocytes/chondrons in the different segments in which the cartilage has been divided for the three applied pressures for a degenerated cartilage sample (sample 10).

The histograms of the mean volume for pressure point 1 show that the calculated values are around 8000 µm^3 for all segments except for the 10th and 6th, where the volumes are smaller. In the histograms for pressure points 2 and 3, the first five segments show a significantly smaller volume size of the chondrons with respect to segments 6 to 10. Regarding the number of chondrocytes/chondrons, pressure points 2 and 3 show an increased number of chondrons in the first five segments than pressure point 1.

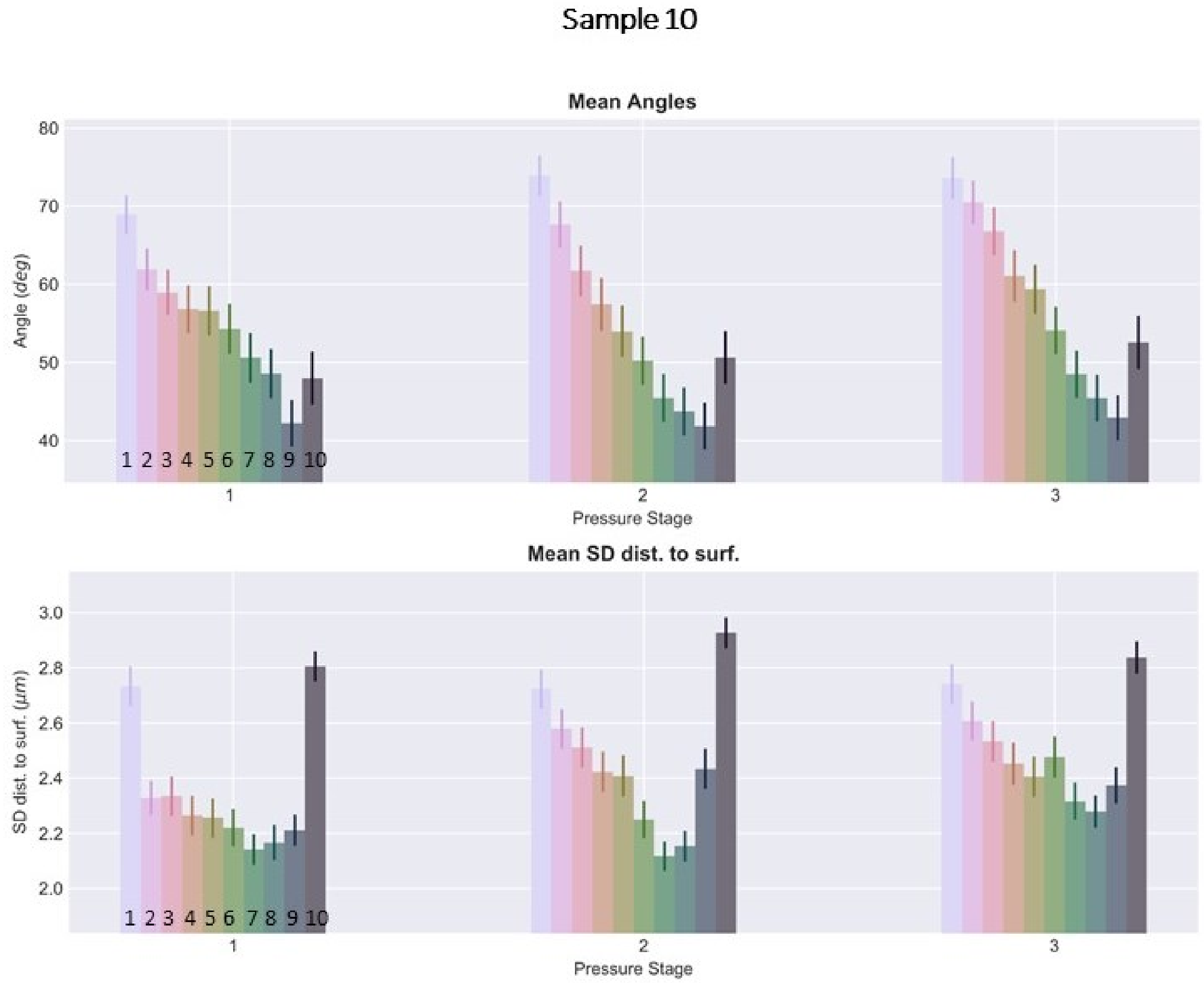

Figure 5.16 Histograms of the mean angle and the mean standard deviation distance to the surface for a non-degenerated cartilage specimen (sample 10)

The variation of the cell orientation, i.e., of the cells' mean angle with respect to the normal of the cartilage surface, has a very similar trend for the three pressure points. By increasing the pressure, the mean angle decreases monotonically up to segment 9, there is a little increase in the last segment, the one closest to the bone.

The mean standard deviation distance to the surface histograms is similar for the three pressure points. The first and the last segment present the highest values, whereas the values in the segments. The value decreases from segment 2 to segment 7. The last segment is always characterized by values significantly higher than the ones in segment 9.

5.4.4. Cell volume density

All the measurements in Paragraph 5.4.3 are absolute numbers like the number of chondrons in the sample, the mean volume or the angle distribution. In this paragraph, I present the result of calculating the volume density distribution, which is the total volume of chondrocytes/chondrons in relation to the tissue volume for the different applied pressures. The results for all specimens are grouped into two categories: samples without signs of degeneration (Figure 5.17) and degenerated samples (Figure 5.18). In the tables below, the volume density results in the percent of every vertical segment are listed. In brackets, the standard deviation is reported.

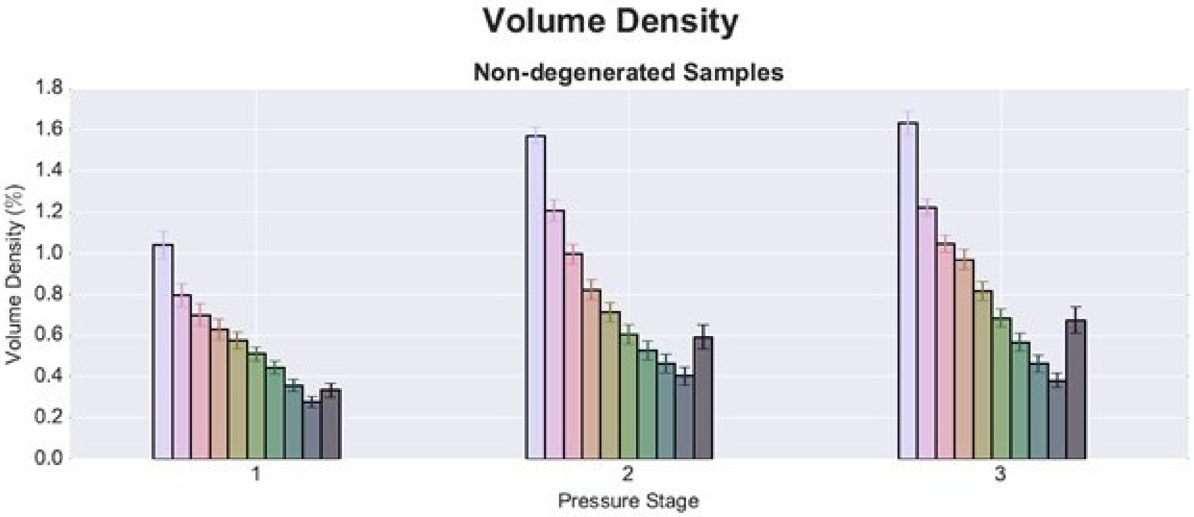

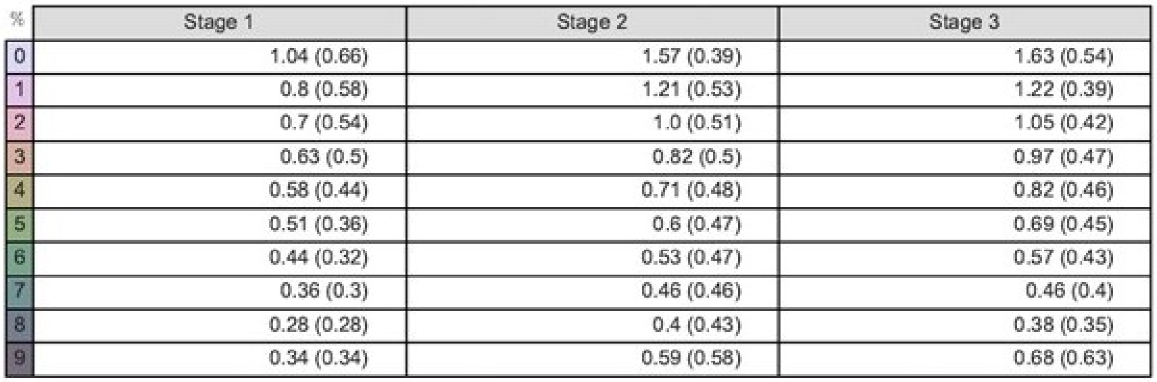

%	Stage 1	Stage 2	Stage 3
0	1.04 (0.66)	1.57 (0.39)	1.63 (0.54)
1	0.8 (0.58)	1.21 (0.53)	1.22 (0.39)
2	0.7 (0.54)	1.0 (0.51)	1.05 (0.42)
3	0.63 (0.5)	0.82 (0.5)	0.97 (0.47)
4	0.58 (0.44)	0.71 (0.48)	0.82 (0.46)
5	0.51 (0.36)	0.6 (0.47)	0.69 (0.45)
6	0.44 (0.32)	0.53 (0.47)	0.57 (0.43)
7	0.36 (0.3)	0.46 (0.46)	0.46 (0.4)
8	0.28 (0.28)	0.4 (0.43)	0.38 (0.35)
9	0.34 (0.34)	0.59 (0.58)	0.68 (0.63)

AVG 0.56%	AVG 0.79 %	AVG 0.84 %

TOTAL AVG 0.73 %

Figure 5.17 Cell volume density of degenerated and samples for every horizontal segment.

These results show that, when applying pressure on the cartilage tissue, the cell volume density becomes higher in all samples. The overall distribution among the different segments is very similar. In the upper segments, the cell volume density is the highest, and then it decreases up to segment 9. Segment 10, close to the bone, always has a higher cell volume density than segment 9.

The average cell volume density (overall the segments) rose from 0.25 % up to 0.56 % for the degenerated samples. In contrast, for the non-degenerated samples, the average rose from 0.56 % up to 0.84%, going from pressure point 1 to pressure point 3. We see, therefore, in our datasets a difference between the degenerated and non-degenerated samples, the average of the cell volume values is higher in the non-degenerated samples than in the degenerated ones.

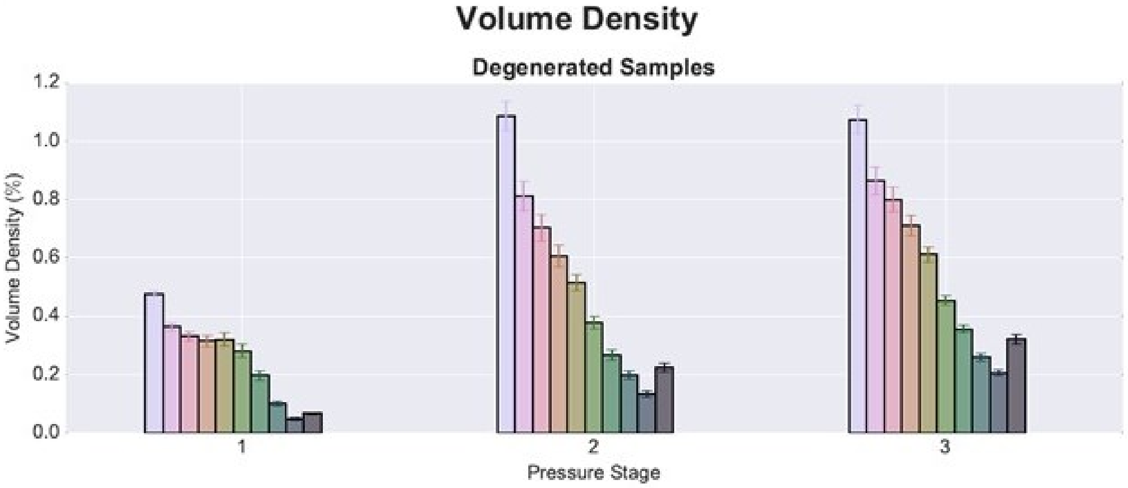

%	Stage 1	Stage 2	Stage 3
0	0.48 (0.09)	1.09 (0.5)	1.07 (0.5)
1	0.36 (0.13)	0.81 (0.5)	0.86 (0.47)
2	0.33 (0.17)	0.7 (0.46)	0.8 (0.44)
3	0.31 (0.2)	0.61 (0.37)	0.71 (0.35)
4	0.32 (0.24)	0.51 (0.28)	0.61 (0.25)
5	0.28 (0.23)	0.38 (0.21)	0.45 (0.16)
6	0.2 (0.15)	0.27 (0.18)	0.36 (0.14)
7	0.1 (0.07)	0.2 (0.15)	0.26 (0.13)
8	0.05 (0.03)	0.13 (0.12)	0.21 (0.11)
9	0.07 (0.03)	0.22 (0.15)	0.32 (0.15)

AVG 0.25 % AVG 0.49 % AVG 0.56 %

TOTAL AVG 0.43 %

Figure 5.18 Cell volume density of degenerated and samples for every horizontal segment.

5.5. Discussion

Phase-contrast imaging – Computed tomography provides 3D visualization of the interterritorial matrix and the cells within articular cartilage, thanks to its sensitivity towards soft tissue. The images show chondrocytes and chondrons, but no details about the cellular structures (i.e., cell nucleus) are revealed. Another detail that is detected, that these images cannot depict the difference between territorial and interterritorial matrix. The pixel size is set to allow for a large field of view (including the full sample laterally) and to detect and visualize the cartilage cells. The high contrast and the 3D possibility offered by this method allow us to visualize/segment cells and locate them within the examined volume precisely. With this, a quantification of the cell structure is possible. This analysis has been done on two samples that are classified as non-degenerate (e.g., sample 1) and degenerated (e.g., sample 10). The aim was to demonstrate the development and the optimization for the workflow to perform it on a larger sample set, to have more statistically significant results. When applying pressure on the plugs, a reduction of the mean cell volume can be observed in the first five segments for both samples. Thus, the articular cartilage is more compressed in the superficial zone (first segments) than in the middle or deep zone, and so are the chondrocytes/chondrons. This result confirms previous observations reported in the literature in 2007 by Choi et al. on zonal changes in the three-dimensional morphology of the chondron under compression (Choi, Youn et al. 2007).

The difference between this experiment and Choi et al. is that we analyzed a much larger volume. Our samples had a diameter of 7 mm compared to the 40µm thickness of the block. And the cartilage was is in a more "natural state" in saline solution than in the Choi et al. experiment (paraformaldehyde). Choi et al. also showed that the chondrocytes/chondrons in the middle and deep-zone slightly reduce their size. In contrast, Choi et al., these experiments show that, in sample 1, the chondrons of the deep zone are increased in volume. This might be caused by the fact that chondrons are so close that the segmentation algorithm cannot separate them. Therefore the volume size is overestimated in this analysis. In Figure 5.11 C, the cells in the lower part of the cartilage (close to the bone) form a long cluster, make them look like one single object. The single cell in that cluster cannot be separated from the resolution used in this experiment. The clustering of chondrocytes/chondrons under pressure conditions also explains the reduction of the number of cells counted by the applied algorithm (for example, Figure 5.13, for sample 1).

The analysis of the cell orientation for sample 1 shows a change in the direction of the chondrocytes/chondrons when different pressures are applied. In the first segment, the mean angular value changes from 70^{o} at rest to 60^{o} for pressure point 3 (82 N), while there is no significant variation visible deeper in the tissue, i.e., in segment 10. Therefore, cartilage compression affects the way cells are oriented within the different layers of the cartilage matrix. The compression changes the direction of the chondrocytes/chondrons and the shape of the chondrons, which is measured with the mean standard deviation distance to the surface. In sample 1, this changes quantitatively when pressure is applied and the mean standard deviation distance to the surface increases (this means that the cells have a round shape).

Not all samples behaved the same way as sample 1; this made it hard to conclude a general behavior for non-degenerate cartilage samples. Also, within the degenerated group, a common trend is challenging to be identified. For example, in sample 10, when applying pressure, the average cell volume is reduced in the superficial and upper-middle zone, and the number of chondrons in these zones rises, as shown in Figure 5.15. In this specimen, the segmentation of the chondrons worked better in the datasets collected for pressure points 2 and 3: cells were more accessible to be segmented, leading to a reduced false clustering (more single cells identified) thus to a more precise cell volume evaluation.

There are several limitations to this experiment to be discussed. The detector's pixel size was 5.1 µm, the size of a chondron varies from 15 -35 µm. Therefore a chondron is about 3 to 7 pixels large in the reconstructed images. Therefore, if the segmentation algorithm is off by 1 or 2 pixels, the length in 2D or the volume in 3D and the angle differs from the "real" length or volume. Another issue with this experiment is that the imaged cartilage plugs' height varies from sample to sample. The displacement of the piston of the tomopress device was always the same. Therefore, the force measured by the pressure plate was different for the different samples as well as the elasticity of the cartilage plugs. Another issue was that the cartilage tissue, which is softer than the bony part, could expand to the sides when applying pressure because the tube's diameter surrounding them was bigger than the sample diameter (7 mm). It is difficult to draw general conclusions because the natural variability is large and the force application method could not be adapted case by case depending on the plug dimension.

The estimation of the cell volume density of the chondrocytes/chondrons shows a significant difference between the non-degenerated and degenerated cartilage groups. The cell volume density in the non-degenerated samples was greater than in degenerated samples, within the estimated errors for all pressure points. The degenerated specimens have an average volume density of 0.43 %, with respect to the total volume of the tissue in which the estimation was performed. In comparison, for the non-degenerated group, we calculated 0.73%. The volume density of cartilage was also measured in previous works by Hunziker, Quinn et al. using 100 µm thick-sliced sections and confocal light microscopy. They found a volume density of chondrons in the cartilage of 1.65 % (Hunziker, Quinn et al. 2002), but this reported value estimates the volume based on the 2D measurement. For comparison, in this experiment, the volume and volume density is measured directly from a 3-dimensional dataset and is not indirectly estimated. By comparing the non-degenerated samples at different pressure points, the average cell volume density increases by a factor of 1.5 (1.41) for high (medium) applied pressure. In comparison, the degenerated sample has an increase of cell volume density by a factor of 2.25 (1.96) for high (medium) pressure. This shows how cartilage gets more compressed and effective when it is in a degenerated state.

5.6. Conclusions

This experiment and quantitative study give an interesting insight into the cartilage structure and its resident cells' behavior at rest and in pressure conditions. The most challenging part has been the analysis and the interpretation of the data because of the sample variance and preservation conditions (samples underwent a long preservation period). In this study, the number of granted synchrotron beamtime shifts allowed examining 13 samples. This work is a proof of principle study: we have been the first to use the tomopress device for dynamic cartilage experiments and apply the described methodology for the extraction of quantitative information on the behavior of the articular cartilage tissue and its cells. The quantitative information shows how the different cartilage layers are affected under pressure and that there are differences between non-degenerated and degenerated cartilage.

Despite the difficulties encountered in the work's mechanical and image processing phases, we were able to confirm some of the results already reported in the literature, but with a more accurate approach using a volumetric method.

One of the experiment's main limitations is the spatial resolution employed, which made the segmentation difficult and prone to errors. Therefore, in order to confirm and improve the significance of the results, the experiment should be repeated using higher spatial resolution (i.e., a detector with a smaller pixel size) to get a more detailed visualization of the cells. I would suggest a pixel size between 0.5 and 1 µm.

This work's main purpose was to establish an imaging methodology allowing for a 3D imaging-based quantitative analysis of cartilage samples down to cell level. With this respect, a full analysis pipeline for the characterization of chondrocytes/chondrons based on 3D phase-contrast imaging was successfully tested and implemented.

Bibliography

Agneskirchner, J., C. Hurschler, C. Stukenborg-Colsman, A. Imhoff and P. Lobenhoffer (2004). "Effect of high tibial flexion osteotomy on cartilage pressure and joint kinematics: a biomechanical study in human cadaveric knees." Archives of orthopaedic and trauma surgery **124**(9): 575-584.

Agneskirchner, J. D., C. Hurschler, C. D. Wrann and P. Lobenhoffer (2007). "The effects of valgus medial opening wedge high tibial osteotomy on articular cartilage pressure of the knee: a biomechanical study." Arthroscopy **23**(8): 852-861.

Arganda-Carreras, I., V. Kaynig, C. Rueden, K. W. Eliceiri, J. Schindelin, A. Cardona and H. Sebastian Seung (2017). "Trainable Weka Segmentation: a machine learning tool for microscopy pixel classification." Bioinformatics **33**(15): 2424-2426.

Bleuet, P., J.-P. Roux, Y. Dabin and G. Boivin (2004). In situ microtomography study of human bones under strain with synchrotron radiation. Developments in X-Ray Tomography IV, International Society for Optics and Photonics.

Chambolle, A. (2004). "An algorithm for total variation minimization and applications." Journal of Mathematical imaging and vision **20**(1-2): 89-97.

Choi, J. B., I. Youn, L. Cao, H. A. Leddy, C. L. Gilchrist, L. A. Setton and F. Guilak (2007). "Zonal changes in the three-dimensional morphology of the chondron under compression: the relationship among cellular, pericellular, and extracellular deformation in articular cartilage." Journal of biomechanics **40**(12): 2596-2603.

Corezzi, S., L. Urbanelli, P. Cloetens, C. Emiliani, L. Helfen, S. Bohic, F. Elisei and D. Fioretto (2009). "Synchrotron-based X-ray fluorescence imaging of human cells labeled with CdSe quantum dots." Anal Biochem **388**(1): 33-39.

Fisher, R., S. Perkins, A. Walker and E. Wolfart (2003). "Contrast stretching." Online]. http://homepages. inf. ed. ac. uk/rbf/HIPR2/stretch. htm.

Glitsch, U., N. Lundershausen, D. Knieps, A. Johannknecht and R. Ellegast (2009). Biomechanische Analyse der Kniegelenkbelastung bei Tätigkeiten im Hocken und Knien 49. Jahrestagung der Deutsche Gesellschaft für Arbeitsmedizin und Umweltmedizin. Aachen. **49**.

Gründer, W., M. Kanowski, M. Wagner and A. Werner (2000). "Visualization of pressure distribution within loaded joint cartilage by application of angle-sensitive NMR microscopy." Magnetic Resonance in Medicine **43**(6): 884-891.

Ho, T. K. (1995). Random decision forests. Proceedings of 3rd international conference on document analysis and recognition, IEEE.

Hunziker, E., T. Quinn and H.-J. Häuselmann (2002). "Quantitative structural organization of normal adult human articular cartilage." Osteoarthritis and Cartilage **10**(7): 564-572.

Kamiński, B., M. Jakubczyk and P. Szufel (2018). "A framework for sensitivity analysis of decision trees." Central European journal of operations research **26**(1): 135-159.

Lee Koh, J., A. Kowalski and E. Lautenschlager (2006). "The effect of angled osteochondral grafting on contact pressure: a biomechanical study." The American journal of sports medicine **34**(1): 116-119.

Maki, K., N. Inou, A. Takanishi and A. Miller (2003). "Computer-assisted simulations in orthodontic diagnosis and the application of a new cone beam X-ray computed tomography." Orthodontics & craniofacial research **6**: 95-101.

Mirone, A., E. Brun, E. Gouillart, P. Tafforeau and J. Kieffer (2014). "The PyHST2 hybrid distributed code for high speed tomographic reconstruction with iterative reconstruction and a priori knowledge capabilities." Nuclear Instruments and Methods in Physics Research Section B: Beam Interactions with Materials and Atoms **324**: 41-48.

Mononen, M., M. Mikkola, P. Julkunen, R. Ojala, M. Nieminen, J. Jurvelin and R. Korhonen (2012). "Effect of superficial collagen patterns and fibrillation of femoral articular cartilage on knee joint mechanics—a 3D finite element analysis." Journal of biomechanics **45**(3): 579-587.

Rack, A., J. Stroebel, T. Rack, Y. Dabin, C. Knabe, M. Stiller, P. Coan and P. Bleuet (2020). "TomoPress—In Situ Synchrotron-Based Microtomography under Axial Load." Instruments **4**(2): 11.

Rudin, L. I., S. Osher and E. Fatemi (1992). "Nonlinear total variation based noise removal algorithms." Physica D: nonlinear phenomena **60**(1-4): 259-268.

Witten, I. H., E. Frank, M. A. Hall and C. J. Pal (2016). Data Mining: Practical machine learning tools and techniques, Morgan Kaufmann.

6. Automatic Analysis and Convolutional Neural Networks

This chapter presents a work in which convolutional neural networks (CNNs) are applied to X-ray phase-contrast images for an automatic data analysis and diagnosis. This project's objective was to test and compare the performance of three different CNN systems in terms of their capability in discriminating different stages of cartilage and liver diseases using input datasets images acquired by highly sensitive PCI methods. The goal is to identify the optimal approach and settings to establish a procedure for OA and liver data classification that is time-effective, observer-independent, and more accurate than what is already reported in the literature. This chapter's result is condensed in the paper "Convolutional Neuronal Networks combined with X-ray Phase-contrast Imaging for an improved, fast and observer-independent discrimination of cartilage and liver diseases stages" which has been published in the Scientific Reports journal (Stroebel, Horng et al. 2020).

6.1. Introduction

The analysis and classification of radiological images are highly time-consuming and require trained observers. In the X-ray domain, biological tissues and their pathology-induced modifications can have very similar attenuation properties. Thus their discrimination can be very difficult or, in some cases, impossible. Early stages of a disease, characterized by tiny signs and structures, have to be visualized when a new treatment is being studied; this requires the availability of highly sensitive imaging methods and high spatial resolution images. The standard reference in clinical pathology is the histological examination; however, this is an invasive procedure and can provide only a 2D vision of a small portion of tissue.

Additionally, the diagnosis relies on skilled operators both on the realization of tissue sampling and in the histological exam. Previous works have shown that PCI enables the depiction of different stages of articular cartilage degradation (i.e., OA) (Mollenhauer, Aurich et al. 2002, Wagner, Aurich et al. 2005, Li, Zhong et al. 2009, Coan, Bamberg et al. 2010, Lee, Heo et al. 2010, Muehleman, Fogarty et al. 2010, Marenzana, Hagen et al. 2012) and liver fibrosis in a rat animal model (Zhang, Yang et al. 2013, Brandlhuber, Armbruster et al. 2016). In those studies, images were evaluated and classified by experienced radiologists. As already explained in chapter one, osteoarthritis is a degenerative disease, where the cartilage wears up over time (Zhang 2015), leading to mobility problems and pain (Felson 1988). Liver fibrosis is the excessive accumulation of extracellular matrix proteins, including collagen, in most types of chronic liver diseases (Bataller and Brenner 2005). Conventional X-ray imaging techniques are sensitive only to advanced stages of these pathologies when therapeutic strategies are less effective.

Convolutional Neural Networks are new artificial neural systems, which offer a highly accurate and observer-independent classification of images (Krizhevsky, Sutskever et al. 2012). This is achieved through a two-step process: the network is first trained on a given dataset to let the algorithm learn how to classify the samples, and then it is applied to the dataset of interest; in this last step, the network works in a fully automated manner. As reported in the literature, CNNs have been successfully used in different fields, in object detection (Szegedy, Toshev et al. 2013) and face recognition (Hu, Yang et al. 2015). CNNs were, for the first time and successfully applied to PCI images by Abidin et al. (Abidin, Deng et al. 2018). These results have inspired us to test the CNN approach to different datasets: one of the cartilage images acquired at higher spatial resolution and by using a different PCI technique (the Propagation-based imaging) concerning what presented in the literature, and a second one including PCI images of liver fibrosis and fat liver.

6.2. Artificial Neural Networks

Artificial Neural Networks (ANNs) are computing systems inspired by the structure and functioning of biological neural networks, which "learn" to perform tasks from given input examples without being specifically programmed for the task. ANNs are a sub-category of the more general machine learning algorithms. The basic sub-unit of this system is an artificial neuron: it has an input value x_j, a weight value $w_{k,j}$, a threshold θ_k for the activation function F_k and an output value o_k.

$$o_k = F_k(s_k, \theta_k) \tag{6.1}$$

Where s_k is the input of the function obtained as the following sum:

$$s_k = \sum_i x_j\, w_{k,j} + b_k \tag{6.2}$$

With b_k the bias value, which helps for better adjusting of the network.

If the result is above the threshold, then the activation function gives an output that is a new input value for an artificial neuron in the next layer of the system. An ANN can consist of multiple layers with multiple artificial neurons in it (Vidushi Sharma 2012). In this work, the convolutional neural network was used, which is a special kind of ANN having four different types of layers: an input, a convolutional, a pooling, and a fully connected layer, which are represented in Figure 6.1.

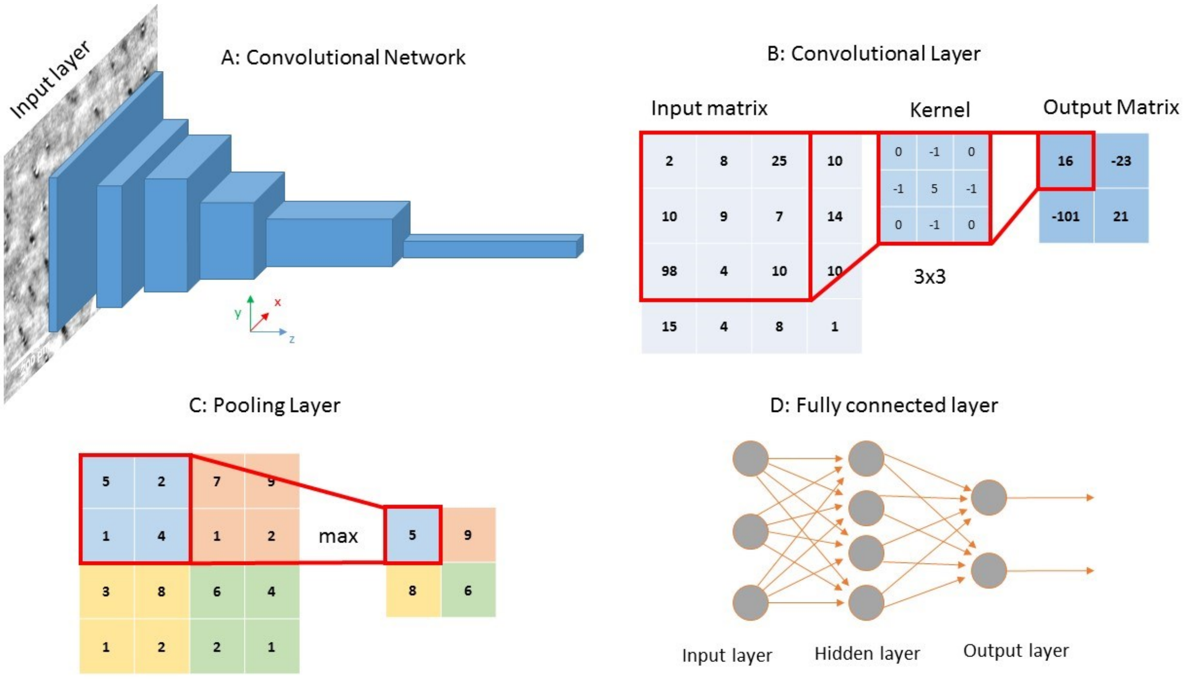

Figure 6.1 A) sketch of convolutional network design, with input and convolutional layers. The data reduction along the x and y directions depends on the kernel size and stride length, the extension along the z-direction is related to the number of kernels applied to the layer. B) Convolutional Layer, every pixel in the output matrix is calculated by a convolution of the input matrix and the kernel. C) The Pooling Layer reduces the matrix size by taking the maximum value of an area (2x2 pixels) as an output. C) Sketch of a fully connected layer: the hidden layer is connected with every node of the input and output layer.

The input layer takes the image that is given to the network to be analyzed. The convolutional layer has a kernel with trainable weights and a size that can vary: usual sizes are 3x3, 5x5 or 7x7 pixels. The input image is convoluted with the kernel, which acts, thus, as a filter. The pooling layer performs the downsampling of the input that depends on the kernel size and stride length (step of displacement after convolution). In this study, the so-called max-pooling layer is used: it takes the maximum value within the kernel as an input for the next layer. At the end of the network system, classification and activation functions are performed in the fully connected layer, where all artificial neurons are connected (Ciregan, Meier et al. 2012).

In the CNN language, one epoch is one iteration of the network. An epoch consists of two parts: the forward processing of images to classify them and the backpropagation to change/train the weights and converge towards an improved classification. In the forward processing, the image data go from the input layer to the classification layer. A function calculates the error between the predicted classification and the prior classification information (error function) by considering every weight's effect in the classification layer. To minimize the error, an optimizer (Ruder 2016) is used, which adjusts the weight according to the user's learning rate. Depending on the number of epochs and the learning rate, CNN converges and classifies the data. Therefore the learning rate is set to get the fastest convergence (as defined at the end of this section) and the best classification.

In this study, I used the so-called transfer learning method that works with CNN weights pre-trained on large image datasets. Our case weights were trained on the ImageNet dataset, a database of about 14 Million Images of 218141 synsets (groups of synonyms) with an average of 500 images per synset (Deng, Dong et al. 2009). I removed the classification layer of the pre-trained network and implemented a self-designed network procedure. This self-designed network has a fully connected layer and a classification layer with 2 or 4 outputs, depending on the dataset. The pre-trained CNN acts as a feature extractor for the self-designed part of the network. In the backpropagation, the weights are adjusted in the self-designed network, whereas the pre-trained network weights are fixed.

We tested three pre-trained CNNs for our study: the VGG16, the Inception V3, and the Xception Network. These three networks showed great capabilities in the classification of images in the Large Scale Visual Recognition Challenge (LSVRC) organized by the ImageNet project (Russakovsky, Deng et al. 2015). A dataset of 1.2 million images of 1000 synsets was chosen to be classified by ANNs or other Machine Learning algorithms in this challenge. The achieved accuracy in the challenge was 90.1 % for VGG16, 94.1% for the Inception V3 network and 94.5% for the Xception (Chollet 2016).

The VGG16 CNN is a network with 16 convolutional layers with a kernel size of 3x3 pixels. The size of the input images is 224 x 224 pixels (for RGB images). The max-pooling layer has a kernel of 2x2 pixels and a stride of 2 pixels. After the convolutional layers, there are two fully connected layers with 4096 connections (Figure 6.2). The last layer is the softmax classification layer with 1000 classification units. The softmax function is a normalized exponential function, giving a probability distribution. In the fully connected layer, the activation function is the rectified linear unit function (ReLU) (Simonyan and Zisserman 2014). The VGG16 is a heavy computation network, with long training times and many weights (for a total size of 533MB).

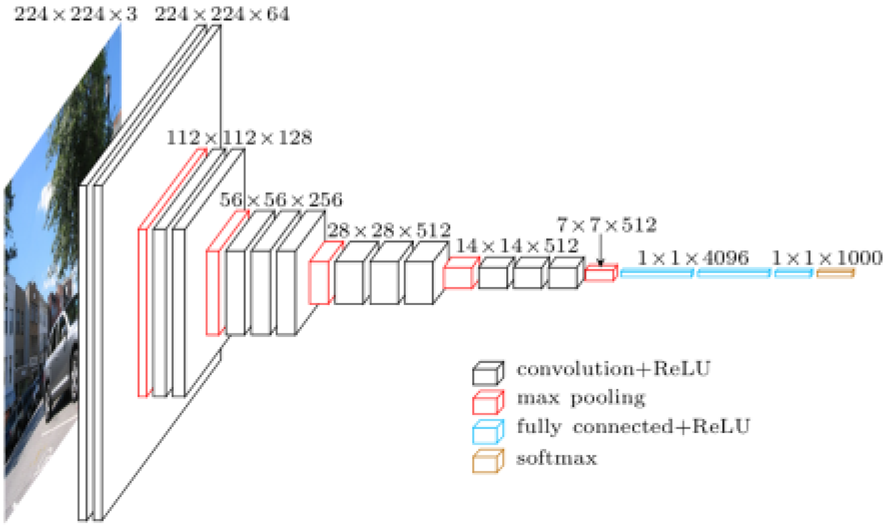

Figure 6.2 Schematic visualization of the VGG16 network structure (Cord 2016)

The Inception network was introduced by Szegedy et al. in 2014. The idea is to make the network "wider" instead of "deeper". There are multiple inception modules in one layer, with convolutional modules of different kernel sizes (1x1, 3x3 or 5x5 pixels) and a max-pooling or avg-pooling module. All these modules are then concatenated and sent to the next inception layer (Christian Szegedy 2014).

In version 2 of the Inception network, the factorization of the kernel is applied. Instead of having modules with kernels of 5x5 pixels, sets of two 3x3 pixels kernels are used. In version 3, which was used in this study, the module with a kernel of 7x7 pixels is replaced by three 3x3 pixels kernels. In this way, the pre-trained weights' size is reduced to 96 MB (Christian Szegedy 2015). This network's input is 299 x 299 x 3 pixels, and the output of the inception is 8x8x2048.

The Xception Network derives its name from "Extreme Inception" and brings the Inception concept to the next level. This architecture builds on a depth-wise separable convolutional layer. This means that mapping the cross channel correlations and spatial correlations in the so-called feature maps (output of convolutional layers) can be entirely decoupled. The weight size of this network is 91 MB (Chollet 2016).

The analysis was performed on a Fujitsu workstation with 8 Intel Xeon CPU processors with four kernels and 2.6 GHz. The graphics card on which the calculations were done is an NVIDIA Quadro P1000 with 4 GB of Memory and 640 Cuda cores. The entire code is written in Python with Keras(Chollet 2015), a deep learning library in Python interfacing TensorFlow-GPU as a backend (Abadi, Agarwal et al. 2016).

6.3. Sample description and methods

The cartilage samples were osteochondral plugs of cylindrical shape with a diameter of 7 mm extracted from a cadaveric human patella. The images of these plugs are presented in chapter four, in the multiscale study. The plugs were divided into two groups based on experienced pathologists' histological images: the control group with healthy cartilage samples and the OA degraded cartilage group. IRB was waived by the institutional review board of the Ludwig-Maximilians-University, Munich. The samples were imaged at the Biomedical beamline (ID17) of the ESRF by using X-ray propagation-based PCI micro-CT (Davis, Gao et al. 1995) polychromatic and filtered X-ray beam with peak energy around 40 keV. The detection system consisted of a PCO edge 5.5 sCMOS camera (Mittone, Manakov et al. 2017) coupled with 10x optics and a 19 µm thick GGG scintillator screen to a final pixel size of 0.7 x 0.7 µm^2.

The liver samples were extracted from rats that underwent a protocol based on Bile Duct Ligation (BDL) to induce liver fibrosis and fat livers (Brandlhuber, Armbruster et al. 2016). The liver samples were divided into three groups: healthy, fibrotic four weeks (BDL for four weeks) and fatty livers. The samples were all paraffin-preserved and imaged with X-ray PCI micro-CT with a polychromatic X-ray beam with a mean energy of 24 keV at the ID19 beamline ESRF. The detection system was a PCO Edge with a 6.5 µm pixel size and a 2.9 x MR optics, which has an effective pixel size of 2.2 x 2.2 µm^2.

Both CT datasets were reconstructed with the PyHST2 software (Mirone, Brun et al. 2014). For the cartilage data, sagittal images of 1024 x 1024 pixels were extracted from the reconstructed CT volumes' radial zone, binned to reduce them to 224 x 224 pixels to fit the CNN requirements and normalized to values in the range [0-1]. These are shown in Figure 6.3 A) and B): A) is a sagittal PCI-CT image of healthy cartilage tissue, whereas B) the sagittal slice of an osteoarthritic cartilage sample with a small crack of the tissue visible on the right side. 3802 images were extracted from every group and split into two categories: 60 % were used as training data, 20 % as validation data, and 20% as testing data.

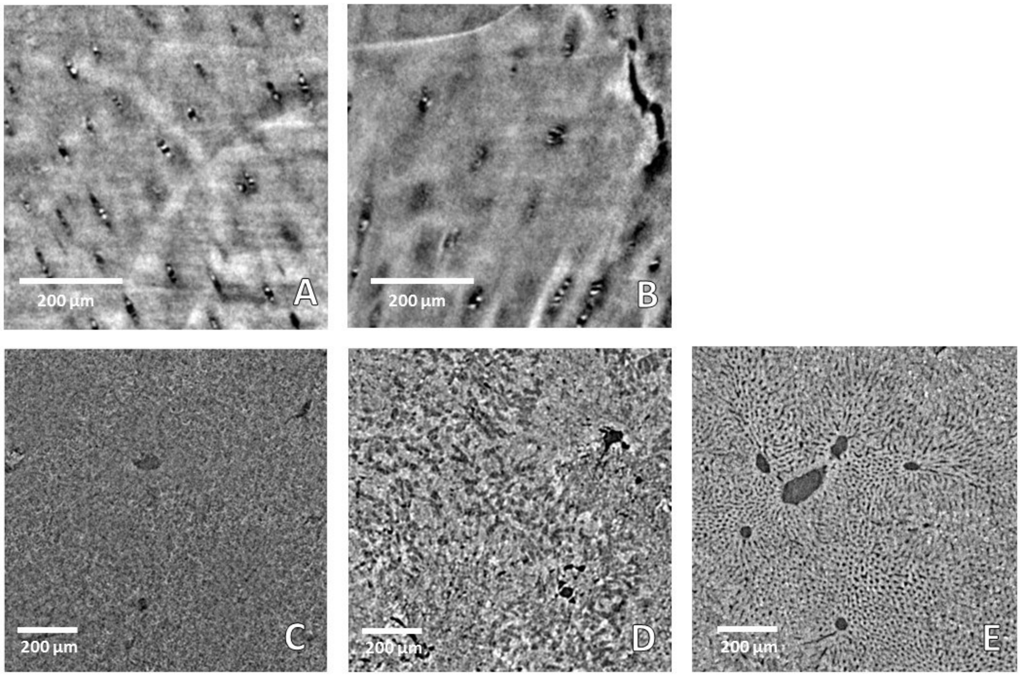

Figure 6.3 Examples of PCI micro CT images (224x224 pixels) used as input for the neural network's systems; A) and B): images acquired with a detector pixel size of 0.7 x 0.7 µm^2 of a healthy (A) and degenerated (B) cartilage specimen, respectively; C)-E): PCI images acquired at a final pixel size of 2.2 x 2.2 µm^2 of a healthy (C), D) fibrotic-4 weeks liver and E) fat liver, respectively. The scale bar indicates 200 µm.

The 512 x 512 pixels' liver images were extracted from 3D reconstructed volumes, normalized to the range [0-1] and reduced to 224 x 224 pixels by binning and linear interpolation. This dataset originates from 6 different liver samples: two healthy (Figure 2C), two fatty livers (Figure 2E) and two fibrotic four weeks (Figure 2D). A total of 3600 images were obtained, and, from each liver sample, 600 images were extracted. By applying again, a 60/20/20 split ratio, 2160 images were used for training the network, 720 for validation during the training and 720 images were used for testing the trained network. Besides, the total number of input images for training and testing was increased by rotating the original images by 90, 180 and 270 degrees and adding them to the respective groups of images. This method is referred to as "data augmentation" and it increased the total number of available images by a factor of four in this case (Van Dyk and Meng 2001). In this third step, I have split the samples as follows: one of each group was used for training, and the images of the remaining three samples were used for validation and testing data sets.

The training data were used for training and updating the weights of the network. The validation data were used to evaluate after each iteration the accuracy of the network. The testing data set was used to evaluate the accuracy of a trained model with a new dataset. The accuracy of the performance of the networks was calculated as the ratio of the sum of the true positive cases plus true negative cases over the total number of input images:

$$Accuracy = \frac{\sum True\ Positive + \sum True\ Negative}{\sum Total\ number\ of\ image}\ .$$

In our study, I kept constant some parameters: the optimizer algorithm RMSProb (Hinton, Srivastava et al. 2012) among the different cases and the number of epochs within one case. The number of epochs was chosen to assure convergence of the CNN. In this study, a network is said to converge when the difference in validation accuracy between two consecutive epochs is smaller than ± 0.5 %. The learning rate has always been adjusted to push the network to its best performance.

6.4. Results:

All validations were done concerning the histological data, taken as reference. For the cartilage data, the VGG16 network provided a testing accuracy of 99.8% (validation accuracy 99.8% and training accuracy 99.9%) after 25 epochs and a learning rate of 7×10^{-7}. In this case, none out of 760 images were falsely classified as healthy instead of degenerated (false-positive), and 3 out 760 images were classified healthy instead of degenerated (false-negative), as shown in the so-called confusion matrix in Figure 6.4 A. The time to train and validate this network was 34 minutes and 42 seconds.

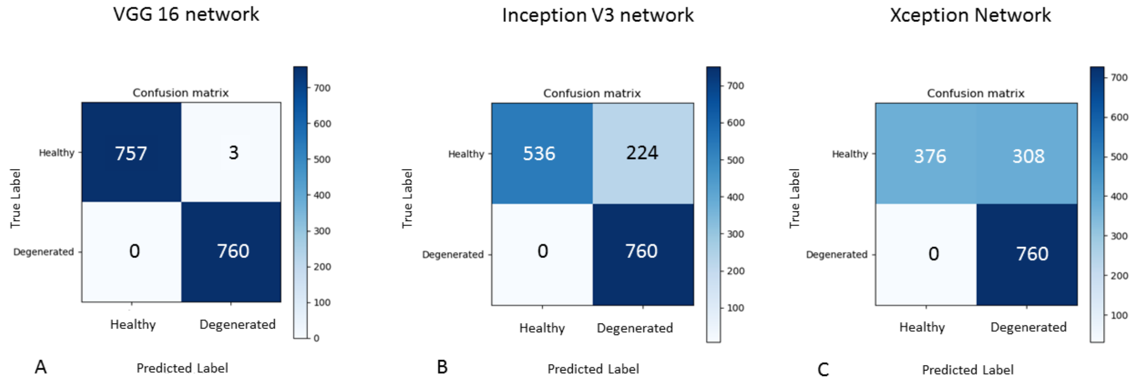

Figure 6.4 Confusion matrix of the VVG16, Inception V3, and Xception networks applied to the cartilage dataset. They show the "true" label (as a result of the histologic analysis) and the predicted (by the CNN) label. A) The test accuracy in classifying healthy and degenerated (i.e., OA affected tissues) is 99.8 % with the VGG 16 B) The test accuracy of the Inception V3 network is 84.7 % C) The Xception has a test accuracy of 72.6 %.

The inception V3 network classified the data with a test accuracy of 84.7% (validation accuracy 86.8% and training accuracy 96.6%) after 25 epochs with a learning rate of 1×10^{-6}; in numbers: 224 images were predicted as false negative and no images as false positive (Figure 3B); 536 healthy images were classified correctly, and 760 images with signs of degeneration were classified correctly over the total number of 1520 images (Figure 6.4 B). The calculation time for this network (training, validation and testing) was 19 min and 41 s. The Xception network has 308 images predicted false positive and 0 false negative; 376 healthy images and 760 degenerated are predicted correctly (Figure 6.4 C). Figure 6.5 shows the accuracy plot as a function of the number of epochs for the VGG16, the Inception and the Xception networks, respectively; it shows how they converge toward a stable solution for the same number of iterations.

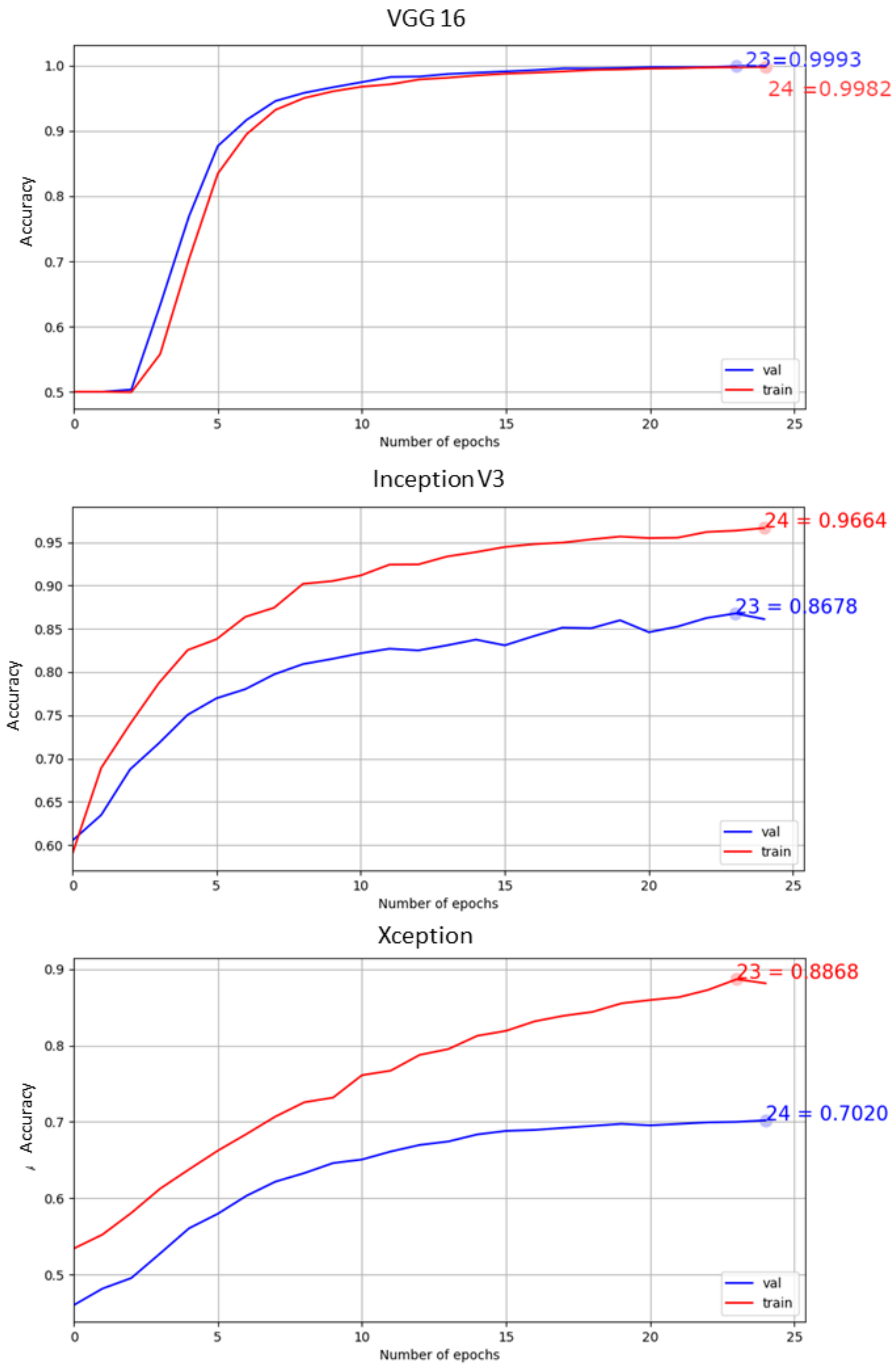

Figure 6.5 Accuracy plots as a function of the number of epochs for the VGG16, Inception V3 and Xception networks. The Xception has the largest gap between training and validation accuracy, and the VGG16 network achieves the highest level of accuracy.

Figure 6.5 is the accuracy plot as a function of the number of epochs for the VGG16, the Inception and the Xception networks, respectively; it shows how they converge toward a stable solution for the same number of iterations. With the Xception network, a validation accuracy of 70.20% and a testing accuracy of 72.63% was achieved after 25 epochs. The training, validation and testing with this Network took 37 min and 25 seconds. The accuracy of the training data is 88.68%. Using 42 epochs instead, the plateau (<

± 0.5% difference between epochs) was reached during the training accuracy (97.24%), the validation accuracy increased to 79.74%, and the testing accuracy was at 81.25%. With more epochs, the Xception network's testing accuracy could be increased, but it is still not as high as the testing accuracy of the inception or VGG16 network. The time for this calculation was 1h 14min and 33s.

In the next step, the cartilage data is split by samples. Images of one healthy and one degenerated sample were used for training. The images from the other samples were split into validation and testing data. Therefore, I have a split of 50/25/25 percent. 1900 images are used for training (950 images from a healthy sample, 950 images from a degenerated sample). 950 images are used for validation and testing. The training with this dataset is 25 epochs long. The testing (validation) accuracy of the VGG16 network is 68.6% (70.0%), whereas the training accuracy is 99.9 %. The training/validation and testing took 32 minutes and 45 seconds. The inception network achieved a testing (validation) accuracy of 65.9 % (66.6%) and a training accuracy of 99.0%. The calculation time was 29 minutes and 38 seconds. The testing (validation) accuracy was 75.7% (79.8%) of the Xception and a training accuracy of 99.8%. The testing accuracy of the VGG16 network, declined as well as the accuracy of the inception network when splitting the dataset based on samples. The Xception network increased its testing accuracy from 72.6% up to 75.7%.

For the liver data, I report in Figure 6.6 the confusion matrixes. For all the three CNNs, the convergence was obtained after 50 epochs. The VGG16 network was performed with a test accuracy of 96.0% (validation accuracy 96.1%), with a learning rate of 1×10^{-6}. The training accuracy is slightly lower at 94.6%. 2 healthy, 26 fat liver, 1 fibrotic (4 weeks) images got mistakenly classified (Figure 6.6 A). The computational time was 34 minutes and 21 seconds.

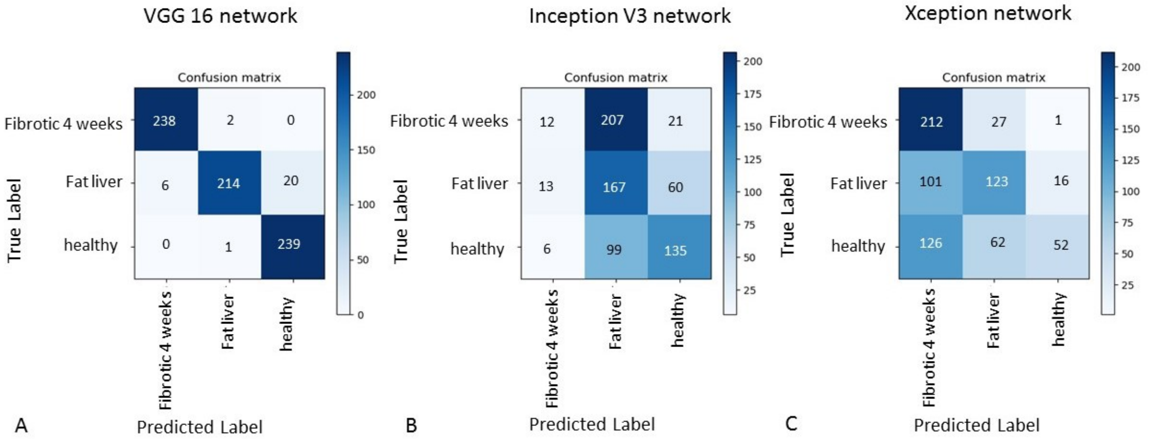

Figure 6.6 6.7 Confusion matrixes are representing the image classification capability for the VGG16 (A), Inception V3 (B) and Xception (C) networks. The testing accuracy of the VGG16 network is 96.0%, for Inception 43.6% and Xception 53.8%

The Inception V3 network, with a learning rate of $1\text{x}10^{-6}$, performed on this dataset with a test accuracy of 43.6% in 18 minutes and 54 seconds. By this network, 442 out of 720 images were falsely classified (Figure 6.6 B). The Xception network (learning rate of $1\text{x}10^{-6}$) was performed with a test accuracy score of 53.8 % on this dataset in 36 minutes and 1 second (Figure 6.6 C).

To increase the number of samples as input for the network, I decided to repeat the classification by rotating the images to get a more general classifier. The training/validation/testing ratio was set to

60/20/20 again. As a result, 14400 images (4x 360 original images) were available: 8640 images were used for training the CNNs and 2880 for the validation; finally, 2800 were used for testing the network. The networks converged faster with a larger number of images. Thus the number of epochs was reduced for this calculation down to 15 epochs. With the VVG16 network, a test (validation) accuracy of 95.6% (95.0 %) was achieved. The Inception V3 network reached a testing (validation) accuracy of 38.8% (35.8%) and the Xception network a test (validation) accuracy of 50.3% (48.8%), but the training accuracy was at 86.2% and 95.4%. The calculation times increased compared to the previous liver cases: 42 minutes and 11 seconds for the VGG16, 23 minutes and 10 seconds for the Inception network and 44 minutes and 19 seconds for the Xception network.

In the next step, I tested the network performances by training the system with images of one set of samples and then validating and testing it with another set. For training, 1800 images from three samples of different groups were used (600 images of one healthy liver sample, 600 images from one fatty liver sample and 600 images from one four-week perfusion sample). The testing dataset's classification accuracy by the VGG 16 network was 75.4 %, whereas the training (validation) accuracy score was 99.8% (73.7 %). Training (15 epochs) and testing process of this network took 10 min and 33 seconds. The inception network obtained a testing accuracy of 39.8 % and a training (validation) accuracy of 99.94% (41.0%). This training (15 epochs) and testing of the network took 6 min and 10 seconds. The Xception network achieved a testing accuracy of 42.0%. The training and validation accuracies were 98.7% and 46.4%, respectively. The training of the network with 15 epochs and testing lasted 11 min and 17 seconds.

6.5. Discussion and conclusions:

In this chapter, the possibility of using convolutional neural networks is shown. The networks are used to classify healthy and pathological biological tissues considering two different biomedical cases: osteoarthritic cartilage and liver fibrosis. The sample's evaluation was made by two experienced pathologists based on the histological results, which serves as a golden standard.

Three CNNs (VGG16, Inception V3, and Xception networks) are applied, and their performance is compared in terms of accuracy in the classification and the time needed for this calculation. The VGG16 network provided the highest accuracy, compared to the Inception V3 and Xception network in the analyzed cases. In the VGG16, the entire image is convoluted in every layer, whereas in the Inception V3 and the Xception networks, the image to be analyzed is split into different regions. This process of subdividing the images can lead to overfitting, which causes poor performance of the networks when applied to data in the validation phase. This is visible in the discrepancy between the training and validation accuracy curves for the Inception V3 and Xception networks.

I also tested the effect of training the network with images of two cartilage samples (one healthy and one degenerated) and validated and tested with images of other cartilage samples. The testing accuracy decreased in all of the three networks. But the Xception network was the one with the highest testing accuracy. This shows that the Xception network model is the best-generalized model when splitting the dataset by sample.

Many different ways, such as additional fully connected layers and drop out layers, changing the optimizer algorithm or adjusting the learning rate, were used to reduce overfitting in the Xception and Inception V3 networks. The results we presented here are obtained after this optimization procedure (best accuracy and lowest overfitting); instead, the results of these intermediate optimization procedures were not reported.

In the case of cartilage, other computer-aided diagnosis tools are available, like texture analysis. This kind of analysis of cartilage PCI images for characterizing osteoarthritis gives good results for both 2D images (Nagarajan, Coan et al. 2014) and 3D volumes (Nagarajan, Coan et al. 2015).

The Inception V3 network with its inception modules is much faster for training, validation and testing than the other two networks. For the cartilage dataset, the Inception is 56.7% faster than the VGG16 network and 47.4% than the Xception. For the liver dataset, the Inception is 26.6% faster than the VGG16 and 29.5% than the Xception network. Its unique inception module structure reduces the number of trainable weights and, therefore, speeds up the computation.

With the data augmentation of the liver dataset, I could show that the networks converged faster when the number of input images was increased and therefore, I needed fewer epochs. For the VGG16 network, the testing accuracy stayed approximately the same 95.5%. The computational time increased by 23.5% from 34 minutes and 21 seconds to 42 minutes and 11 seconds because of increasing the number of input images by a factor of 4. The conclusion can be made that more input data leads to better accuracy and faster convergence of the VGG network, but this does not come with shorter computational times.

When using data from different liver samples for the training and the testing of the networks, the getting is a decrease in testing accuracy of all the networks, whereas the training accuracy increased. This result shows that overfitting occurs and the networks do not generalize enough; to overcome this limitation, a larger number of samples should be used. The network presenting the best testing accuracy is the VGG16 with 75.38 %, as in the calculation without the split based on samples. Both the Inception V3 and Xception networks testing accuracy were for this test below 50 %; for this test and both networks did not perform well on liver data, in contrast to the cartilage data, both networks had a testing accuracy above 68 %. The testing accuracy strongly depends on the data splitting method that is used. If the slices for training and testing the CNN are extracted from the same sample, the two processes' data may look very similar, and overfitting the networks during training may occur. In this case, the generalization of CNN on new samples is unsettled and may be severely hindered.

This study shows that the combination of advanced high sensitive X-ray imaging techniques (i.e. PCI) with newly available algorithms for data classification based on the neural network concept could greatly help discriminate between healthy-normal and pathological-abnormal conditions of biological tissues. This methodology's proof of concept was here performed on small tissue samples (cylindrical bone/cartilage plugs of 7 mm of diameter). The possibility of a computerized and accurate classification offered by these combined tools could be an important asset in the direction of the automation of diagnostic procedures. The application of CNNs to our datasets showed that these tools (in the specific case, I identified the VGG16 network as the most accurate one) make it possible to analyze and classify sets of 9616 images of 224x224 pixels in less than 25 minutes providing a robust, fast and observer-independent method of diagnosis.

Bibliography

Abadi, M., A. Agarwal, P. Barham, E. Brevdo, Z. Chen, C. Citro, G. S. Corrado, A. Davis, J. Dean and M. Devin (2016). "Tensorflow: Large-scale machine learning on heterogeneous distributed systems." arXiv preprint arXiv:1603.04467.

Abidin, A. Z., B. Deng, A. M. DSouza, M. B. Nagarajan, P. Coan and A. Wismüller (2018). "Deep transfer learning for characterizing chondrocyte patterns in phase-contrast X-Ray computed tomography images of the human patellar cartilage." Computers in biology and medicine **95**: 24-33.

Bataller, R. and D. A. Brenner (2005). "Liver fibrosis." The Journal of clinical investigation **115**(2): 209-218.

Brandlhuber, M., M. Armbruster, B. Zupanc, P. Coan, E. Brun, W. Sommer and M. Rentsch (2016). "A Novel and Sensitive Approach for the Evaluation of Liver Ischemia-Reperfusion Injury After Liver Transplantation." Investigative Radiology **51**(3): 170-176.

Chollet, F. (2015). "Keras: Deep learning library for theano and tensorflow." URL: https://keras. io/k **7**(8).

Chollet, F. (2016) "Xception: Deep Learning with Depthwise Separable Convolutions."

Christian Szegedy, V. V., Sergey Ioffe, Jonathon Shlens, Zbigniew Wojna (2015). Rethinking the Inception Architecture for Computer Vision. arXiv:1512.00567.

Christian Szegedy, W. L., Yangqing Jia, Pierre Sermanet, Scott Reed, Dragomir Anguelov, Dumitru Erhan, Vincent Vanhoucke, Andrew Rabinovich (2014). Going Deeper with Convolutions.

Ciregan, D., U. Meier and J. Schmidhuber (2012). Multi-column deep neural networks for image classification. 2012 IEEE Conference on Computer Vision and Pattern Recognition.

Coan, P., F. Bamberg, P. C. Diemoz, A. Bravin, K. Timpert, E. Mützel, J. G. Raya, S. Adam-Neumair, M. F. Reiser and C. Glaser (2010). "Characterization of Osteoarthritic and Normal Human Patella Cartilage by Computed Tomography X-ray Phase-Contrast Imaging: A Feasibility Study." Investigative Radiology **45**(7): 437-444.

Cord, M. (2016). "A brief report of the Heuritech Deep Learning Meetup #5." Retrieved 9.8.2018, 2018, from https://blog.heuritech.com/2016/02/29/a-brief-report-of-the-heuritech-deep-learning-meetup-5/.

Davis, T., D. Gao, T. Gureyev, A. Stevenson and S. Wilkins (1995). "Phase-contrast imaging of weakly absorbing materials using hard X-rays." Nature **373**(6515): 595.

Deng, J., W. Dong, R. Socher, L.-J. Li, K. Li and L. Fei-Fei (2009). Imagenet: A large-scale hierarchical image database. Computer Vision and Pattern Recognition, 2009. CVPR 2009. IEEE Conference on, Ieee.

Felson, D. T. (1988). "Epidemiology of hip and knee osteoarthritis." Epidemiologic reviews **10**: 1-28.

Google. (2019). "Advanced Guide to Inception v3 on Cloud TPU." Retrieved 13. th February, 2019, from https://cloud.google.com/tpu/docs/inception-v3-advanced.

Hinton, G., N. Srivastava and K. Swersky (2012). "Rmsprop: Divide the gradient by a running average of its recent magnitude." Neural networks for machine learning, Coursera lecture 6e.

Hu, G., Y. Yang, D. Yi, J. Kittler, W. Christmas, S. Z. Li and T. Hospedales (2015). When face recognition meets with deep learning: an evaluation of convolutional neural networks for face recognition. Proceedings of the IEEE international conference on computer vision workshops.

Krizhevsky, A., I. Sutskever and G. E. Hinton (2012). Imagenet classification with deep convolutional neural networks. Advances in neural information processing systems.

Lee, Y. S., E.-A. Heo, H. Y. Jun, S. H. Kang, H. S. Kim, M. S. Lee, S.-J. Byun, S. H. Lee, S. H. Park and K.-H. Yoon (2010). "Articular cartilage imaging by the use of phase-contrast tomography in a collagen-induced arthritis mouse model." Academic radiology **17**(2): 244-250.

Li, J., Z. Zhong, D. Connor, J. Mollenhauer and C. Muehleman (2009). "Phase-sensitive X-ray imaging of synovial joints." Osteoarthritis and cartilage **17**(9): 1193-1196.

Marenzana, M., C. K. Hagen, P. D. N. Borges, M. Endrizzi, M. B. Szafraniec, K. Ignatyev and A. Olivo (2012). "Visualization of small lesions in rat cartilage by means of laboratory-based x-ray phase-contrast imaging." Physics in Medicine & Biology **57**(24): 8173.

Mirone, A., E. Brun, E. Gouillart, P. Tafforeau and J. Kieffer (2014). "The PyHST2 hybrid distributed code for high speed tomographic reconstruction with iterative reconstruction and a priori knowledge capabilities." Nuclear Instruments and Methods in Physics Research Section B: Beam Interactions with Materials and Atoms **324**: 41-48.

Mittone, A., I. Manakov, L. Broche, C. Jarnias, P. Coan and A. Bravin (2017). "Characterization of a sCMOS-based high-resolution imaging system." Journal of synchrotron radiation **24**(6): 1226-1236.

Mollenhauer, J., M. Aurich, Z. Zhong, C. Muehleman, A. Cole, M. Hasnah, O. Oltulu, K. Kuettner, A. Margulis and L. Chapman (2002). "Diffraction-enhanced X-ray imaging of articular cartilage." Osteoarthritis and cartilage **10**(3): 163-171.

Muehleman, C., D. Fogarty, B. Reinhart, T. Tzvetkov, J. Li and I. Nesch (2010). "In-laboratory diffraction-enhanced X-ray imaging for articular cartilage." Clinical Anatomy **23**(5): 530-538.

Nagarajan, M. B., P. Coan, M. B. Huber, P. C. Diemoz, C. Glaser and A. Wismuller (2014). "Computer-aided diagnosis for phase-contrast X-ray computed tomography: quantitative characterization of human patellar cartilage with high-dimensional geometric features." Journal of digital imaging **27**(1): 98-107.

Nagarajan, M. B., P. Coan, M. B. Huber, P. C. Diemoz and A. Wismuller (2015). "Volumetric quantitative characterization of human patellar cartilage with topological and geometrical features on phase-contrast X-ray computed tomography." Medical & biological engineering & computing **53**(11): 1211-1220.

Ruder, S. (2016). "An overview of gradient descent optimization algorithms." arXiv preprint arXiv:1609.04747.

Russakovsky, O., J. Deng, H. Su, J. Krause, S. Satheesh, S. Ma, Z. Huang, A. Karpathy, A. Khosla and M. Bernstein (2015). "Imagenet large scale visual recognition challenge." International Journal of Computer Vision **115**(3): 211-252.

Simonyan, K. and A. Zisserman (2014). "Very deep convolutional networks for large-scale image recognition." arXiv preprint arXiv:1409.1556.

Stroebel, J., A. Horng, M. Armbruster, A. Mittone, M. Reiser, A. Bravin and P. Coan (2020). "Convolutional neuronal networks combined with X-ray phase-contrast imaging for a fast and observer-independent discrimination of cartilage and liver diseases stages." Scientific Reports **10**(1): 20007.

Szegedy, C., A. Toshev and D. Erhan (2013). Deep neural networks for object detection. Advances in neural information processing systems.

Van Dyk, D. A. and X.-L. Meng (2001). "The art of data augmentation." Journal of Computational and Graphical Statistics **10**(1): 1-50.

Vidushi Sharma , S. R., Anurag Dev (2012). "A Comprehensive Study of Artificial Neural Networks." International Journal of Advanced Research in Computer Science and Software Engineering **2**(10).

Wagner, A., M. Aurich, N. Sieber, M. Stoessel, W. D. Wetzel, K. Schmuck, M. Lohmann, B. Reime, J. Metge, P. Coan, A. Bravin, F. Arfelli, L. Rigon, R. H. Menk, G. Heitner, T. Irving, Z. Zhong, C. Muehleman and J. A. Mollenhauer (2005). "Options and limitations of joint cartilage imaging: DEI in comparison to MRI and sonography." Nuclear Instruments and Methods in Physics Research Section A: Accelerators, Spectrometers, Detectors and Associated Equipment **548**(1-2): 47-53.

Zhang, X., X.-R. Yang, Y. Chen, H.-Q. Li, R.-M. Li, Q.-X. Yuan, P.-P. Zhu, W.-X. Huang and W.-j. Peng (2013). "Visualising liver fibrosis by phase-contrast X-ray imaging in common bile duct ligated mice." European Radiology **23**(2): 417-423.

Zhang, Z. (2015). "Chondrons and the pericellular matrix of chondrocytes." Tissue Engineering Part B: Reviews **21**(3): 267-277.

Conclusions

The focus of this Thesis was to **visualize and analyze** in 3D the changes of cartilage at the **early stages** of OA by using state-of-the-art, high sensitivity, and **multi-scale X-ray imaging techniques** to get a better understanding of the development of OA and the induced effects on the tissue.

The first part of the Thesis manuscript (chapters one, two and three) presents an overview of the cartilage tissue's anatomy and main characteristic and its pathological degeneration and a description of the X-ray's theoretical and technical aspects of phase-contrast imaging. The following chapters are dedicated to describing the imaging experiments carried out at the ESRF and SLS synchrotron facilities and the results obtained. Chapter six reports the work I have applied to advanced machine learning systems to obtain a user-independent and fast analysis of the acquired high detailed phase-contrast CT datasets. The ESRF and SLS provided state-of-the-art X-ray imaging instrumentation and setups and allowed collecting high-quality data for this doctoral work. The results I have obtained by combining these technological opportunities with specifically developed methodologies for data processing have been presented in three scientific manuscripts: one of these works has been published in the Scientific Reports journal (first author) (Stroebel, Horng et al. 2020), one in Instruments (second author) (Rack, Stroebel et al. 2020) and the third one (co-first author) is under review (Horng, Stroebel et al. 2020). Another publication in the Journal of Synchrotron Radiation was produced as the result of my contribution to the implementation and testing of a multi-scale imaging setup at the ESRF (Mittone, Fardin et al. 2020).

The experimental work of the Thesis moved along three main directions:

1) **To apply multiple-spatial-resolution X-ray phase-contrast CT to cartilage imaging** in order to detect small and early changes in the cartilage, which are signs of early stages of OA, and to depict also the overall structure of the tissue.

2) **To study the behavior of healthy and OA cartilage under different load (pressure) conditions** by setting up an *ad-hoc* experiment to collect 3D datasets of the tissue and by developing a method to evaluate the cell network changes in the different settings.

3) **To combine X-ray phase-contrast imaging with advanced machine learning methods** to get an automatic and observer-independent system to classify image data. This classification is done with artificial neural networks to discriminate healthy tissue images from images with early signs of OA.

The multi-scale X-ray phase-contrast CT imaging for cartilage was possible thanks to the development of the multi-scale pink-beam imaging setup at the ID17 Beamline (ESRF). Applying this setup to my cartilage samples helped test it with scientific samples and showed potential biomedical applications. As mentioned above, these advancements are presented in a publication (Mittone, Fardin et al. 2020), which is the foundation of chapter four in this Thesis.

The work on multi-scale imaging provided a 3D representation of the cell structure in different healthy cartilage layers. Using lower spatial resolutions (6 µm pixel size), the cells' distribution in each cartilage layer could be depicted. With higher spatial resolution (100 nm pixel size), a detailed view of cells and their inside structure could be obtained as well as parts of the fiber structure in between the cell structure could be resolved. Similarly, **early signs of tissue OA degeneration** could be analyzed at different length scales. At the highest spatial resolution, fiber bundles and micro-cracks could be depicted, which are a sign of degeneration. Results were **correlated with histology and TEM images** to verify the degradation signs and confirm the interpretation. This detailed and 3D X-ray imaging analysis serves as a sort of 'virtual histology' tool. It is referred to as in the relevant literature because it provides similar or higher spatial resolution than standard histology but in 3D and without the need to cut the sample. Such a high-resolution 3D examination of cartilage tissue, to my best knowledge, has never been obtained before.

In addition to the synchrotron radiation experiments, I showed that cartilage X-ray PCI could be, to some extend, performed by using **rotating anode**, **liquid metal and nano focus X-ray tubes**. These experiments were performed at the Fraunhofer Institute for Integrated Circuits in Würzburg and the Georg-August University of Göppingen at the Institute for X-ray physics. Only the liquid metal and nano-focused X-ray tubes provide images with **sufficient quality** for cartilage cell structure depiction. With those imaging setups, the cell distribution in cartilage was visible, but not the structure of single cells and the acquisition times for measurements are 3 to 10 times longer than at synchrotron facilities for the same sample.

The X-PCI experiment realized to study the biomechanical response of healthy and OA cartilage under pressure. The quantitative analysis of the acquired data gave interesting insights into the cartilage structure and its resident cells' behavior at rest and under load conditions simulating walking and running activities. I developed a methodology for analyzing residual cartilage cells of 3D X-ray phase-contrast images to depict and quantify cells' alterations and cell population in the tissue. The obtained data were compared to already reported results in the literature. The **mean volume of cells** in the superficial layer (close to the cartilage surface) **decreases** compared to the cartilage's mid and deep layers. But not only could I show that the mean volume was affected, but the mean orientation and shape of cells were changed in the superficial layer when applying pressure. I could show that the cell volume density in normal cartilage samples was, on average higher by a factor 1.6 than in the case of degenerated specimens. The cell volume density increases when applying pressure for non-degenerated samples by a factor of 1.5 and degenerated samples by 2.25.
Part of the data produced in this work is reported in Rack, Stroebel at al. 2020. (Rack, Stroebel et al. 2020).

The third and last focus of this thesis was to develop an **automatic procedure** for image classification of large data. This study showed that the combination of advanced high-sensitive X-ray imaging techniques and newly available algorithms for data classification based on the neural network concept can greatly help discriminate between healthy-normal and pathological-abnormal conditions biological tissues.

Three different **convolutional neural networks** (CNN), the VGG16 network, the inception V3 network and the Xception network, were trained with annotated high-resolution X-ray PCI cartilage images to classify not annotated cartilage images into healthy and degenerated groups.
The possibility of a computerized and accurate classification offered by these combined tools could be an important asset in the direction of the automation of diagnostic procedures. The application of CNN's to our datasets showed that these tools allow analyzing and classifying sets of images precisely and fast, providing a robust and observer-independent diagnosis method. The combination of convolutional neural networks to X-ray images of cartilage at such a high spatial resolution is an original work.
This part of the Thesis is published in Scientific Reports in the paper "Convolutional Neural Networks combined with X-Ray phase-contrast imaging for a fast and observer-independent discrimination of cartilage and liver diseases stages" (Stroebel, Horng et al. 2020)

In conclusion, this doctoral Thesis has proved that X-PCI-CT can provide a powerful tool for a fully 3D, highly accurate and quantitative depiction and characterization of healthy and early stage-osteoarthritic cartilage tissue sample. With respect to results produced and published in the literature before this Ph.D. work, in this Thesis, 3D images of the cartilage with unprecedented detail have been obtained using the most advanced synchrotron X-ray setups. Besides, accurate and efficient procedures for visualizing and quantitative assessing the tissues' morphological and biomechanical properties under different conditions (pathology and under pressure load) were implemented. I believe that the methodologies and results presented in this PhD manuscript represent valuable supports for a deeper understanding of osteoarthritis development and possible treatment strategies.

Bibliography

Horng, A., J. Stroebel, T. Geith, S. Milz, A. Pacureanu, Y. Yang, P. Cloetens, G. Lovric, A. Mittone, A. Bravi and P. Coan (2020). "Multiscale X-Ray Phase-contrast Imaging of human Cartilage for investigating Osteoarthritis Formation " Investigative Radiology **still under review**.

Mittone, A., L. Fardin, F. Di Lillo, M. Fratini, H. Requardt, A. Mauro, R. A. Homs-Regojo, P.-A. Douissard, G. E. Barbone and J. Stroebel (2020). "Multiscale pink-beam microCT imaging at the ESRF-ID17 biomedical beamline." Journal of Synchrotron Radiation.

Rack, A., J. Stroebel, T. Rack, Y. Dabin, C. Knabe, M. Stiller, P. Coan and P. Bleuet (2020). "TomoPress—In Situ Synchrotron-Based Microtomography under Axial Load." Instruments **4**(2): 11.